THESIS FOR THE DEGREE OF DOCTOR OF PHILOSOPHY

Development of Structural Steels for Powder Bed Fusion – Laser Beam

WILLIAM HEARN

Department of Industrial and Materials Science

CHALMERS UNIVERSITY OF TECHNOLOGY

Gothenburg, Sweden 2023

Development of Structural Steels for Powder Bed Fusion – Laser Beam
WILLIAM HEARN
ISBN: 978-91-7905-778-7

Doktorsavhandlingar vid Chalmers tekniska högskola
New serial no: 5244
ISSN 0346-718X

Department of Industrial and Materials Science
Chalmers University of Technology
SE-412 96 Gothenburg
Sweden
Telephone: + 46 (0)31-772 1000

Printed by Chalmers digitaltryck
Gothenburg, Sweden 2023

Development of Structural Steels for Powder Bed Fusion – Laser Beam

WILLIAM HEARN

Department of Industrial and Materials Science
Chalmers University of Technology

Abstract:
Over the past decade, powder bed fusion – laser beam (PBF-LB) has attracted noticeable attention from both academia and industry. However, there remains a scarcity of approved material for the process, as fewer than 40 alloys are commercially available. Although structural steels are some of the most commonly used materials in traditional manufacturing, they have yet to be developed for PBF-LB as their high carbon content makes them susceptible to cracking. The objective of this thesis was to develop structural steels for PBF-LB by determining the impact of various process parameters on part quality, microstructure and mechanical properties. This involved the production and analysis of various carbon (0.06 to 1.1 wt.% C) and low-alloy steels (AISI 4130, 4140, 4340 and 8620).

In terms of part quality, specimen density was related to the volumetric energy density (VED) and the carbon content of the alloy. Regarding the VED, specimens produced at low VED formed lack of fusion porosity, while specimens produced at high VED formed keyhole porosity. As for the carbon content, increasing the carbon content would reduce lack of fusion porosity at low VED, while lowering the required VED to form keyhole porosity. As for cold cracking, this occurred in structural steels with ≥ 0.38 wt.% C as elevated carbon contents would increase specimen hardness. However, cracking could be mitigated by increasing the VED, laser power or build plate preheating temperature, as each enhanced the level of in situ tempering during PBF-LB. From these findings, process windows were established for each structural steel that produced defect-free and high-density specimens (> 99.8%).

In terms of the microstructure, the as-built specimens were primarily composed of tempered martensite, with retained austenite also observed in alloys with ≥ 0.75 wt.% C. During PBF-LB, martensite formed during layer melting and was initially in a quenched-like state, with carbon atoms segregating to dislocations and martensite lath boundaries. Subsequent tempering of this martensite was due to micro-tempering within the heat affected zone and macro-tempering within the previously solidified material. Although both influenced martensite tempering, micro-tempering had the most significant effect as it reduced martensite hardness by up to ~380 HV. This noticeable reduction in hardness was due to the precipitation of nano-sized carbides at the previously carbon enriched regions of martensite.

Lastly, mechanical testing found that structural steels produced by PBF-LB achieved a high ultimate tensile strength (4140: ∼1400 MPa, 4340: ∼1500 MPa, 8620: ∼1100 MPa), impact toughness (4140:∼90–100 J, 4340:∼60–70 J, 8620:∼150–175 J) and elongation (4140:∼14%, 4340:∼14%, 8620:∼14–15%) that met or exceeded the ASTM standards. Additionally, these specimens displayed limited directional anisotropy due to small grains with weak crystallographic texture, a homogenous microstructure and low levels of internal defects. These findings are meant to highlight that these alloys are not only suitable but actively take advantage of PBF-LB to achieve properties that meet or exceed those of conventionally produced alloys.

Keywords: additive manufacturing; powder bed fusion – laser beam; structural steel; carbon steel; low-alloy steel; process development; cold cracking; martensite; in situ tempering; tensile properties.

Preface

The work presented in this doctoral thesis was conducted at the Department of Industrial and Materials Science at Chalmers University of Technology from May 2018 to February 2023. The work was conducted within the framework of the Center for Additive Manufacturing – Metal (CAM^2). The research was conducted under the academic supervision of Prof. Eduard Hryha. Prof. Lars Nyborg acted as examiner and co-supervisor.

This thesis consists of an introduction followed by the appended papers as listed below:

List of appended papers:

Paper I: Effect of Carbon Content on the Processability of Fe-C Alloys Produced by Laser Based Powder Bed Fusion

W. Hearn, E. Hryha

Frontiers in Materials 8 (2022) 800021

Paper II: Influence of Carbon on the Microstructure of Carbon Steels produced by L-PBF

W. Hearn, E. Hryha

Conference Proceedings of WorldPM 2022, Lyon, France

Paper III: Impact of Powder Properties on the Deoxidation and Densification Behavior of Carbon Steel produced by PBF-LB

W. Hearn, L. Cordova, A. Raza, A. Dahl-Jendelin, E. Hryha

Manuscript to be submitted

Paper IV: Laser-based powder bed fusion of non-weldable low-alloy steels

W. Hearn, R. Steinlechner, E. Hryha

Powder Metallurgy 65:2 (2022) 121-132

Paper V: In situ tempering of martensite during laser powder bed fusion of Fe-0.45C steel

W. Hearn, K. Lindgren, J. Persson, E. Hryha

Materialia 23 (2022) 101459

Paper VI: Development of powder bed fusion – laser beam process for AISI 4140, 4340 and 8620 low-alloy steel

W. Hearn, P. Harlin, E. Hryha

Powder Metallurgy (2022)

Contribution to appended papers:

Paper I: The author planned, executed and analyzed the majority of the experimental work and results. The author wrote the paper in collaboration with the co-authors.

Paper II: The author planned, executed and analyzed the majority of the experimental work and results. The author wrote the paper in collaboration with the co-authors.

Paper III: The author planned the experimental work and was involved in the execution and analysis with the co-authors. Measurements with the revolution powder analyzer were carried out by L. Cordova. Measurements with X-ray photoelectron spectroscopy were carried out by A. Raza. Measurements of the particle size distribution were carried out by A. Dahl-Jendelin. The author wrote the paper in collaboration with the co-authors.

Paper IV: The author planned the experimental work and was involved in the execution and analysis with the co-authors. The author wrote the paper in collaboration with the co-authors.

Paper V: The author planned the experimental work and was involved in the execution and analysis with the co-authors. Preparation, testing and analysis of TEM and APT specimens was carried out by K. Lindgren. Nano-hardness measurements were carried out by J. Persson. The author wrote the paper in collaboration with the co-authors.

Paper VI: The author planned the experimental work and was involved in the execution and analysis with the co-authors. Procurement of the raw material as well as mechanical testing was coordinated by P. Harlin. The author wrote the paper in collaboration with the co-authors.

Papers not appended in this thesis:

i) Processability & Microstructure of Fe-C System via L-PBF

W. Hearn, E. Hryha, S. Bengtsson, L. Nyborg

Proceedings of EuroPM2019 Conference, 2019

TABLE OF CONTENTS

ABBREVIATIONS

A_{C1}	Austenite Eutectoid Temperature
A_{C3}	Austenite Transition Temperature
AM	Additive Manufacturing
APT	Atom Probe Tomography
BCC	Body Centered Cubic
BCT	Body Centered Tetragonal
BSE	Backscattered Electrons
CAD	Computer Aided Design
CO	Carbon Monoxide
CO_2	Carbon Dioxide
EBSD	Electron Backscatter Diffraction
FCC	Face Centered Cubic
FIB	Focused Ion Beam
G	Thermal Gradient
GA	Gas Atomization
L-PBF	Laser Powder Bed Fusion
M_S	Martensite Start Temperature
M_{50}	50% Martensite Transformation Temperature
M_{90}	90% Martensite Transformation Temperature
M_f	Martensite Finish Temperature
OM	Optical Microscopy
PBF-LB	Powder Bed Fusion – Laser Beam
PSD	Particle Size Distribution
R	Growth Rate
RQ	Research Question
SE	Secondary Electrons
SEM	Scanning Electron Microscopy
T_B	Building Temperature
T_L	Liquidus Temperature
T_P	Phase Transition Temperature
T_s	Solidus Temperature
T_R	Residual Temperature
TEM	Transmission Electron Microscopy
UTS	Ultimate Tensile Strength
VED	Volumetric Energy Density
WA	Water Atomization
XPS	X-ray Photoelectron Spectroscopy
XRD	X-ray Diffraction
YS	Yield Strength

1 INTRODUCTION

1.1 BACKGROUND

Additive manufacturing (AM) relates to processing techniques that produce parts layer by layer, such as VAT photopolymerization, powder bed fusion, material extrusion, material jetting, binder jetting, directed energy deposition and sheet lamination [1]. These techniques allow for the production of near-net-shape parts directly from computer files, allowing design freedom that cannot be achieved when using conventional manufacturing techniques. Combined with high materials utilization, reduced lead times, and the ability to achieve part consolidation, it has allowed the AM market to reach a current value of $13.84 billion, with expected growth to $16.75 billion by 2022 and $76.16 billion by 2030 [2].

Metal-based AM accounts for more than 50.6% of the global AM market [3], with the most prominent method being powder bed fusion - laser-beam (PBF-LB), which represent 88% of all metal AM machines that are currently in use [4]. PBF-LB is expected to grow by 22.43% annually from 2021 to 2026 due to surging investment in research and development, as well as technological advancement in the aerospace, automotive, and defense industries [3].

Despite this promise, the use of PBF-LB still lags behind traditional manufacturing techniques. This is due to the comparatively low build rate and small build volume of the process, leading to long processing times and reduced lot sizes. PBF-LB also requires noticeable post-processing to remove support structures, improve surface roughness and remove residual stresses, which all increase processing time and cost. Considering these factors, PBF-LB is best suited for the production of small and complex parts with relatively low production volumes. This is because unlike conventional processes PBF-LB can add complexity and individualization for “free”, depending upon lot size and part complexity, see Figure 1.

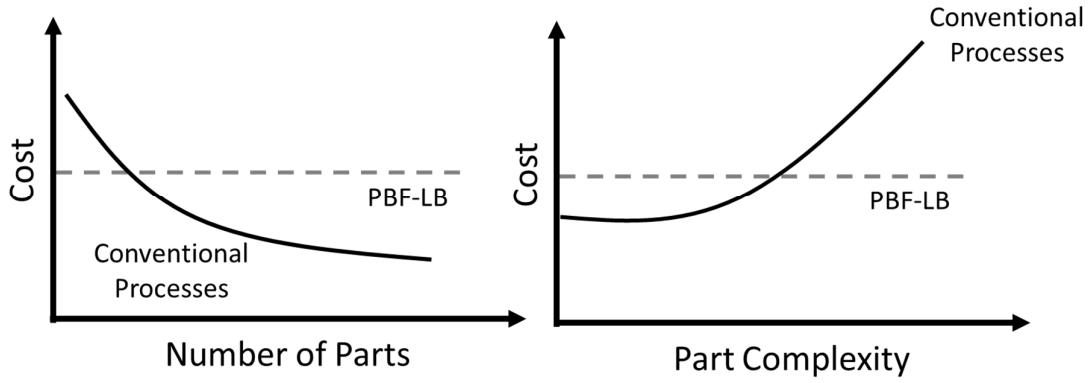

Figure 1: Comparison of PBF-LB to conventional processes in terms cost versus number of parts (left) and cost versus part complexity (right). Adapted from [5].

Another limitation of PBF-LB is the scarcity of approved materials, as currently there are fewer than 40 alloys available for the process. In more established techniques, iron-based alloys like structural steel are the most commonly used material, where over 90% are categorized as either carbon or low-alloy steel [6]. Considering that iron-based alloys in PBF-LB are limited to a select group of stainless and tool steels [7] [8] [9], this indicates a noticeable gap for the technology that severely hinders the application of produced parts [10] [11].

Structural steels like carbon and low-alloy steel are widely used in the automotive, railway and construction industries due to their combination of strength, toughness, and wear resistance at low material cost [12] [13]. In these industries, PBF-LB is well suited for the production of spare parts, which is currently a $194.43 billion market for the automotive industry alone, that is expected to grow to $284.15 billion by 2028 [14]. This suitability stems from the freedom of design afforded by PBF-LB, as essentially any spare part can be produced as long as there is a corresponding computer file. Additionally, PBF-LB can produce parts on demand, helping reduce or eliminate the need for maintaining part inventories. Lastly, PBF-LB can localize supply chains as the desired part can be produced wherever there is a PBF-LB machine available. This is important, especially after the disruptions to the global supply chain that have occurred since the start of the Covid-19 pandemic.

An example outlining the potential of PBF-LB to produce spare parts was demonstrated by the Center for Additive Manufacture – Metal (CAM^2) at Chalmers University of Technology. Here PBF-LB was used to produce an injector yoke for heavy duty diesel engines that is typically made from low-alloy steel. This component is for aftermarket use and requires approximately 100 parts per year. Traditionally these injector yokes were produced by press and sintering, however after their inventory ran out, Volvo AB found that their part supplier was no longer in business. Without the previous infrastructure in place, press and sintering became too expensive due to the low annual lot size. Therefore, new injector yokes had to be produced using CNC-machining of solid bars. This new method was still quite expensive and led to a large amount of material waste. Under these circumstances, PBF-LB provides a good use-case in terms of time, cost and lot size. And from the case-study it was found that these injector yokes could be produced by PBF-LB using low-alloy steel after adequate process development, see Figure 2.

Figure 2: Example of injector yokes (Volvo AB) that were made from AISI 4140 low-alloy steel and produced by PBF-LB.

Despite the strong use-case for structural steels, their use remains limited in PBF-LB. This is due to their high carbon content (> 0.3 wt.% C) which induces large cracking defects within the material due to the combined presence of brittle martensite and residual stress. These cracks should be avoided, as defects close to the specimen surface [15] [16] or defects that are elongated in shape [17] [18] will reduce mechanical properties. This issue, combined with other process defects, has led to reduction in properties when compared to conventionally produced alloys [19] [20], bringing into question the suitability of structural steels when using PBF-LB.

1.2 Objectives

The objective of this thesis was to develop structural steels for PBF-LB through determining the impact of the carbon content and process parameters on part quality, microstructure and mechanical properties. Understanding the necessary conditions for crack-free and high-density parts (>99.8%) is vital to establish robust processing windows that can determine the suitability of the alloys for the process. These objectives can be summarized in the following research questions (RQ):

> ***RQ1:*** What is the impact of carbon content on processability and microstructure of structural steels?
>
> ***RQ2:*** What is the impact of process parameters on porosity and cold cracking?
>
> ***RQ3:*** What is the impact of local thermal history on microstructure and mechanical properties?

1.3 Research Approach

At the beginning of this thesis work, the processing of carbon steels was based on the concept of alloy weldability, where alloys with carbon content above 0.3 wt.% were considered difficult, if possible, to produce. To understand the processability of structural steels by PBF-LB, initial work focused on how carbon impacted the processability and microstructure of Fe-C alloys at compositions between 0.06 to 1.1 wt.% C. Once this was established, work then examined the impact of process parameters on the production of defect-free and high-density specimens (> 99.8%). Then finally, once robust process windows were defined, these parameters were used to test mechanical properties and define the suitability of structural steels for PBF-LB. This research approach is presented in Figure 3.

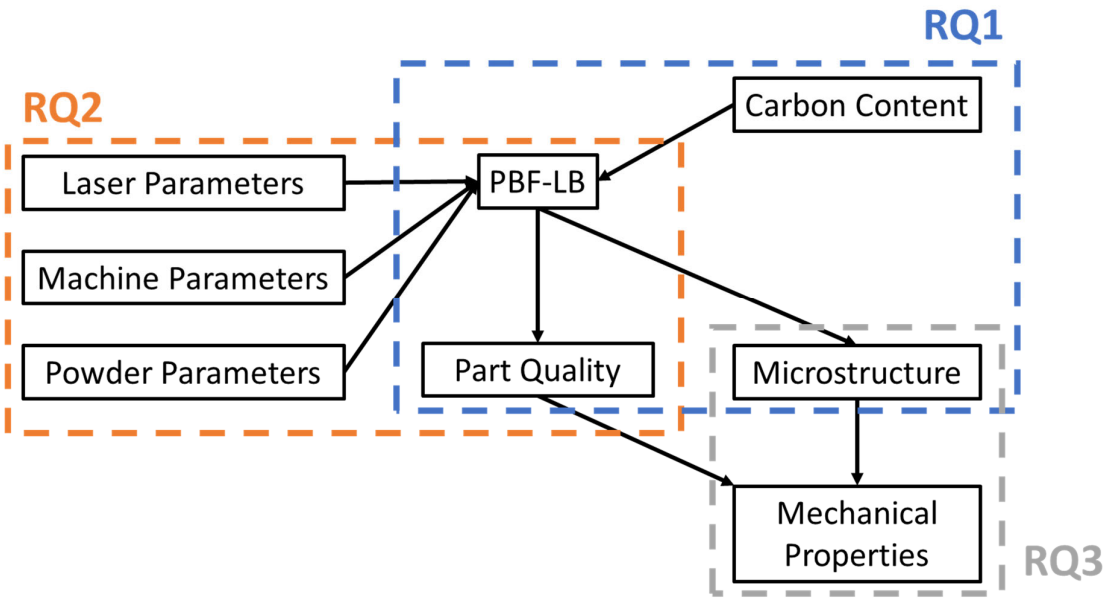

Figure 3: Schematic of the research approach used in this thesis. The topics covered by RQ1 (blue), RQ2 (orange) and RQ3 (grey) are outlined by corresponding boxed regions.

The primary objective for each appended paper can be summarized as follows:

- *Paper I* examined the impact of carbon content (from 0.06 to 1.1 wt.% C) and laser parameters on the production of crack-free and high-density carbon steels, at VEDs between 60 to 200 J/mm^3.
- *Paper II* examined the impact of carbon content (from 0.06 to 1.1 wt.% C) on the microstructure of carbon steels produced by PBF-LB.
- *Paper III* examined the impact of carbon content (from 0.06 to 1.1 wt.% C) and powder parameters on oxygen loss and part quality of carbon steels, at VEDs between 60 to 200 J/mm^3.
- *Paper IV* examined the impact of laser parameters on the production of crack-free and high-density AISI 4130, 4140, 4340 and 8620 low-alloy steels, at laser powers between 110 to 170 W and VEDs between 60 to 220 J/mm^3.
- *Paper V* examined how the local thermal history impacts the formation and tempering of martensite during PBF-LB of Fe-0.45C steel, at VEDs of 60, 100 and 190 J/mm^3.
- *Paper VI* examined the influence of laser and machine parameters on the production of crack-free and high-density AISI 4140, 4340 and 8620 low-alloy steels, at VEDs of 60 to 200 J/mm^3 and BPTs of 25 to 180°C. After the highest performing parameters were established, tensile and Charpy impact specimens were tested to determine the performance of these alloys when produced crack free and high-density by PBF-LB.

The specific material(s), machine and research question(s) addressed in each appended paper are summarized below in Table 1.

Table 1: Research questions, materials and machines examined within the appended papers.

	RQ1	RQ2	RQ3	Material	Machine
Paper I				Carbon Steel	EOS M100
Paper II				Carbon Steel	EOS M100
Paper III				Carbon Steel	EOS M100
Paper IV				4130, 4140, 4340, 8620	EOS M100
Paper V				Fe-0.45C Steel	EOS M100
Paper VI				4140, 4340, 8620	EOS M290

2 POWDER BED FUSION – LASER BEAM (PBF-LB)

2.1 WORKING PRINCIPLE

PBF-LB is an AM technique that selectively fuses regions of a powder bed using a high-powered laser source to produce parts layer by layer. The process begins with the creation of a computer aided design (CAD) file that provides a 3D representation of the intended part. This CAD file is subsequently converted to a STL file which segments the part into a collection of 2D representations. Once converted, this STL file is prepared for printing using a specialized software that places the part on the build platform, defines the part orientation and adds support structures when needed. After this is complete, the file can be sent to the machine for printing.

To prepare the machine for printing, it needs to be filled with powder, the build platform needs to be leveled and an inert atmosphere needs to be established. Once this is complete, the build cycle begins with the spreading of a thin powder layer over the build platform, see Figure 4. Next, the laser selectively fuses regions of the powder bed based upon the desired part geometry as well as the support structures. Then the build platform is lowered, the recoating mechanism returns to its original position and the process repeats until all layers are printed. During this build cycle, an inert environment is maintained via the constant flow of shielding gas.

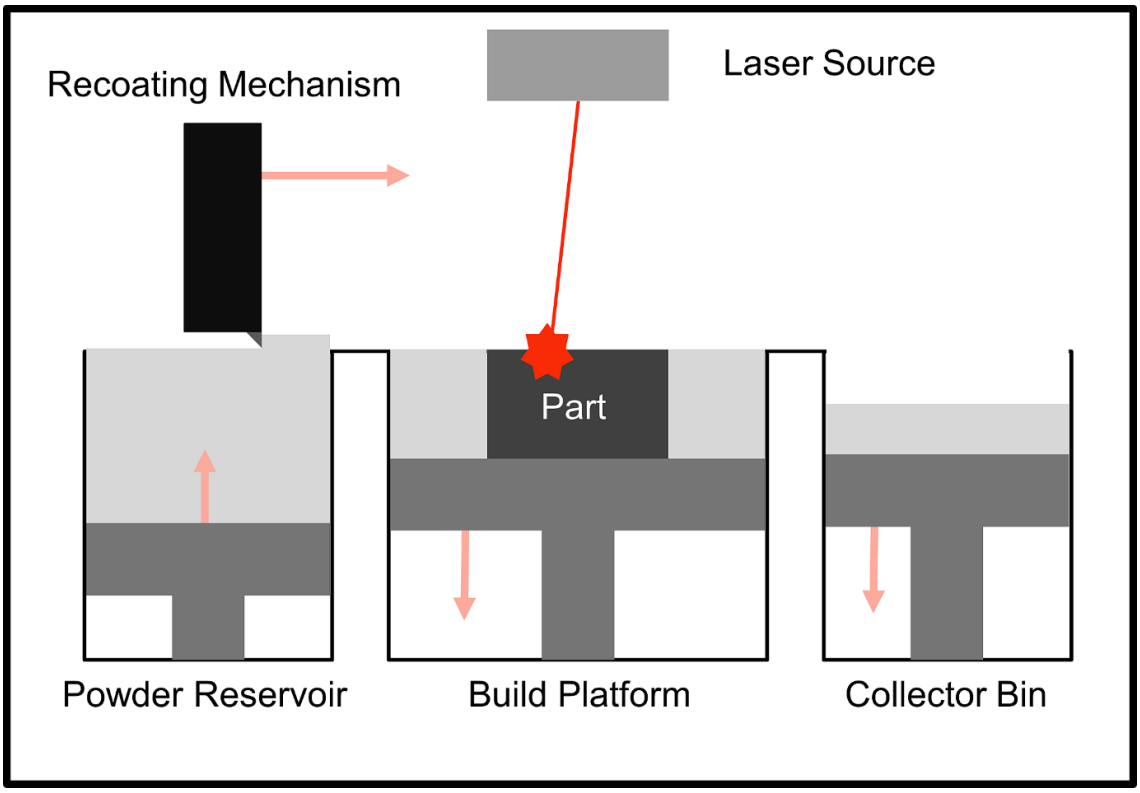

Figure 4: Schematic of a PBF-LB machine. Powder is depicted in light grey, while the arrows indicate the motion of different components during the build cycle.

2.2 PROCESS PARAMETERS

This section outlines the relevant process parameters of PBF-LB and how they affect part quality. To help categorize these parameters they have been organized into three groups: (i) powder parameters, (ii) machine parameters and (iii) laser parameters, see Figure 5.

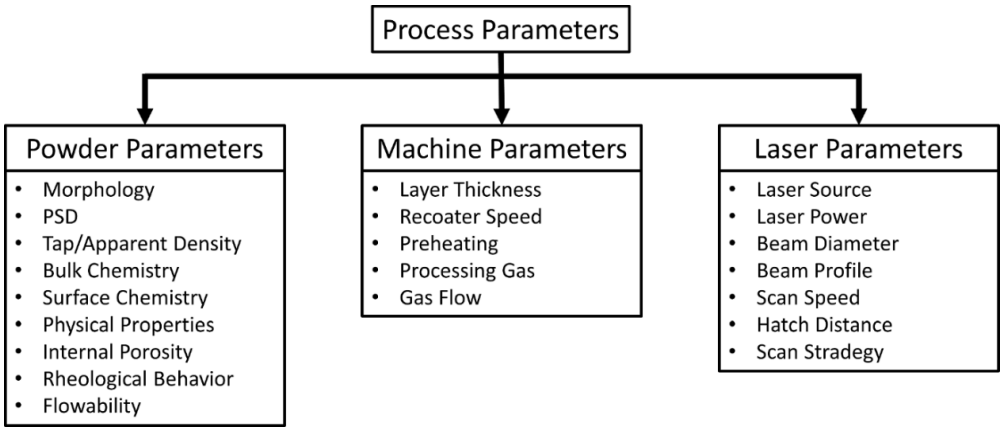

Figure 5: Diagram outlining the relevant process parameters of PBF-LB.

2.2.1 Powder Parameters

Powder parameters refer to characteristics of the powder feedstock such as particle morphology, particle size distribution (PSD), packing density, powder chemistry, powder flowability and rheological powder behavior [5]. These factors are crucial for PBF-LB as they impact powder spreading, powder packing and laser absorption, which subsequently influence in-process performance as well as final part quality [21] [22] [23] [24]. Generally, spherical powders are important to achieve improved packing density and powder flowability [25], while the particle size distribution determines the packing density and flowability of the powder [26] [27].

Despite this, clear correlations between powder properties and part properties have been difficult to establish, making it hard to outline specific requirements of the powder to achieve high part quality and good in-process performance [24]. Some of this difficulty stems from the interconnected nature of powder properties, as many are dependent upon one another, see Figure 6. For example, the rheological powder behavior is not a directly measurable quantity. Instead, it is an umbrella term that describe the behavior of powder when subjected to stress or movement. This makes it dependent upon a variety of powder parameters. Further complexity is added as there are many methods that can measure each powder property, with each involving a different testing procedure and set of equipment.

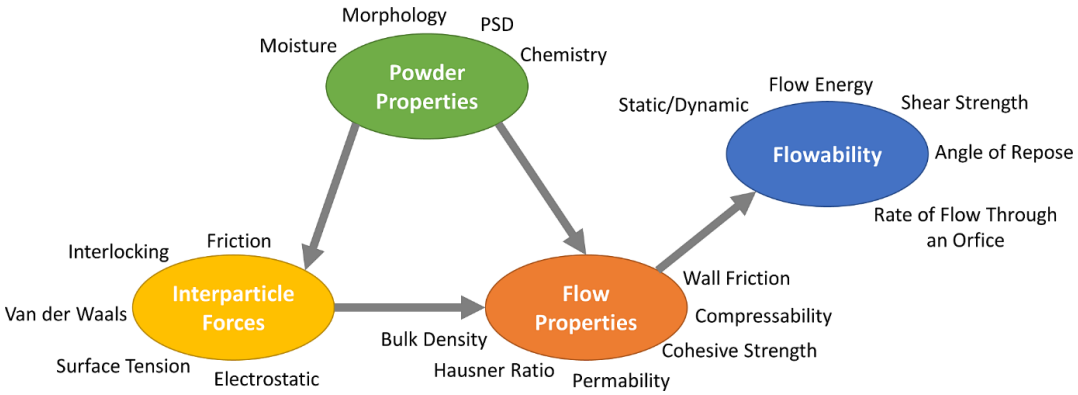

Figure 6: Schematic outlining the connection between various powder properties. Adapted from [24].

The properties of the powder feedstock are dependent upon the chosen manufacturing process [23] [28], the number of times the powder has been re-used [21] [29] and how this powder re-use was conducted [24]. For PBF-LB, the production of powder is typically done via atomization, which involves the break-up of a liquid metal stream into small droplets due to the application of pressurized matter. The most common atomization technique for PBF-LB is gas atomization (GA), which uses inert gas to facilitate the atomization process and where the preparation of the melt takes place either in air or in vacuum. The preference for GA stems from its ability to produce spherical powders with a controlled particle size distribution, while still maintaining high powder yield and relatively low production cost [5]. An example of gas atomized powder is presented in Figure 7.

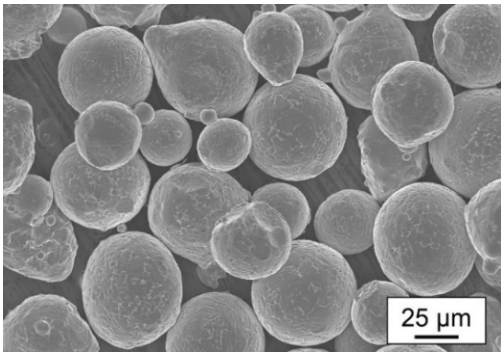

Figure 7: Example of gas atomized Fe-0.45C steel powder.

In terms of powder re-use, the biggest consideration is the accumulation of oxygen, as a steady increase in oxygen can lead to diminished in-process performance as well as a reduction in mechanical properties [21] [30] [31] [32].

2.2.2 Machine Parameters

Machine parameters relate to inputs such as the recoater speed, layer thickness, build plate preheating temperature and process atmosphere. Typically, an adequate recoater speed must be chosen to ensure proper uniformity and packing of the powder bed during spreading [33]. As for the layer thickness, this parameter is often increased to improve the build rate. However, without proper adjustment of other parameters this can lead to the formation of defects [34] and an increase in the surface roughness [35]. Build plate preheating is commonly applied during PBF-LB to reduce residual stress [36] [37], as a higher ambient temperature will lower the thermal gradient and cooling rate during solidification, while simultaneously providing in situ tempering [38]. Lastly, adjustment of the process atmosphere is used to ensure a low residual oxygen level, assist with heat transfer and remove metal vapors or ejected powders away from the melt pool. Adjustment of the chosen process gas (Ar, N_2 or He) can control the amount of produced metal vapor and ejected metal particles [39], while also influencing the rate of heat extraction [40]. As for the gas flow, it must be controlled to ensure adequate removal of metal vapor and ejected particles, as these by-products can interact with the laser source or become redeposited on the powder bed leading to the formation of defects [39] [41].

2.2.3 Laser Parameters

Laser parameters refer to inputs such as the laser source, beam diameter, beam profile, laser power, scan speed, hatch spacing and scan strategy. Currently, most PBF-LB machines are equipped with Yb-fiber lasers as their shorter wavelength improves energy absorptivity in metals [42], while also providing lower maintenance cost due to greater laser stability and efficiency [43]. In terms of the beam profile, PBF-LB machines typically utilize a Gaussian power density distribution [44], which provides the greatest intensity at the center of the beam that gradually decreases as the distance from the center

increases. The laser beam is commonly applied as a continuous wave; however, some works have experimented with pulsed laser sources which can lead to improvements in microstructural refinement, mechanical properties and energy utilization [45] [46].

To achieve a fully dense material there needs to be adequate energy input from the laser to achieve full melting, in addition to adequate overlap between layers and melt tracks. With respect to full melting, this is primarily driven by the power density distribution of the laser (P_d), which is a function of the laser power (P), radial distance from the heat source (r), radius of the heat source (r_b) and distribution factor (f) [38]:

$$P_d = \frac{fP}{\pi r_b^2} \exp\left(-f\frac{r^2}{r_b^2}\right) \tag{2.1}$$

From this power density distribution, the most important parameters are the laser power and beam diameter, as they control the formation of the melt pool during PBF-LB [47] [48] [49] [50] [51]. Regarding adequate overlap between layers and melt tracks, this is controlled by the scan speed and hatch spacing, which define the speed of the laser and the spacing between melt tracks, respectively. Control of the scan speed is vital as this influences the size and the stability of the melt pool [49] [52] [53] [54], while the hatch spacing must be controlled to guarantee adequate overlap between deposited melt tracks [34] [55].

To simplify the required process parameters for full melting and bonding, a combined process parameter is often used that called the volumetric energy density (VED). This VED describes the total energy input per volume of material within the powder-bed and is a function of the laser power (P), scan speed (v), hatch spacing (h) and layer thickness (t), see Figure 8:

$$VED = \frac{P}{v*h*t} \tag{2.2}$$

Previous works have shown that the VED can be related to the size and shape of the melt pool [49] [52] [53] [54], making it a simple parameter for process development that is easily adjusted. However due to its simplicity, the VED is unable neither to describe the complex heat and mass transfer that occurs within the melt pool, nor can it provide information regarding how much of the inputted energy is absorbed by the material. This means that caution must be applied when using the VED as a design parameter. Still, it provides a rough estimation of the applied energy input and is a useful tool that can aid in process development, as long as it is not used as an absolute metric.

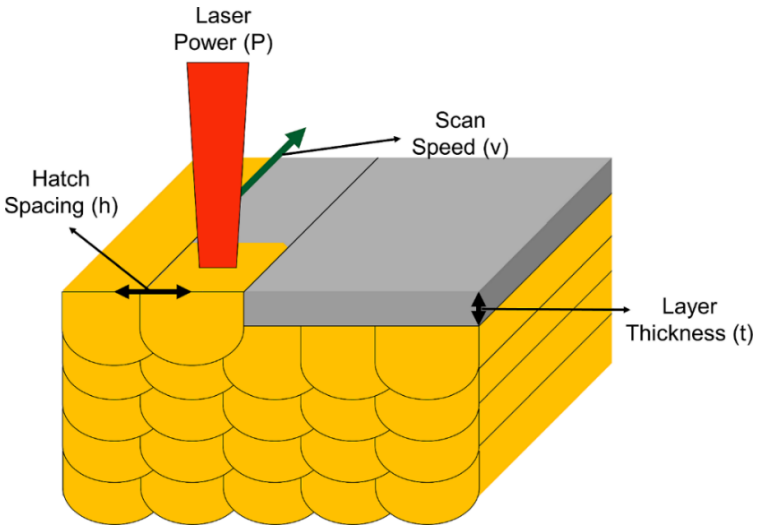

Figure 8: Schematic outlining the various process parameters of the VED.

The other important laser parameter is the scanning strategy, which defines the path of the laser during exposure and impacts defect formation, surface roughness, microstructure and residual stresses [56] [57] [58] [59]. Generally, when exposing a single layer there are two areas of interest. The first is the exposure of the entire area which is termed core exposure, while the second is the exposure of the part edges which is termed contour exposure, see Figure 9. This contour exposure is often used to improve surface roughness [60] and remove porosity that can form at the end of a melt track [61].

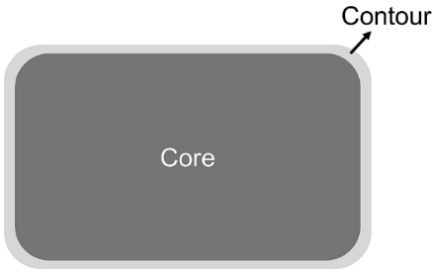

Figure 9: Schematic outlining the regions of contour exposure (light grey) and core exposure (dark grey).

As for core laser exposure, different laser paths can be employed. The simplest is unidirectional scanning, where laser vectors all travel in the same direction, see Figure 10a. Another is bi-directional scanning where the direction of the laser vectors progressively alternates, see Figure 10b. Besides the direction of the laser vectors, the planned exposure area can be divided into different regions as well. The most common methods are either island or stripe scan patterns. Where an island pattern divides the total exposure area into several islands, see Figure 10c, while a stripe pattern divides the exposure area into several stripes, where the translational direction of the laser is alternated by 180˚ between each stripe, see Figure 10d. The last component of the scan strategy is the rotation angle between layers. Typically, the rotation angle is set at 67˚ as this angle provides the greatest number of orientations before the original orientation is repeated [62].

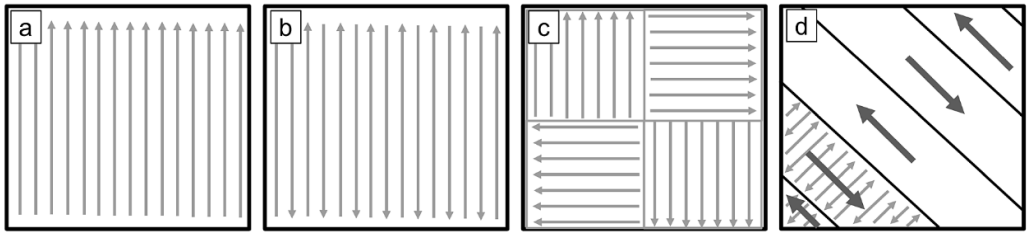

Figure 10: a) Unidirectional exposure, b) bi-directional exposure, c) island scan pattern, and d) stripe scan pattern. For each schematic, the light grey arrows indicate the direction of the laser vectors, while the dark grey arrows indicate the translational direction of the laser.

2.3 THERMO-PHYSICAL PHENOMENA DURING PBF-LB

This section outlines the various thermo-physical phenomena that occur during PBF-LB including the formation and dynamics of the melt pool, the formation of spatter particles and the local thermal history.

2.3.1 Melt Pool Formation & Dynamics

During PBF-LB the formation of the melt pool is governed by the interaction between the laser source and the particles in the powder bed. When the laser first contacts a metal particle, some of the inputted energy will interact while the rest is reflected away. As long as this reflected energy stays within the powder bed, it can continue to interact with other metal particles until its intensity becomes negligible [63]. The heat transfer between the laser and metal particle is rapid, with the irradiation of a metal

particle happening in approximately 0.2 to 8 ms [64]. This leads to a high concentration of thermal energy on the metal powder surface, that within 10 to 50 µs is transferred to the rest of the powder bulk [65]. As several metal particles melt and coalesce a melt pool is formed.

The morphology of this melt pool is first dependent upon the mode of heat transfer. In traditional laser-based manufacturing, heat transfer occurs either in conduction or keyhole mode [66]. In conduction mode, heat is transferred to the rest of the material via conduction, forming a shallow and wide melt pool. As for keyhole mode, a deep and elongated melt pool forms due to material evaporation and the formation of a vapor plume that exerts a recoil pressure onto the melt pool. Here, heat transfer occurs due to conduction at the surface and due to conduction within the interior of the induced vapor depression [67]. Typically, the transition from conduction to keyhole mode occurs when the energy from the laser is large enough to induce material evaporation and form a vapor depression [38]. Past studies have found that a vapor depression is a common characteristics of the PBF-LB process [49] [68], as the peak temperature can often meet or exceed the vaporization temperature [68] [69].

Another important factor that governs the melt pool morphology is the movement of material within the melt pool. During PBF-LB this movement of material is primarily driven by Marangoni flow, where surface tension gradients, that result from non-uniform temperatures, induce convective flow from regions with low surface tension to regions with high surface tension. The strength of this Marangoni convection can be estimated using the Marangoni number (M_α), where $\frac{d\gamma_{LV}}{dT}$ is the surface tension gradient, $\frac{dT}{ds}$ is the thermal gradient, L is the characteristic length of the melt pool, η is the viscosity and δ is the thermal diffusivity:

$$M_a = \frac{d\gamma_{LV}}{dT}\frac{dT}{ds}\frac{L}{2\eta\delta} \tag{2.3}$$

The direction of Marangoni flow depends upon the sign of the surface tension gradient. For most metals there is a negative surface tension gradient [53]. In this case, the flow of material will be away from the center, creating a wide and shallow melt pool where there will be more material at the melt pool edge, see Figure 11. However, the surface tension gradient can shift to a positive value when there is a noticeable presence of surface-active elements like oxygen, sulfur and nitrogen [70] [71]. In this case, the flow of material will instead be towards the center, creating a narrow and deep melt pool where there will be more material at the melt pool center, see Figure 11.

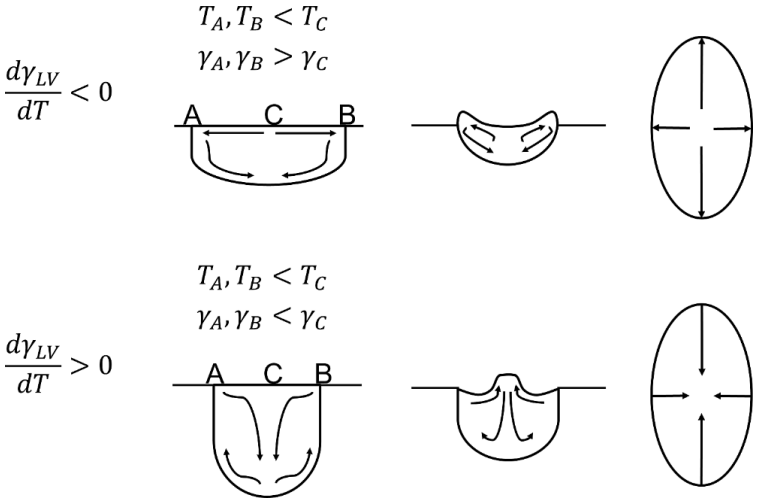

Figure 11: Schematic of Marangoni flow within a melt pool for a negative (top) and positive (bottom) surface tension gradient. Adapted from [71] [72].

2.3.2 Spatter Formation

The interaction between the laser, powder bed and melt pool can induce the formation of unwanted process by-products known as spatter. These spatter particles are typically oxidized [73] and are agglomerated or spherical in shape [41] [74] [75]. The characteristics of individual spatter particles will also vary depending upon their formation mechanism [69], see Figure 12. Cold spatter forms when entrained particles are ejected without interacting the laser beam, while hot spatters form when entrained particles do interact with the laser beam while being ejected. This entrainment is due to the strong pressure drop around the vapor jet which induces gas flow towards the melt pool [76]. Hot spatter can also form due to the ejection of material from the melt pool, when the recoil pressure exerted by the vapor plume exceeds the internal surface tension forces of the melt pool [77].

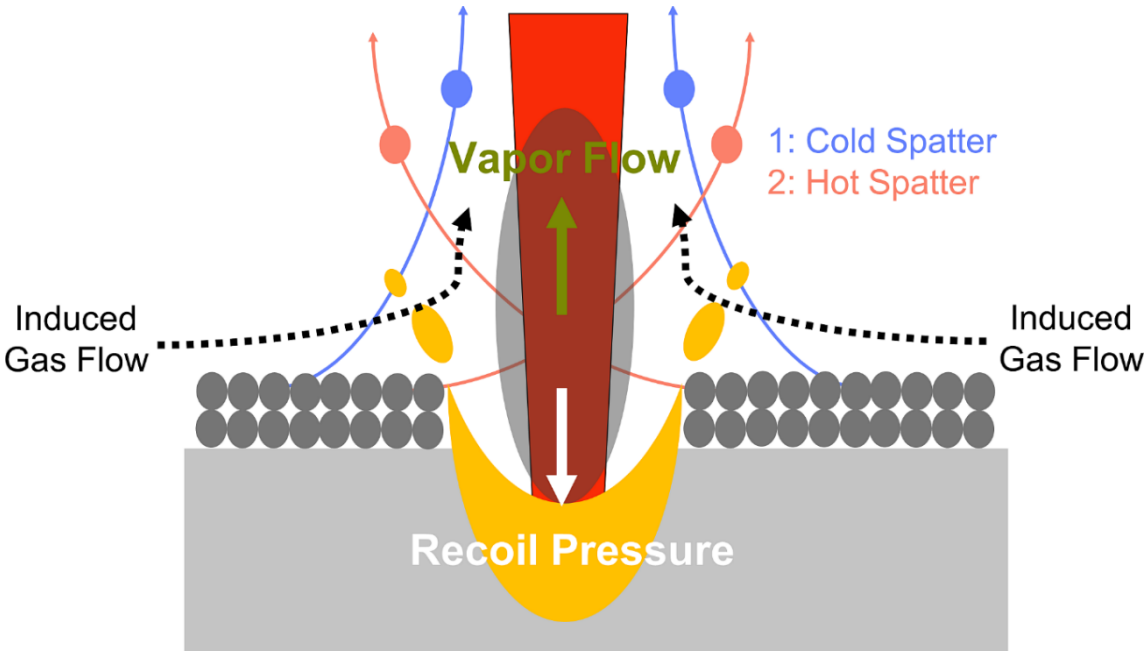

Figure 12: Schematic outlining the various types of spatter that can form during PBF-LB. Adapted from [69].

The formation of these spatter particles, especially hot or recoil induced spatter, is undesired as they can have a negative impact on final part quality. This is because the interaction between entrained metal particles and the laser can induce beam attenuation, leading to the formation of defects [78]. Additionally, these ejected spatter particles can become re-deposited onto the powder bed. This is undesired as their highly oxidized surface makes it difficult to achieve adequate melting and bonding during subsequent passes of the laser [41]. Lastly, the oxidation and re-deposition of spatter can lead to the formation of oxygen inclusions within the produced part [79] and increase the accumulation of oxygen during powder re-use [80] [81], as oxidized spatter is difficult to remove when using manual techniques like sieving.

2.3.3 Local Thermal History

The local thermal history during PBF-LB defines the temperature-time profile at a specific location during the process and can be broadly categorized as two stages: (i) Initial solidification during melt track deposition and (ii) In situ tempering during the deposition of subsequent melt tracks and layers, see Figure 13.

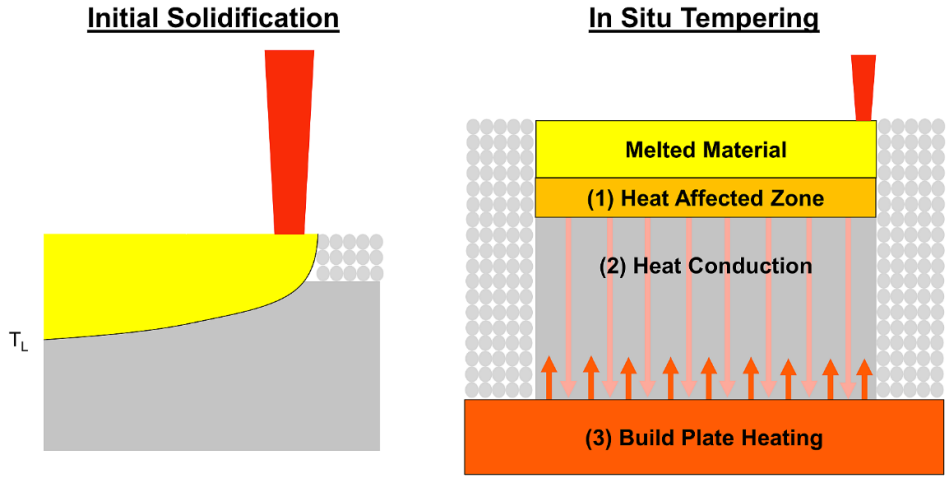

Figure 13: Schematic outlining the stages of the local thermal history including; (i) initial solidification and (ii) in situ tempering. In situ tempering relates to tempering within the heat affected zone (light orange), tempering due to heat conduction (pink arrow) and tempering due to build plate preheating (red arrow).

During the first stage of the local thermal history, material is rapidly heated above the above the liquidus temperature (T_L) before rapidly cooling to the building temperature (T_B) at cooling rates of 10^4 to 10^6 K/s [47] [68], see Figure 14. These rapid cooling and solidification rates are possible due to the small diameter of the laser source which generates a small melt pool relative to the underlying substrate and layers, inducing a self-quenching effect. Typically, the depth and width of the melt pool is on the order of 100 to 200 µm, while the thickness of the powder layer is on the order of 20 to 80 µm and the spacing between melt tracks is on the order of 50 to 150 µm. This means that during melt track deposition, previously deposited material is remelted in addition to the spread powder layer.

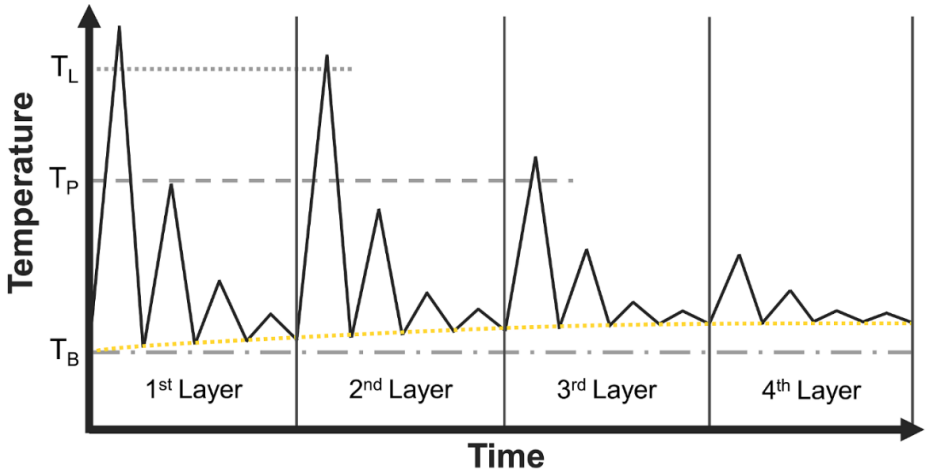

Figure 14: Schematic outlining the local thermal history (black) during PBF-LB. The liquidus temperature (T_L), phase transition temperature (T_P) and building temperature (T_B) are labelled using grey lines, while the residual temperature is labeled using a dotted yellow line. Adapted from [82] [83].

As for the second stage of the local thermal history, this relates to heating of material below the phase transition temperature (T_P), which for structural steel is the stability temperature of austenite (A_{C1}). In total, there are three phenomenon that contribute to in situ tempering during PBF-LB, see Figure 13. The first is micro-tempering that occurs within the heat affected zone during layer melting. Here, all material heated below the A_{C1} will undergo rapid tempering that repeats each time a new melt track or layer is deposited. This induces a cyclic intrinsic heat treatment, where the peak temperature progressively decreases as the distance from the heat source increases [84] [85] [86], see Figure 14. The second phenomenon is macro-tempering that occurs within the previously solidified material due to heat conduction and accumulation. This form of tempering takes place as the thermal conductivity of the solidified material is approximately 100 times larger than the surrounding powder bed [87]. This induces conductive heat flow towards the build platform that leads to heat accumulation and an increase in the residual temperature (T_R) of the specimen [83], see Figure 14. Typically, a somewhat constant residual temperature is reached after 10 to 20 layers [88], and will remain at said temperature in a quasi-steady state until the end of the process [89]. The last in situ tempering phenomenon relates to pre-heating of the build plate which will increase the building temperature (T_B), see Figure 14.

2.4 DEFECTS IN PBF-LB PROCESSED COMPONENTS

This section outlines the typical process defects found in PBF-LB parts, how these defects affect mechanical properties and how their formation can be mitigated by adjusting the process parameters.

2.4.1 Balling

Balling is a phenomenon during PBF-LB where the deposited melt track does not adequately wet the underlying substrate, leading to spheroidization due to surface tension forces [56]. This is undesired as it creates a beaded melt track that hinders the deposition of subsequent tracks and can lead to the formation of defects [56] [90]. This phenomenon is tethered to the maximum allowable length of the melt pool which is based on the Plateau Raleigh capillary instability [44], see Figure 15. Literature has shown that increasing the laser power [56] [90] [91], decreasing the scan speed [90] [91], decreasing the layer thickness [90] and reducing the oxygen content [90] [92] can help to mitigate this issue. However, the most common understanding of balling is based on the deposition of a melt track onto a substrate made from different material which does not adequately represent what happens during PBF-LB, as the underlying material is the same. In addition, non-equilibrium wetting conditions are present during PBF-LB [93]. Furthermore, balling seems to be more a prevalent issue during single track experiments than during the production of multiple layers [53].

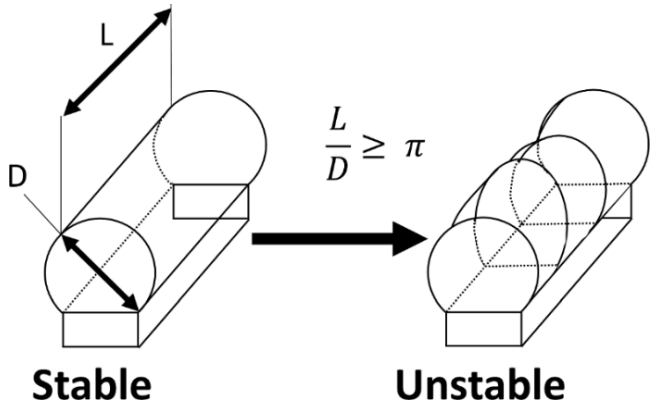

Figure 15: Schematic outlining the criterion for balling, which is defined by the relation between the allowable length of the melt pool (L) and melt track diameter (D). Adapted from [44].

2.4.2 Surface Roughness

Generally, the surface roughness of PBF-LB parts is higher than conventionally produced material. This is undesired as a high surface roughness leads to a degradation in dimensional accuracy [94] as well as a degradation in fatigue life [95]. The formation of high surface roughness stems from two factors. The first is the "stair-case effect" which transpires due to layer by layer approach of PBF-LB, which induces a high surface roughness on curved and inclined surfaces [96], see Figure 16. The second mechanism is the inadequate melting of powder and subsequent balling [56] [91]. Experiments have found that low energy inputs led to insufficient melting of metal particles [91]. Due to the surface tension gradient within the melt pool, these powders are subsequently dragged to the edges, leading to their entrainment and the creation of a very rough surface as these unmelted metal particles accumulate.

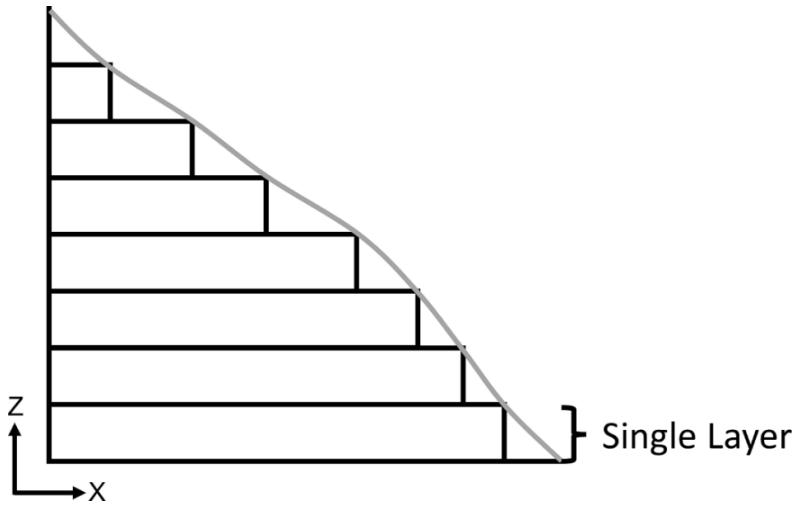

Figure 16: Schematic of the stair-case effect where each deposited layer is outlined in black, while the intended part geometry is outlined in grey. Adapted from [96].

Although a rough surface is an inherent by-product of PBF-LB, it can be somewhat mitigated by adjusting the process parameters. Regarding the stair-case effect, its effect becomes more prevalent as the layer thickness increases [35]. This means that the surface roughness can be improved but at the cost of a reduced build rate. Additionally, the staircase effect is influenced by part geometry and orientation. Lastly, exposure of the part edges using contour scanning can help improve the surface roughness [60]. As for the issues related to inadequate melting, this can be improved by increasing the energy input [38] [91] [95], as this will help facilitate full melting of the powder without the entrainment of particles at the melt pool edge. Melting can also be improved by decreasing the PSD as smaller powder particles are easier to melt [38] [97].

2.4.3 Porosity

Porosity is unwanted by-product of PBF-LB as these defects negatively impact part quality as well as mechanical properties. This section outlines the common types of porosity that form during PBF-LB.

Lack of Fusion

Lack of fusion porosity forms when the energy provided by the laser is insufficient to achieve adequate bonding between deposited layers or melt tracks, see Figure 17. Lack of fusion between melt tracks occurs when the overlap is inadequate, while lack of fusion between layers occurs when the penetration depth is inadequate. The formation of these pores should be minimized as their large and irregular shape make them preferred sites for stress concentration that subsequently reduce static [17] [98] [99] [100] and fatigue properties [18] [101].

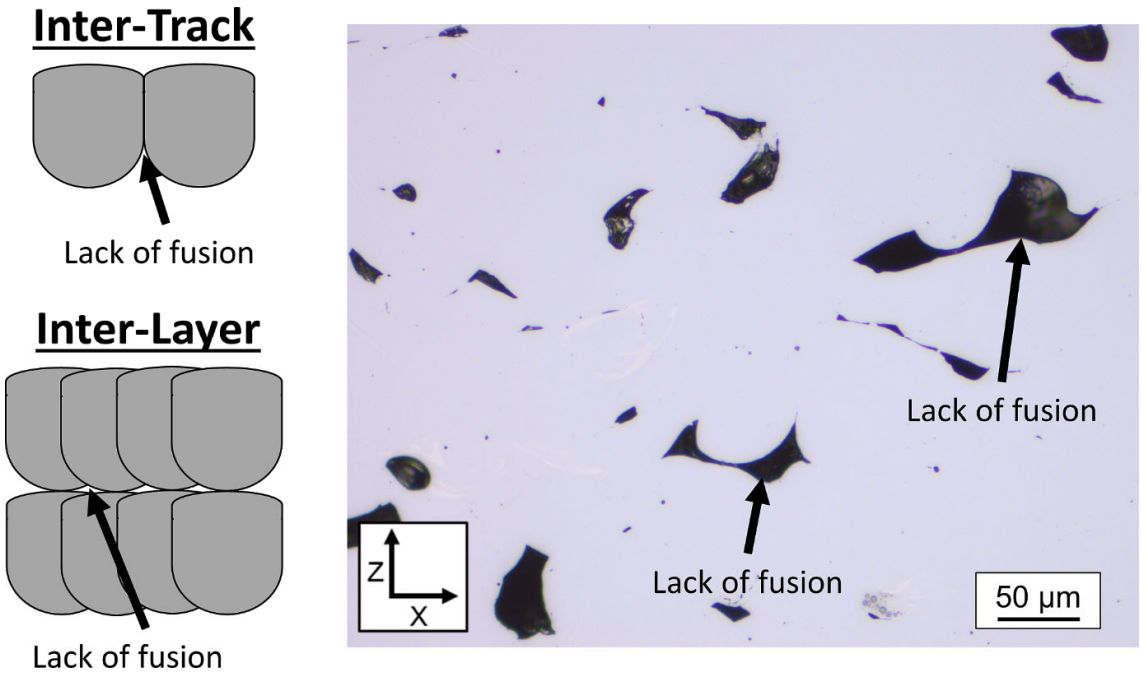

Figure 17: Schematic outlining lack of fusion porosity between melt tracks and layers (left). Example of lack of fusion porosity found in an AISI 4130 low-alloy steel produced by PBF-LB (right).

To mitigate lack of fusion porosity, tuning of the process parameters is required. In terms of laser parameters, it is important to choose inputs that provide the required bonding between deposited melt tracks and layers. This can be attained by decreasing the scan speed or increasing the laser power as both increase the depth and width of the melt pool [48] [49] [52]. Lowering the hatch spacing can also reduce lack of fusion porosity [102] [103], as this reduces the required distance between melt tracks. While lowering the layer thickness can reduce lack of fusion porosity [35] [104] by decreasing the required penetration of the melt pool to achieve proper bonding between layers. In terms of machine parameters, increasing the build plate preheating temperature can improve material densification by increasing the ambient temperature during processing [105]. As for powder parameters, having a coarser PSD can induce lack of fusion porosity [25] [64] [106], as there are fewer fine particles that can fill-in the voids between larger particles. The material properties of the powder are also important as they will affect the size of the melt pool as well as the wetting behavior. As the size of the melt pool is governed by the absorptivity, thermal conductivity, density, heat capacity and melting temperature [34] [55], while the wetting behavior is dictated by the surface tension and viscosity [87] [93]. Lastly, lack of fusion can form due to ejected spatter particles, which can interfere with the laser during flight [78] or become re-deposited on the powder bed [41], leading to a reduced energy input during subsequent passes of the laser beam.

Keyhole Porosity

Keyhole porosity results from instabilities within the vapor depression during keyhole mode melting [107] [108], see Figure 18. In situ observations have found that this porosity forms as the vapor depression collapses, creating a pore that is entrained during solidification due to Marangoni convection [109]. These pores are typically spherical due to pore spheroidization [109] and the hydrostatic pressure acting on the pore by the surrounding liquid [110]. Although keyhole porosity is undesired, it is less detrimental to mechanical properties than lack of fusion [18] [98], as it has more rounded shape. Still, the pronounced presence of keyhole porosity [98], as well as keyhole porosity located close to the specimen surface [15] [111], will negatively impact both static and fatigue properties.

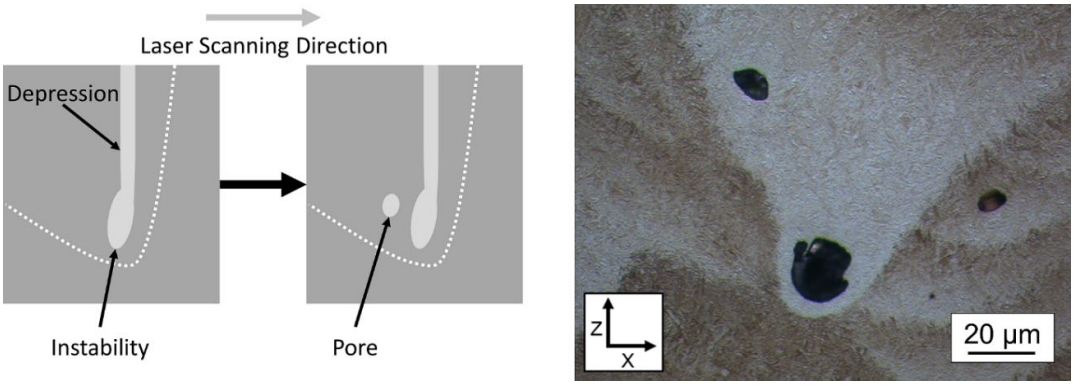

Figure 18: Schematic outlining the formation of keyhole porosity (left), where the dotted white line represents the liquid-solid interface. Adapted from [109]. Example of a keyhole pore located at the bottom of a melt pool in an Fe-0.75C steel produced by PBF-LB (right).

As mentioned earlier, the formation of keyhole porosity is linked to the stability of the vapor depression. This means that adjusting the process parameters to decrease the depth of the vapor depression will decrease the likelihood of forming keyhole porosity. This can be achieved by reducing the energy input, as past works have shown that increasing the scan speed [49], lowering the laser power [49] or increasing the beam diameter [112] can lower the amount of keyhole porosity. Besides laser parameters, the material properties also play a role as these factors will influence absorptivity, thermal conductivity, density, heat capacity, melting temperature and boiling temperature [34] [55] [112], which subsequently influence the depth of the vapor depression.

Entrapped Gas

Entrapped gas porosity relates to small, rounded pores [38] [102], see Figure 20. Unlike lack of fusion or keyhole porosity, their formation is primarily driven by the transfer of residual porosity from the powder feedstock. This has been corroborated by in situ observations where entrapped gas within the powder would transfer to the melt pool before getting entrained during solidification [108] [113]. With that said, the relative transfer of porosity from the powder to part is low (< 10%) as the majority of pores escape before becoming entrained [102] [108]. Other potential sources of entrapped gas porosity during PBF-LB are low packing density of the powder bed [114] and the re-melting of previous defects that contain entrapped gas [102]. The formation of this porosity can be mitigated by ensuring high powder quality where there is limited internal porosity [115].

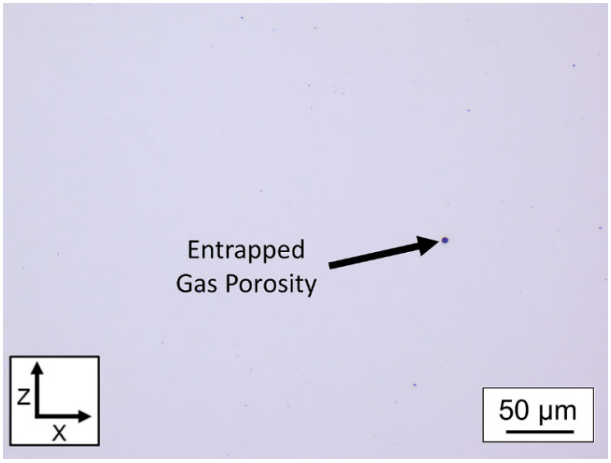

Figure 19: Example of entrapped gas porosity found in an AISI 4130 low-alloy steel produced by PBF-LB.

2.4.4 Residual Stresses

Residual stresses are defined as stresses that remains at equilibrium after a material has experienced non-uniform plastic deformation [116] [117]. Generally, these stresses are categorized by the length scale at which they operate [118]. Type I residual stresses are macro-stresses that act on the entire part, Type II residual stresses are micro-stresses that act on the grain scale level and Type III residual stresses are nano-stresses that act on the atomic scale. In PBF-LB, the focus has been on Type I residual stresses as these can often approach the yield strength of the material [119] [120], leading to part distortion and delamination [121] [122].

The formation of Type I residual stresses during PBF-LB can be traced back to the large thermal gradients of the process [123]. During melt track deposition, a steep temperature gradient develops due to the slow heat conduction of the underlying layers when compared to the newly deposited layer. This causes the new layer to expand and for the underlying layers to restrict said expansion, resulting in compressive stresses in the new layer and tensile stresses in the underlying layers, see Figure 20. As the new layer then solidifies, the melt pool contracts pulling on the underlying layers. At the same time these underlying layers will restrict said expansion, leading to tensile stresses in the newly deposited layer and compressive stresses in the underlying layers, see Figure 20.

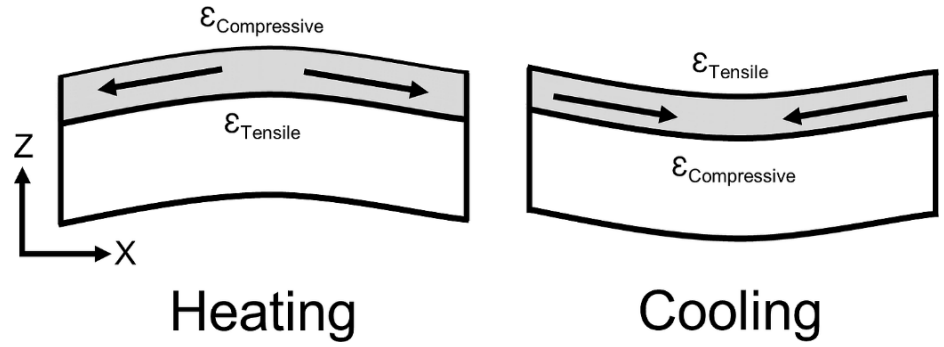

Figure 20: Schematic outlining the formation of residual stress in PBF-LB during heating (left) and cooling (right). The new layer is marked as the grey region, while the underlying layers are marked as the white region. Adapted from [118] [123].

Despite this basic understanding, the nature of residual stress in PBF-LB is complex, as the localized nature of the process means that different regions experience different heating and cooling rates, inducing a non-uniform distribution of residual stress. Generally, past works have shown that the top, side and bottom regions of the specimen are primarily in tension, while the middle regions are in compression [124] [125]. Additionally, the magnitude of residual stress can vary along the laser direction, as residual stress along the longitudinal direction can be 1.5 to 2.5 times larger than residual stress along the transverse direction [126].

The magnitude, orientation and distribution of residual stress is highly dependent upon the chosen process parameters. Regarding laser parameters, a high laser power and a low scan speed generally induce more residual stress [119] [130]. The scan strategy is also an important consideration, as longer scan vectors typically induce more residual stress [126], while the scan orientation [119] [121], dwell time [127] and re-scanning strategy [123] [128] can alter the magnitude of residual stress. Machine parameters are also important, as large layer thicknesses [129] or high build plate preheating temperatures [36] [105] [130] can lower residual stress. Lastly, material properties such as increasing thermal diffusivity or increasing thermal conductivity can help reduce residual stress [118].

Besides rapid cooling, residual stress can also form due to phase transformations within the material. For structural steels, compressive stresses can be introduced during the transformation of martensite, as the shift from austenite to martensite will induce volume expansion since FCC austenite is more closely packed than BCT martensite [131]. The magnitude of this volume expansion is determined by the martensite start temperature (M_S) as well as the degree of alloying [132]. The presence of compressive residual stress has been detected for H13 tool steel produced by PBF-LB [36] [133] [134], indicating that martensite can contribute to residual stress. However, whether martensite or thermally induced stresses dominate is difficult to determine, as the stress state for PBF-LB material is highly localized and will vary greatly depending upon specimen location [125] [134].

2.4.5 Cold Cracking

Another observed defect in carbon-containing steel is cold cracking [36] [122] [134]. These cracks primarily originate at the specimen surface and grow inwards in a direction parallel to the build platform, see Figure 21. Their formation occurs after solidification and can often induce a "blow-up" phenomena after printing has ended, where the powder sitting on top of the specimen is ejected away due to the violence of crack formation [135]. Previous work on PBF-LB tool steel also indicated that these cracks only formed after a certain number of layers have been deposited [136].

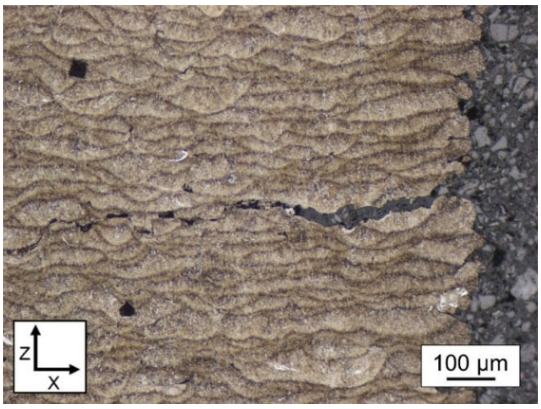

Figure 21: Example of a cold crack in an AISI 4340 low-alloy steel produced by PBF-LB.

The formation of these cracks stem from the combined presence of brittle material and high residual stresses. In structural steel, brittle material is readily available in the form of martensite that forms due to the rapid cooling rates of the process and the high carbon content of the alloys (< 0.3 wt.% C). While residual stresses are readily available due to the rapid cooling rates [118] as well as the formation of martensite [36] [133]. Generally, the susceptibility to cracking increases with carbon content [137], as there is a direct correlation between martensite strength and the amount of carbon [138] [139].

Mitigation of these cracks is primarily achieved by build plate preheating, as this can lower the magnitude of residual stress [36] [105] [130] [134], help lower the cooling rate and help soften the material either by in situ tempering or by the suppression of martensite. The suppression of martensite is possible during PBF-LB as long as the build preheating temperature is above the martensite transformation temperature. This was shown during PBF-LB of H13 tool steel [36], where preheating below 200°C led to compressive stresses related to martensite. While preheating at temperatures above 200°C helped shift to tensile stresses related to rapid cooling of the melt pool. However, suppressing martensite formation alone cannot avoid cold cracking if hard phases are still present, as previous work on high-speed HS6-5-3-8 steel found that increasing the carbon content to achieve a fully austenitic microstructure was not able to avoid cold cracking [140]. Due to this, build plate preheating is often applied during PBF-LB of structural steel.

3 STRUCTURAL STEEL

3.1 DEFINITION

Structural steels are generally defined as iron-based alloys that contain up to 2 wt.% C. Within this alloy group, carbon and low-alloy steel are the most prominent due to their combination of hardness, strength, toughness and wear resistance at low material cost [12] [13] [141]. These properties are primarily derived from the addition of carbon, as this is the principle hardening element for steel [142].

Carbon steels relate to iron-based alloys that have below 2 wt.% in alloying additions, where the Mn, Si, Cu, P and S content cannot exceed 1.65 wt.%, 0.6 wt.%, 0.6 wt.%, 0.04 wt.% and 0.06 wt.%, respectively [12]. They can be further categorized by their carbon content as either low- (up to 0.3 wt.% C), medium- (0.4 to 0.6 wt.% C), high- (0.6-1.0 wt.%) or ultra-high-carbon (1.25 to 2 wt.% C) grades.

As for low-alloy steels, they relate iron-based alloys that have below 10 wt.% in alloying additions, where the Mn, Si and Cu content cannot exceed 1.65 wt.%, 0.6 wt.% and 0.6 wt.%, respectively [12]. These alloys are also categorized by their carbon content as either low- (below 0.3 wt.% C) or medium-carbon (0.3 to 0.6 wt.% C) grades. Compared to carbon steel, low-alloy steels display superior mechanical properties as the enhanced presence of alloying elements improves hardenability and carbide formation, see Figure 22. The addition of alloying elements also influences phase stability, where austenite stabilizing elements widen the temperature range of austenite (e.g., C, Ni, Co and Mn) and ferrite stabilizing elements narrow the temperature range of austenite, expanding the temperature range of ferrite instead (e.g., Cr, Si, S, P and Mo).

Although there are many grades of low-alloy steel, work in this thesis focused on Cr-Mo-Mn (AISI 4130 and 4140) and Ni-Cr-Mo-Mn (AISI 4340 and 8620) compositions that involve the addition of Ni, Cr, Mo, Mn and Si. The impact of each alloying element is briefly summarized below [12] [13]:

- ***Nickel:*** Added to act as an austenite stabilizer and improve corrosion resistance.
- ***Chromium:*** Added to improve hardenability, promote carbide formation and improve corrosion resistance.
- ***Molybdenum:*** Added to improve hardenability and promote carbide formation.
- ***Manganese:*** Added to improve hardenability at moderate cost, form non-harmful sulfides and promote carbide formation.
- ***Silicon:*** Added to help with deoxidation and improve strength in the quenched and tempered condition.

The range of achievable properties is quite broad for carbon and low-alloy steels, see Figure 22, and will depend not only on alloy composition but also on the processing route. At higher temperatures (from 723°C to 1496°C) these alloys are characterized by the FCC austenite (γ) phase, that upon slow cooling will transform into a mixture ferrite (α) and pearlite ($\alpha + Fe_3C$), see Figure 23. As the cooling rate increases the transformation product changes, first to bainite at moderate cooling rates and then to martensite at rapid cooling rates, see Figure 23. Each of these transformation products provide their own combination of properties and are chosen based upon the intended application.

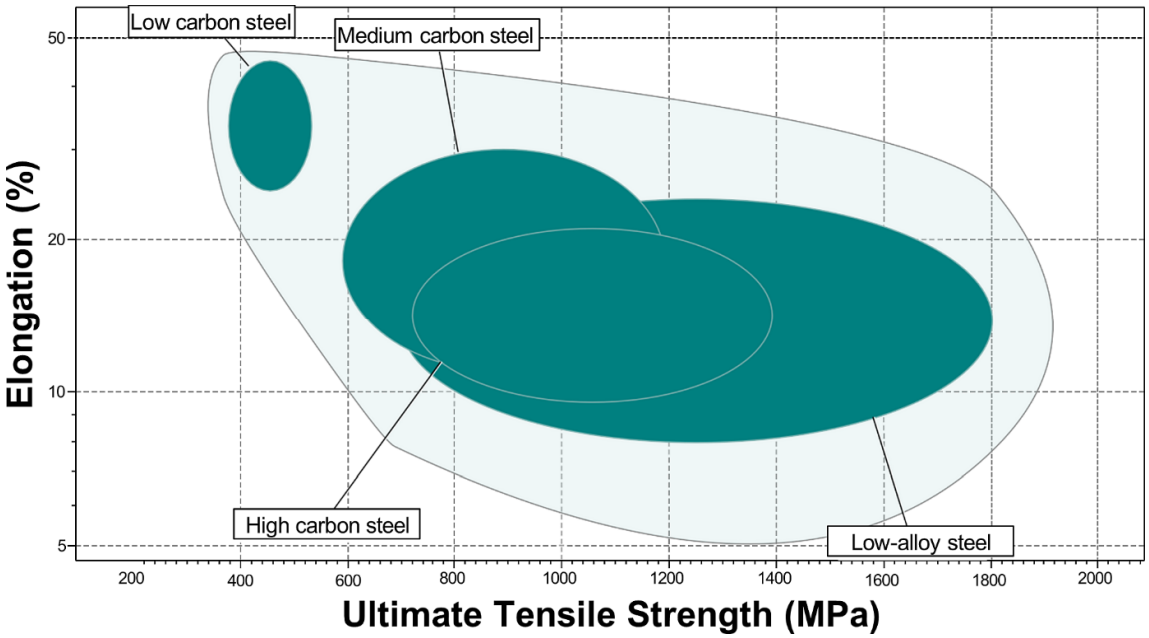

Figure 22: Range of mechanical properties for carbon and low-alloy steels as plotted by Granta EduPack 2021 software [143].

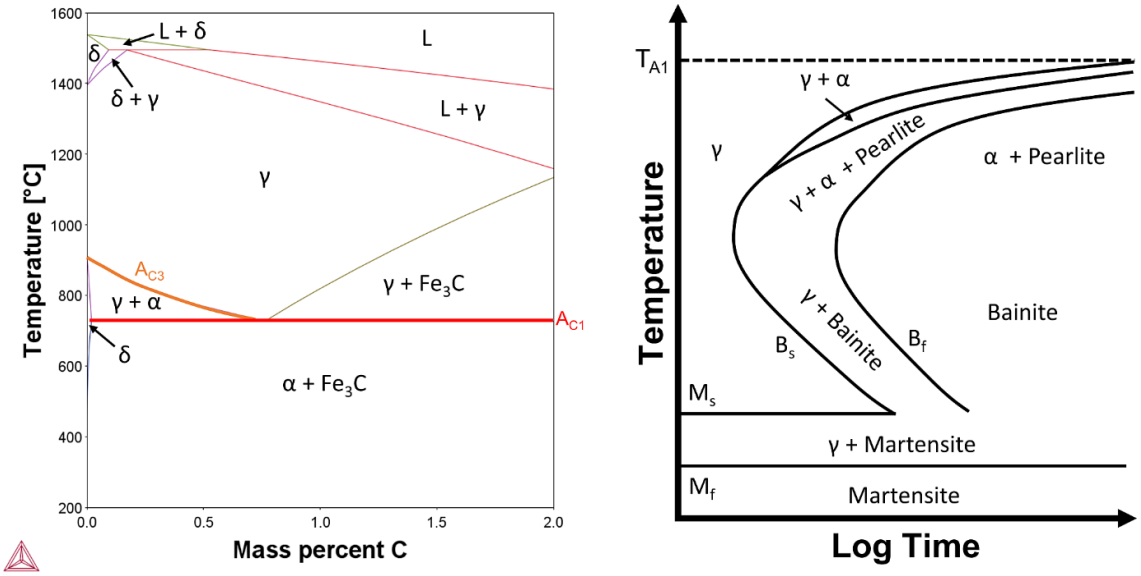

Figure 23: Fe-C phase diagram as calculated by ThermoCalc 2022a software (left). Here the austenite transition temperature (A_{C3}) and austenite eutectoid temperature (A_{C1}) are outlined in orange and red respectively. Schematic time-temperature-transformation diagram for carbon steel (right). Adapted from [142].

3.2 MARTENSITE

This section provides a brief overview of martensite in structural steel, including a description of why it forms, the different types of martensite that can form and where it derives its strength from. It will not attempt to describe the nucleation, kinetics or mechanisms behind martensite as these were considered outside the scope of the thesis work.

3.2.1 Definition & Formation

The name "martensite" was created in 1890 to honor the work of Adolf Martens and describe the hard phase observed in rapidly cooled steel [144]. However, in the present day it is used to describe any diffusionless transformation product that forms during cooling or applied deformation [144] [145].

In structural steel, martensite forms when austenite is cooled at speeds that are faster than the diffusion rate of carbon atoms. This critical cooling rate depends on alloy composition, as this dictates hardenability and defines the ability of steel to delay the decomposition of austenite into ferrite and pearlite. When diffusion is suppressed, carbon atoms cannot escape and will instead become entrapped at octahedral sites of the FCC austenite lattice, inducing the transformation to the BCT lattice of martensite by a diffusionless shear process [145]. Due to the large difference in solubility between FCC and BCT, the BCT lattice of martensite is supersaturated with carbon leading to noticeable lattice distortions. However, these carbon atoms are unlikely to stay at these positions when held at room temperature. Instead, they will segregate to dislocations due to their high diffusivity and the high dislocation density of martensite [131]. To avoid this segregation of carbon atoms, martensite must be cryogenically held after rapid cooling [146].

Since the formation of martensite is both diffusionless and athermal, the amount of transformed martensite depends on the experienced undercooling. The temperature that marks the beginning of martensite formation is referred to as the martensite start temperature (M_s) and represents the required thermodynamic driving force to initiate the shear transformation of austenite to martensite [145]. The temperature that marks the end of martensite formation is referred to as the martensite finish temperature (M_f) and represents the temperature where further cooling does not increase the amount of formed martensite. As the carbon content increases, the martensite transformation temperatures will lower as the increased presence of carbon enhances the shear resistance of austenite. If the carbon content is large enough then the full transformation of martensite cannot be achieved at room temperature, leading to retained austenite [147] [148]. Besides the carbon content, the martensite transformation temperature will lower as other alloying elements are added, except for the addition of Co and Al [145] [149]. There is also a relationship between the martensite transformation temperature and the austenite grain size, where a decrease in grain size will lower the transformation temperature due to a non-chemical contribution to the Gibbs free energy [150] [151].

3.2.2 Morphology & Crystallography

The specific conditions that determine the substructure and morphology of martensite remains poorly defined. However, aspects such as the M_s temperature, critical resolved shear stress for slip and twinning, austenite stacking fault energy and strength of austenite and martensite are important considerations [131]. In carbon and low-alloy steel there are two main martensite morphologies, lath-like and plate-like. Their formation depends upon the carbon content, see Figure 24, as lath martensite is present $\leq$ 0.6 wt.% C, while plate martensite is present $\geq$ 1 wt.% C [131]. In between these compositions, a mixture of lath and plate martensite is expected.

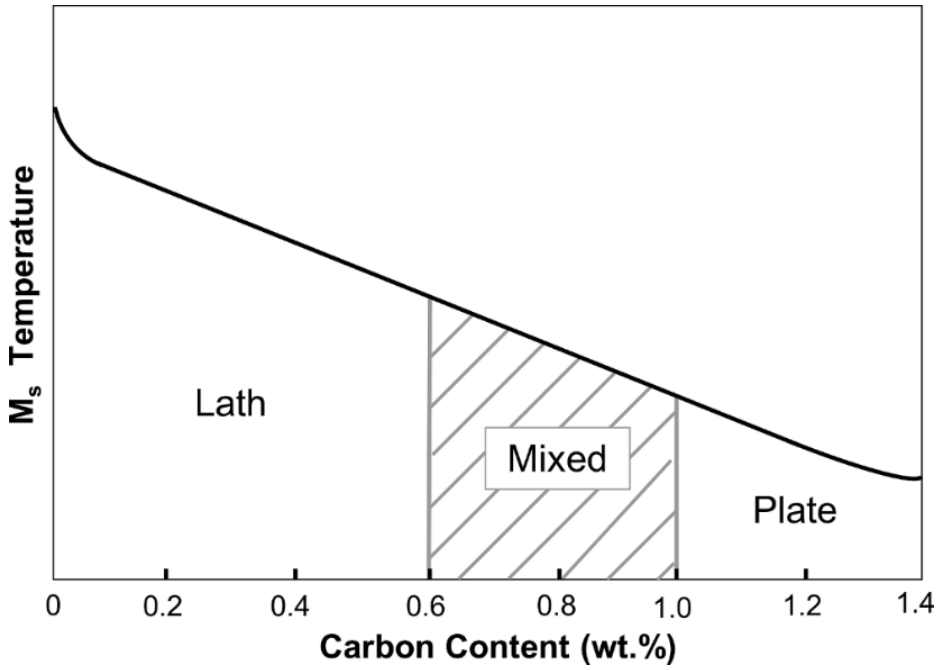

Figure 24: Schematic outlining the change in martensite morphology as a function of the M_S temperature and the carbon content. Adapted from [147].

Lath martensite is characterized by small laths with high dislocation density (10^{14} to 10^{15} m^{-2}), whose growth is subdivided into packets and blocks, see Figure 25. The size of the formed laths is relatively independent of the austenite grain size, carbon content or cooling rate. However, the size of the blocks and packets of lath martensite is dependent on these factors, becoming finer as the carbon content and cooling rate increase [152] [153] and as the austenite grain size decreases [154]. As for plate martensite, it is characterized by larger plate-like structures, that grow across the entire austenite grain and have a central midrib surrounded by partially twinned and then un-twinned regions, see Figure 25. The size of these plates is dictated by the austenite grain size and the nucleation of other martensite plates, where a decrease in austenite grain size or an increase in nucleation rate will lead to finer martensite plates.

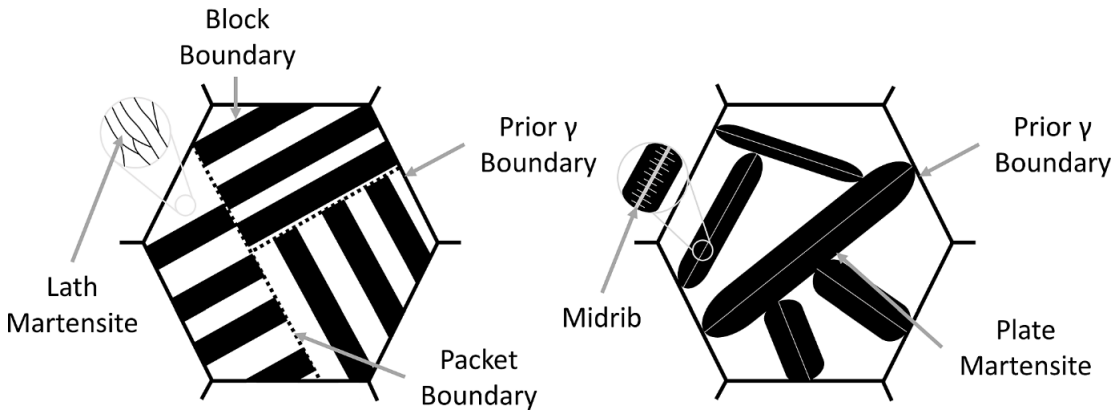

Figure 25: Schematic outlining the typical structure of lath martensite (left) and plate martensite (right). A magnified image of lath martensite (left) reveals the collection of many fine laths within specific packets. While a magnified image of plate martensite (right) reveals the central midrib (grey), surrounded by partially twinned regions (white lines). Adapted from [155] [156] [157].

These martensite morphologies are also distinguishable by their crystallography, as lath martensite satisfies the Kurdjumov-Sachs orientation relationship with a habit plane close to $\{111\}_\gamma$, meaning there are 24 possible crystallographic variants of lath martensite within a single austenite grain [131]. The subdivision of lath martensite also depends on the preferred habit plane and orientation, as growth within packets consists of parallel laths that share a common habit plane, while growth within plates consists of martensite laths that share a common orientation [131]. As for plate martensite, it satisfies the Nishiyama-Wasserman and Greninger-Troiano orientation relationship while having a habit planes close to $\{225\}_\gamma$ or $\{259\}_\gamma$. Here the central midrib, which is considered to be the first part of the plate to form [158], will grow along the preferred habit plane.

3.2.3 Strength of Untempered Martensite

One of the primary benefits of martensite is its high strength. However, the origin of this strength been difficult to define due to the complexity of martensite's structure, the presence of interstitial carbon atoms and the high-density of dislocations and fine twins. As such, there are a variety of proposed strengthening mechanisms including; (i) substitutional and interstitial solid solution strengthening, (ii) carbon atom segregation, (iii) dislocation strengthening, (iv) fine twins, (v) grain size strengthening and (vi) carbide precipitation [144].

Out of these mechanisms, the interstitial dispersion of carbon is considered a major strengthening factor as previous work has shown that an increase in the carbon content will lead to a noticeable increase in hardness and strength [138], where the strength will generally vary as a function of the carbon content [159]. However, it is not necessary for carbon to remain at interstitial sites to provide this strengthening, as work on quenched martensite in low-alloy steel observed a similar strengthening effect when carbon had segregated to dislocations instead of remaining in solid solution [22].

Another important strengthening factor is the austenite grain size, where a Hall-Petch type relationship is often observed [160]. This is because the austenite grain size will determine the size of packets and blocks of lath martensite, while also determining the maximum size of plate martensite. However, smaller grain size features, such as individual lath or plate boundaries, will also hinder dislocation movement and must therefore also be considered when describing martensite's strength.

Lastly the formation of carbide precipitation at dislocations during rapid cooling can also contribute to martensite's strength. However, this phenomenon primarily occurs in martensite with relatively high M_S temperatures [161] and thus cannot describe the strength observed in all forms of martensite.

3.2.4 Tempering of Martensite

After rapid cooling, martensite is hard and brittle, leading to a material with low toughness and ductility. To alleviate this issue, structural steels are often subject to additional tempering which involves heating to an elevated temperature (below the A_{C1}) for a specified period of time. Under these conditions, martensite is highly susceptible to phase transformations due to: (i) The high-density of dislocations and martensite crystal interfaces that create a strong driving force for grain recovery and growth, (ii) The supersaturation of alloying elements that provide a strong driving force for segregation and carbide precipitation, and (iii) The presence of retained austenite that is unstable below the A_{C1} [131].

The time and temperature of tempering will determine the material response, where generally an increase in either factor will lead to a reduction in material hardness for carbon and low-alloy steel [162]. The phase changes that occur during tempering are defined by the tempering temperature and are briefly summarized on the following page [131] [156]:

- ***Stage 1 (100 to 200 °C):*** Involves the precipitation of fine transitional carbides (e.g., M_2C. and $Fe_{2.4}C$). Below 100°C there is the segregation of carbon atoms to regions with high dislocation density. While above 200°C there is the formation of non-transitional carbides (e.g., Fe_3C).
- ***Stage 2 (200 to 300 °C):*** Involves the decomposition of austenite into ferrite and cementite (Fe_3C). Even though the total amount of retained austenite depends upon the alloy composition, some amount is retained regardless. For low- and medium-carbon steels, retained austenite is found between martensite laths, while for high-carbon steels retained austenite is found between martensite plates.
- ***Stage 3 (~250 °C to A_{c1}):*** Involves the formation of cementite at martensite boundaries, prior austenite grain boundaries and inside martensite crystals at dislocation rich regions. This stage occurs in parallel with the formation of cementite during the decomposition of austenite (Stage 2) and extends up to the A_{C1}. As the tempering temperature increases, cementite will coarsen and eventually grow due to Ostwald ripening. The dispersion and fineness of formed carbides is somewhat dependent upon the heating rate, where more rapid heating rates induce a finer and more uniform distribution of carbides [163]. Besides carbide formation, there are substantial changes to the martensite matrix that include recovery, recrystallization and grain growth.
- ***Stage 4 (~500 °C to A_{C1}):*** Involves the formation of alloy-dependent carbides and overlaps with the high temperature range of Stage 3. Higher temperatures are needed for these alloy-dependent carbides as they need substitutional diffusion to become significant and form. These carbides replace less stable cementite either by in situ transformation at the carbide interfaces or by heterogenous nucleation at preferred nucleation sites of martensite.

By correctly tuning the tempering parameters a final microstructure of tempered martensite can be achieved that preserves the high strength of martensite, while still retaining some level of ductility and toughness. However, optimization of these parameters is still the subject of on-going research and is highly dependent upon the initial state of the microstructure as well as the conditions of tempering.

4 PBF-LB OF STRUCTURAL STEEL

4.1 BACKGROUND

To date, few publications have examined PBF-LB of structural steel as fewer than 50 articles have been published on the subject, see Figure 26. This is noticeably below what is published for PBF-LB as a whole, indicating that this research topic is still in its infancy. When examining these published works, most have focused on microstructure characterization, process development and mechanical testing as these are the basic considerations that must be established to ensure the adoption of these alloys. This section aims to outline the current state of the art for structural steels produced by PBF-LB by discussing the research that has been done on these topics.

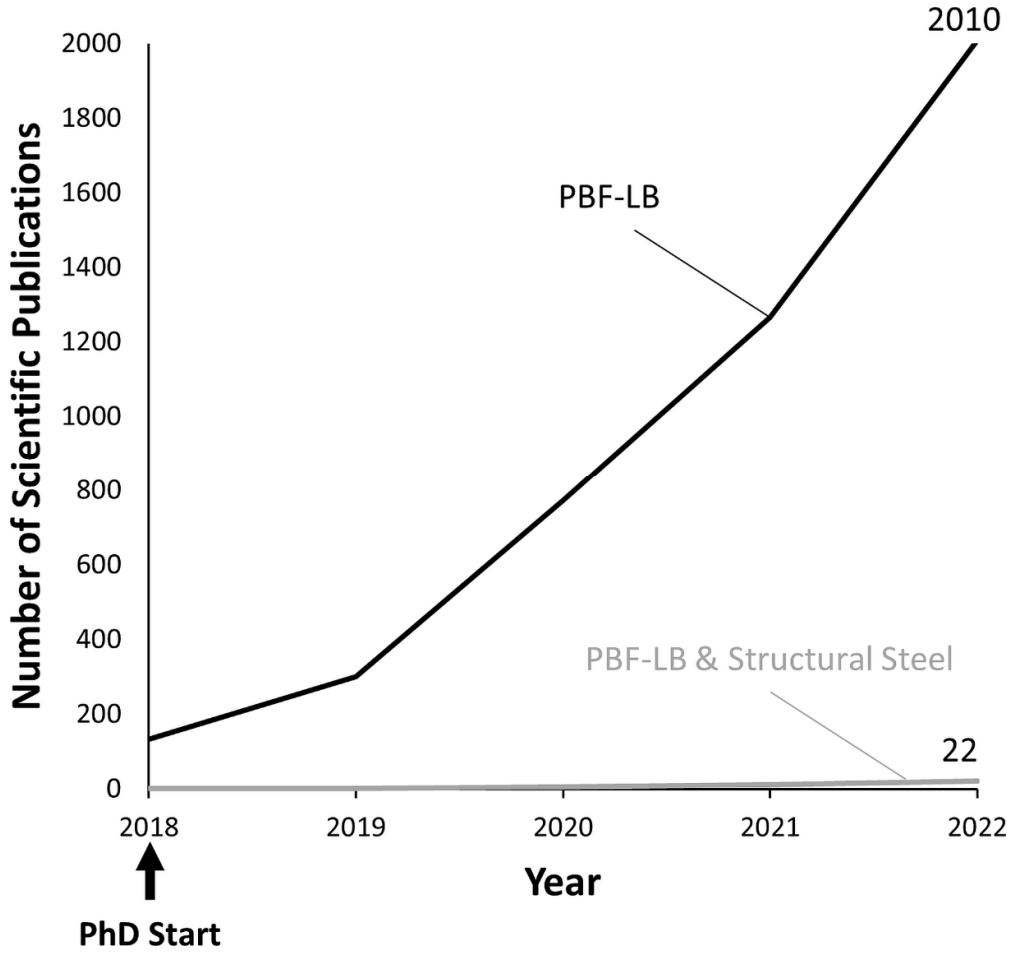

Figure 26: Number of published scientific articles that contain either "PBF-LB" or "PBF-LB and structural steel". When searching for the term PBF-LB the acronyms L-PBF and LPBF were also included. When searching for "PBF-LB and structural steel" carbon steel and low-alloy steel were also included. Data was collected using the online database Scopus.

4.2 MICROSTRUCTURE

Processing of structural steel by PBF-LB leads to a predominantly tempered martensitic microstructure that is often indexed as a BCC phase [54] [164] [165] [166], see Figure 27. Other authors have also mentioned the presence of bainite [172] [176]. This microstructure is fairly complex and contains many features across a variety of length scales.

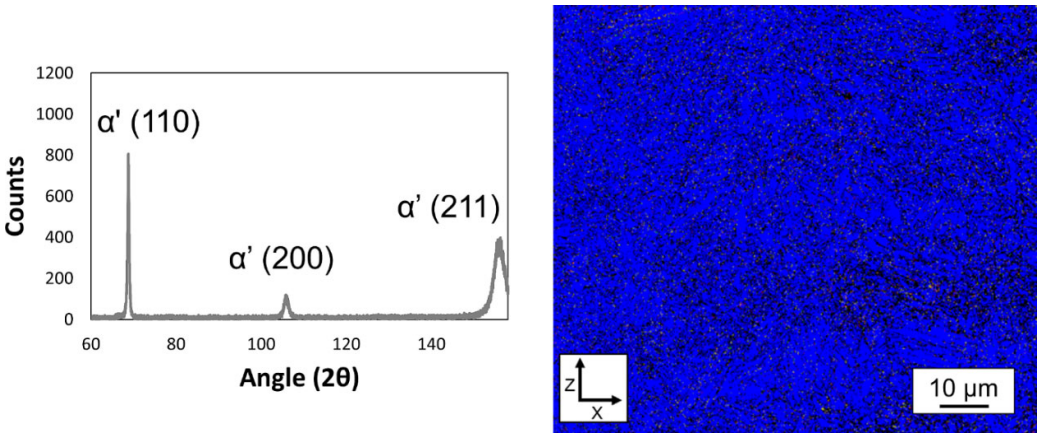

Figure 27: Characteristic XRD peak (left) and EBSD phase map (right) for an AISI 8620 low-alloy steel produced by PBF-LB. In the presented phase map (right) the iron BCC phase is blue, the iron FCC phase is green, the Fe_3C carbide is red and the Cr_7C_3 carbide is yellow

Starting at the millimeter scale, the microstructure is comprised of overlapping boundaries that are preferentially attacked during etching [167] [168] [176], see Figure 29a. These boundaries relate to the portion of material heated above the austenite stability temperature (A_{C1}) during melt track deposition. The melt pool boundaries are also visible, but they are fainter and are revealed as diffuse boundaries instead [167], see Figure 29b.

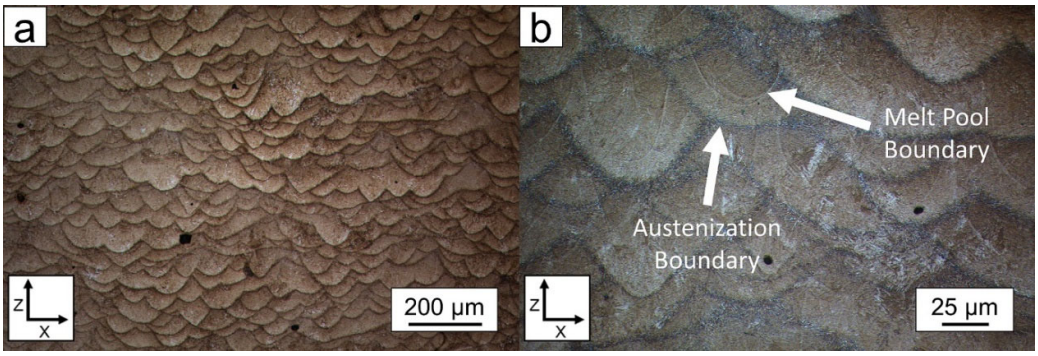

Figure 28: a) Example of the overlapping boundary structure found in Fe-0.45C steel produced by PBF-LB. b) Higher magnification image of (a) highlighting the austenization and the melt pool boundaries respectively.

Moving to the micron scale, the microstructure is extremely fine and lacks distinct crystallographic texture along the building direction, see Figure 29a, which differs from what is observed in more traditional iron-, nickel- and titanium-based alloys [38] [169]. There are also many high-angle grain boundaries that relate to the prior grains of austenite, see Figure 29b. These grains are comprised of both columnar and equiaxed grains that are somewhat aligned with the building direction. However, their orientation and size will vary depending upon the chosen process parameters [170] [171] [172].

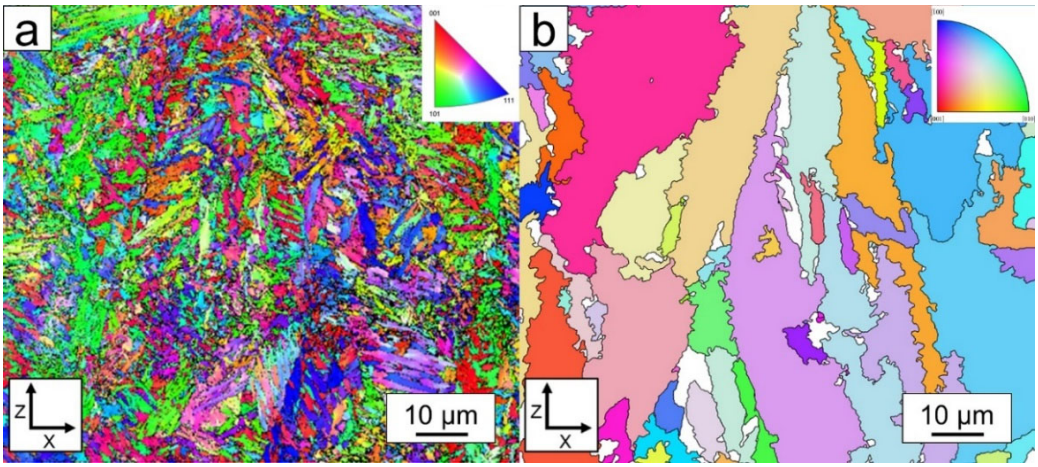

Figure 29: Representative EBSD maps of an AISI 8620 low-alloy steel produced by PBF-LB.
a) Inverse pole figure mapping indicates a fine martensitic structure that lacks a distinct crystallographic texture.
b) Reconstruction of the prior austenite grains as calculated using MTEX software [173].

Lastly on the nanometer scale, a high-density of nano-sized carbides are observed [164] [165] [166] [168] [174], indicating that the material has been tempered during the process, see Figure 30a. Additionally, there is an underlying cellular structure [175] [176], see Figure 30b.

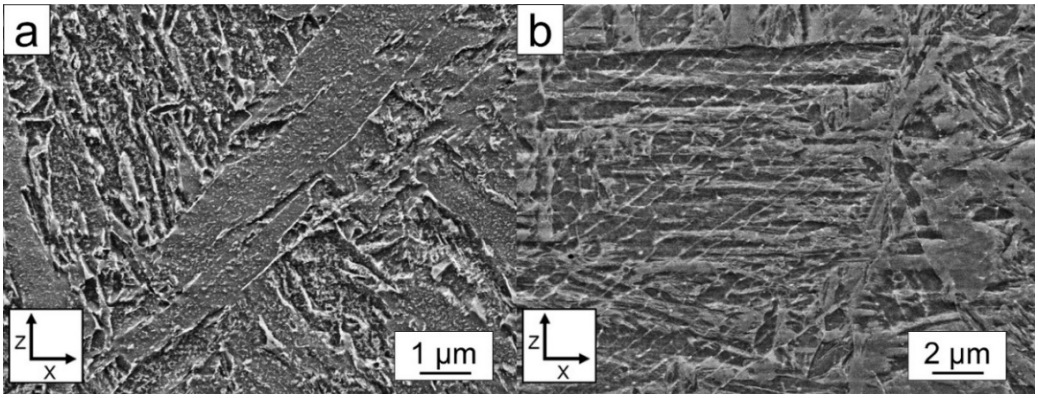

Figure 30: a) AISI 4140 low-alloy steel produced by PBF-LB outlining the fine dispersion of nano-sized carbides. b) AISI 4140 low-alloy steel produced by PBF-LB showcasing the underlying cellular structure.

To understand this microstructure, it is imperative to follow the stages of the local thermal history, see Section 2.3.3. During the first stage, material is rapidly cooled at rates up to 10^4 to 10^6 K/s [47] [68]. Here, it is important to understand what happen during cooling to the solidus temperature (T_s) and what happens during cooling below the T_s.

Regarding cooling to the T_s, a first approximation of the solidification path can be made using the Scheil model which considers perfect mixing of the solute in the liquid, equilibrium at the S/L interface, no diffusion in the solid phase and that the solidus and liquidus are straight line segments [177]. Calculated Scheil curves show that for the structural steels examined in this thesis, the solidification path should follow either L -> δ -> γ or L -> γ depending upon alloy composition, see Figure 31. However, this might not be what happens under rapid cooling conditions, as previous research on welded low-alloy steel found that the primary solidification mode would shift from δ-ferrite to austenite at rapid cooling rates. This was potentially due to the higher dendrite tip temperature of austenite at high solidification velocity, which induces a larger driving force for its formation than δ-ferrite [178].

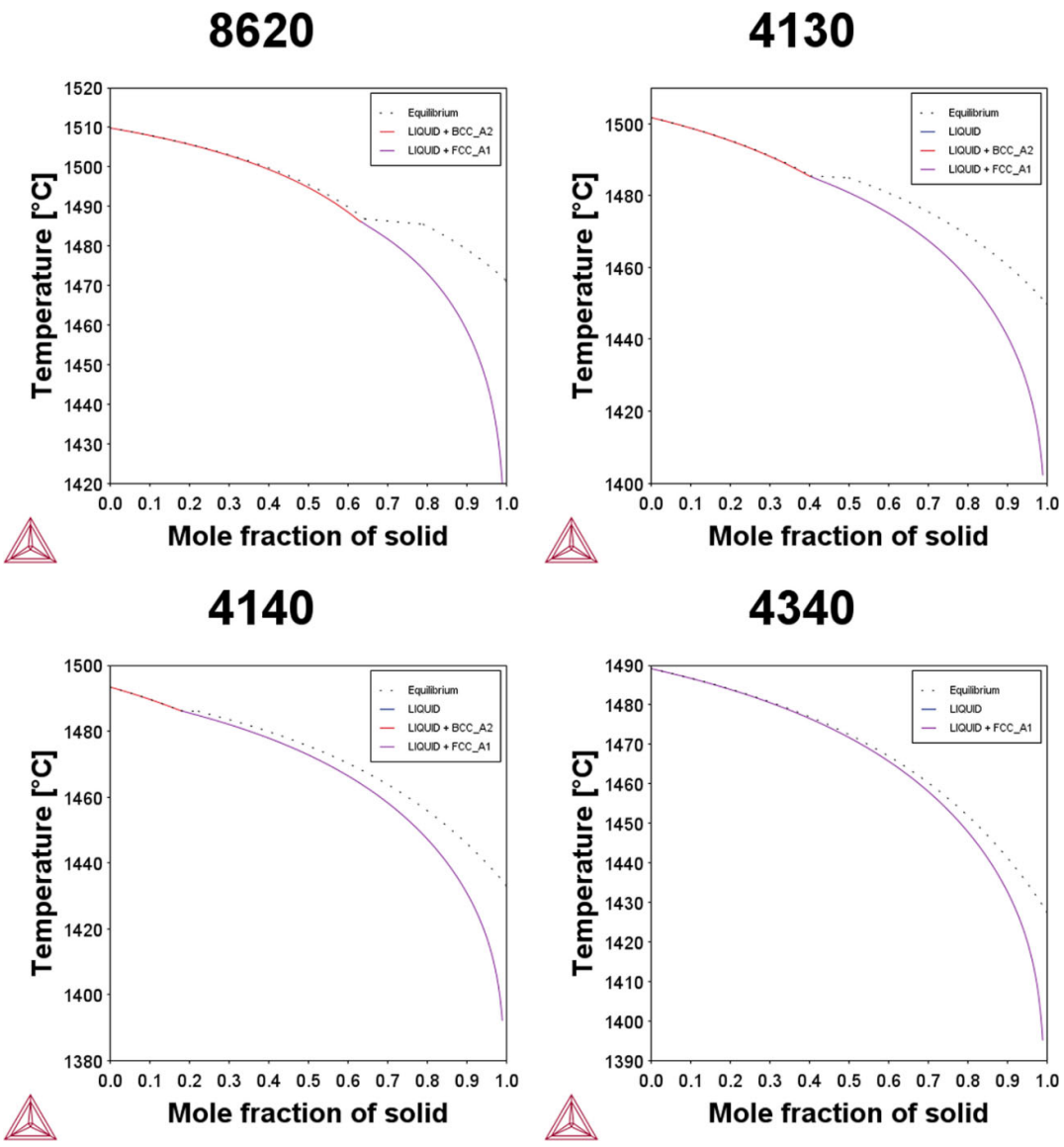

Figure 31: Expected solidification path for AISI 8620, 4130, 4140 and 4340 low-alloy steel as calculated using the Scheil solidification module of ThermoCalc 2022a software [179].

Cooling to the T_s governs the solidification structure of the prior austenite grains and involves the solidification of the melt pool. During this period, grain growth initiates at the melt pool edges and moves towards the center based upon the direction of heat flow and the preferred growth direction, which for cubic materials is <100> [72]. This tendency for preferential growth leads to the formation of textured and columnar grains that are oriented along the building direction [38] [169]. However, the size and orientation of these grains can vary depending upon the applied process parameters [170] [171] [172], as was mentioned previously.

Regarding the underlying solidification structure, this is governed by the local thermal gradient (G) and the local growth rate (R), where the G/R determines the structure morphology, while the G*R (e.g., cooling rate) determines the structure fineness [72], see Figure 32. A fine cellular or dendritic structure is often observed during PBF-LB of iron-based alloys [12] [133] [175] [180] as the large thermal gradients and cooling rates of the process provide the necessary conditions for their formation.

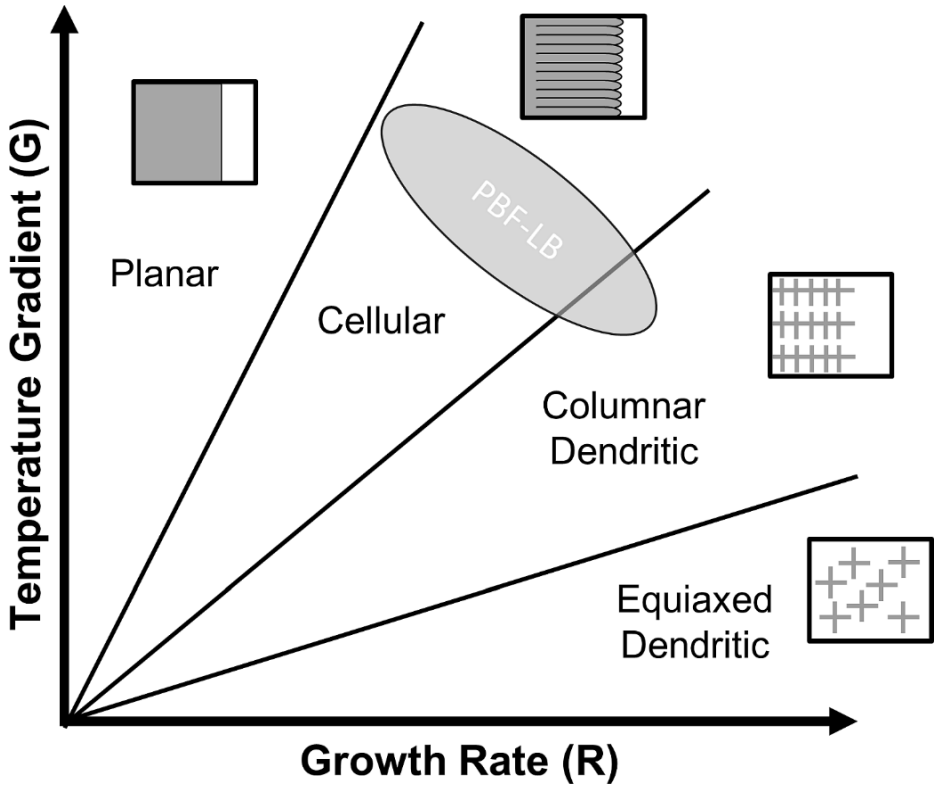

Figure 32: Schematic visualizing the influence of growth rate (R) and temperature gradient (G) on the solidification structure. Adapted from [72].

As for cooling below the T_s, this involves the solid-state transformation of martensite. For the structural steels examined in this thesis the critical cooling rate for a fully martensitic microstructure occurs at approximately 100 K/s, see Figure 33. This is much below the cooling rates of PBF-LB, which indicates that after the first stage of the local thermal history these alloys should consist primarily of untempered martensite. This martensitic microstructure can also explain the lack of distinct crystallographic texture along the building direction, see Figure 29a, as the specimen crystallography will depend upon the preferred habit plane and orientation of martensite, rather than on the direction of heat flow.

Subsequent tempering of this martensite occurs during the various in situ tempering phenomena of the process, see Section 2.3.3. Essentially, anytime martensite is heated below the A_{C1}, see Figure 23, it will experience some degree of tempering, inducing the decomposition of retained austenite, the formation of carbides, and the recovery and growth of the martensite matrix. However, it is difficult to directly apply our classical understanding of tempering to PBF-LB, as the stages of in situ tempering occur cyclically, over much shorter time scales, and at much faster heating and cooling rates [84] [85] [86] [137]. This has made it difficult to precisely identify the state of martensite, the total retained austenite content and the types of carbides that form during the process.

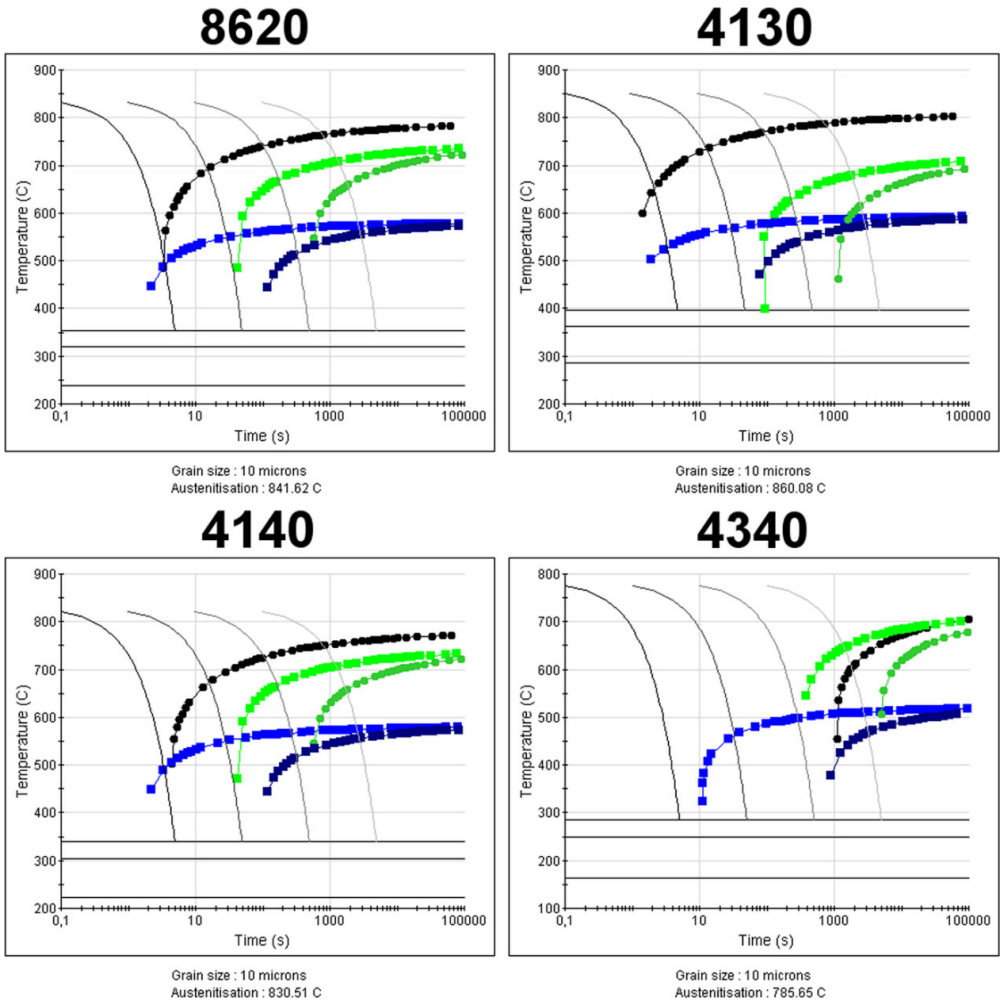

Figure 33: Calculated CCT curves for AISI 8620, 4130, 4140 and 4340 low-alloy steel. The 0.1% transformation for ferrite (black), pearlite (light green) and bainite (blue) and the 99.9% transformation for pearlite (green) and bainite (dark blue) are marked. Additionally, cooling rates of 0.1 C/s (white), 1.0 C/s (light grey), 10 C/s (grey) and 100 C/s (dark grey) are outlined. The perpendicular lines relate to the M_s, M_{50} and M_{90} temperatures respectively. The CCT diagrams were calculated using JMatPro v.11 software [181].

4.3 PROCESS DEVELOPMENT

Generally, process development has focused on the production of high-density and defect free parts, as not meeting either criteria can reduce mechanical properties, see Section 2.4. To achieve this goal, past works have focused on adjusting laser parameters such as the laser power [54] [100] [164] [168] [174] [176] [182] [183] [184] [185], scan speed [54] [100] [168] [174] [176] [182] [183] [184] [185] and hatch spacing [174] [184]. In many cases, process development began with single track experiments that measured the stability of individual melt tracks to determine the suitability of different laser powers and scan speeds [54] [168] [176] [183]. From these experiments, it was found that if the correct laser parameters were chosen relatively high-density parts (> 99%) could be produced, as long as parameters that induced lack of fusion porosity (low laser power + high scan speed), keyhole porosity (high laser power + low scan speed) and balling (high laser power + high scan speed) were avoided. Despite these findings, few works have articulated these results into detailed process maps [54] [100] [165] [168] [174] [183], making it difficult for other researchers to identify the required process parameters to produce high quality structural steels by PBF-LB.

Process development dealing with machine and powder parameters has received little attention in literature for these alloys. In terms of machine parameters, only the impact of layer thickness has been reported on [115]. As for powder parameters, the majority of research has focused on the use of water atomized powder versus gas atomized powder [165] [186] [187], as water atomized powder can take advantage of higher production rates and lower consumable costs, representing a potentially cheaper alternative [188]. The impact of internal powder porosity [113] [115] and particle size distribution [115] has also been discussed. However, detailed investigations that examine the impact of powder parameters remains underexplored.

There is also limited work that has detailed the formation of cracking in structural steels produced by PBF-LB. With regards to cold cracking, although some studies have mentioned its existence [19] most have not and have instead applied build plate preheating to mitigate or avoid this issue. This has led to a limited understanding as to why these cold cracks form and how the processing parameters can be adjusted to mitigate their formation. Other forms of cracking have also been reported on, as the prevalence of severe micro-cracking was observed in AISI 4140 low-alloy steel produced by PBF-LB [100] [174]. These works found that this micro-cracking primarily occurred inside of the specimen and would become more prominent as the energy input increased [100]. However, there remains a lack of data and understanding on the subject.

4.4 MECHANICAL PROPERTIES

A summary of the reported mechanical properties for structural steels produced by PBF-LB is presented in Table 2. From this summation there are three main takeaways. The first is that some reported values indicate that structural steels can achieve a good combination of strength, ductility and toughness [54] [168] [175] [176] [182] [183] [189] [190] that meet or exceed the properties of traditionally produced alloys, see Figure 22. This indicates that there is some level of suitability for PBF-LB.

The second takeaway is that there is some degree of directional anisotropy, as specimens produced in a vertical orientation generally underperformed when compared to those produced in a horizontal orientation [19] [165] [168] [182] [185] [190] [191]. Said anisotropy is somewhat common for alloys produced by PBF-LB. One of the main causes are the large columnar grains that form during the process that are preferentially oriented along the building direction [38] [170]. These elongated grains subsequently lower the strength of vertically orientated specimens, as the loading direction will be perpendicular to these grains during mechanical testing [192]. Directional anisotropy can also be induced by preferentially oriented defects that are perpendicular to the loading direction [193]. Previous works have tried to utilize post heat treatment to alleviate these issues, however, they could only normalize the strength of differently oriented specimens and not the elongation [165] [185].

The third takeaway is that despite the high performance of the alloys there is not a consensus on mechanical properties, as instead there is a wide range of achievable properties for a single alloy. A potential cause is the disparity in formed defects between different works, as some have reported noticeable lack of fusion porosity and micro-cracking. Still, there are differences in mechanical properties for the same alloy when comparing specimens that were produced high-density and defect-free. This has made it difficult to discern if this inconsistency in mechanical properties is an inherent behavior of structural steel or if it is a defect response that is related to processing issues.

Table 2: Summary of the as-built mechanical properties for structural steels produced by PBF-LB. Powder type describes the atomization process of the powder and is listed as either water atomization (WA) or gas atomization (GA). N/A was listed under build plate preheating when the parameter was not specified by the authors. Horizontal and vertical mechanical properties were denoted as H and V respectively.

	Powder Type	Build Plate Preheating (℃)	Yield Strength (MPa)	Ultimate Tensile Strength (MPa)	Elongation (%)	Charpy Impact (J)	
AISI 4130	WA	N/A	(H) 1060 to 1070 (V) 925 to 972	(H) 1155 to 1160 (V) 1012 to 1072	(H) 1.9 to 2.5 (V) 1 to 3.6	-	[191]
	GA	N/A	(H) 1250 ± 15 (V) 1166 ± 5	(H) 1419 ± 30 (V) 1277 ± 7	(H) 3.4 ± 0.6 (V) 6.3 ± 0.9	-	[165]
	WA	N/A	(H) 1072 ± 2 (V) 981 ± 4	(H) 1168 ± 17 (V) 1059 ± 13	(H) 2.5 ± 0.1 (V) 3.2 ± 1.5	-	
	GA	160℃	1243 ± 25	1449 ± 19	15.5 ± 0.8	-	[54]
AISI 4140	GA	200℃	(V) 1148 ± 37	(V) 1260 ± 11	(V) 1.15 ± 0.3	-	[100]
	GA	200℃	(V) 1175 ± 5	(V) 1280 ± 10	(V) 7.2 ± 2.8	-	[174]
	GA	80℃	(H) 1365 ± 43 (V) 1281 ± 4	(H) 1526 ± 40 (V) 1438 ± 3	(H) 13.8 ± 0.7 (V) 12.4 ± 1.5	(H) 34.8 ± 4.5 (V) 32.1 ± 3.6	[182]
AISI 4340	GA	50 to 80℃	(H) 1565 ± 24 (V) 1551 ± 36	-	(H) 9.2 ± 0.7 (V) 4.1 ± 0.8	-	[19]
	GA	300℃	(H) 1000 ± 26 (V) 760 ± 46	(H) 1070 ± 20 (V) 1020 ± 70	(H) 17.4 ± 0.6 (V) 15.1 ± 1.6	(H) 87 ± 12 (V) 105 ± 3.5	[185]
	GA	N/A	(V) 1240	(V) 1429	(V) 15	-	[175]
AISI 5115	GA	80 to 600 ℃	340 to 1030	514 to 1113	3.2 to 12.4	-	[194]
AISI 4820	GA	N/A	(H) 1048 to 1096	(H) 1126 to 1208	(H) 5.1 to 17.4	-	[164]
E185 AMPO	GA	25℃	1070 ± 20	1150 ± 10	15 ± 1.5	142 ± 10	[189]
AF-9628	GA	N/A	(H) 1080 to 1110 (V) 1040 to 1110	(H) 1400 to 1430 (V) 1310 to 1380	(H) 7.7 to 10.2 (V) 7.4 to 10.9	-	[168]
	GA	N/A	(H) 1530 ± 8 (V) 1526 ± 5	(H) 1700 ± 3 (V) 1705 ± 3	(H) 11.5 ± 0.4 (V) 10.5 ± 0.7	-	[190]
	GA	N/A	(V) 1393 to 1670	(V) 1750 to 2085	(V) 6 to 14	-	[176]
	GA	N/A	(H) 1527	(H) 1815	(H) 19.7	-	[183]

5 EXPERIMENTAL METHODS

5.1 MATERIALS

Carbon Steel

Pre-alloyed, gas atomized carbon steel powders, supplied by Höganäs AB, were used in this thesis. In total, six grades of carbon steel were examined that had carbon contents between 0.06 to 1.1 wt.% C, see Table 3. These carbon steel powders had a supplied sieve fraction of approximately 20 to 65 µm from the supplier.

Table 3: Chemical composition of the examined carbon steel powders in wt.%.

	C	Si	Mn	S	O	N
Fe-0.06C	0.06	0.10	0.06	0.008	0.12	0.006
Fe-0.12C	0.12	0.09	0.09	0.011	0.05	0.008
Fe-0.2C	0.20	0.10	0.09	0.007	0.04	0.007
Fe-0.45C	0.45	0.18	0.15	0.007	0.03	0.012
Fe-0.75C	0.75	0.18	0.08	0.007	0.07	0.013
Fe-1.1C	1.10	0.16	0.08	0.007	0.05	0.008

Low-Alloy Steel

Pre-alloyed, inert gas atomized low-alloy steel powders, supplied by Höganäs AB and Sandvik Osprey™, were used in this thesis. In total, four grades of low-alloy steel powders were studied, specifically AISI 4130, 4140, 4340 and 8620. Analysis of the AISI 4140, 4340 and 8620 grades involved a range of compositions that are outlined in Table 4. The inert gas atomized powders had supplied sieve fractions of approximately 20 to 53 µm and 15 to 45 µm respectively, from the suppliers.

Table 4: Chemical composition of the examined low-alloy steel powders in wt.%.

	C	Ni	Cr	Mo	Mn	Si
4130	0.34	-	1.0	0.20	0.60	0.30
4140	0.38-0.47	-	1.0-1.1	0.20-0.23	0.60-0.77	0.20-0.29
4340	0.43	1.9	0.9-1.0	0.30	0.60	0.17
8620	0.20	0.6-0.7	0.5	0.22-0.23	0.70-0.80	0.32-0.35

5.2 PBF-LB

PBF-LB was conducted using an EOS M100 (EOS GmbH, Germany) and an EOS M290 (EOS GmbH, Germany). The EOS M100 was used to produce carbon and low-alloy steel samples in *Paper I, Paper II, Paper III, Paper IV* and *Paper V*, while the EOS M290 was used to produce low-alloy steel samples in *Paper VI*. Both machines were equipped with an Yb-fiber laser source. However, there were differences between the machines in terms of the build area, laser beam diameter, nominal laser power and preheating temperature, see Table 5. During processing an oxygen content of approximately 0.1% was maintained for both machines using Ar as the shielding gas.

Table 5: Technical data for the EOS M100 and EOS M290 machines.

	EOS M100	EOS M290
Build Area	ø 100 x 95 mm	325 x 250 x 250 mm
Max. Laser Power	200 W	400 W
Laser Diameter	~40 µm	~100 µm
Build Plate Preheating	N/A	Up to 180°C

Process development for the carbon steels in *Paper I* and *Paper III* involved the production of 5 x 5 x 5 mm^3 specimens using an EOS M100 at VEDs of 60 to 200 J/mm^3. To vary the VED, the scan speed was altered while maintaining a set layer thickness (20 µm), hatch spacing (70 µm) and laser power (110 W). These values were chosen based off a previous study by the authors [195]. Process development of the low-alloy steels in *Paper IV* involved the production of 10 x 10 x 10 mm^3 specimens using an EOS M100, at VEDs of 60 to 220 J/mm^3 and laser powers of 110 to 170 W. To vary the VED at each laser power, the scan speed was adjusted while using a set layer thickness (20 µm) and hatch spacing (70 µm). Additional process development for the low-alloy steels in *Paper VI* was carried out using an EOS M290. Said process development involved the production of 10 x 10 x 10 mm^3 specimens at VEDs of 60 to 200 J/mm^3 and build plate preheating temperatures of 25 to 180°C. To vary the VED, the scan speed was altered while using a set layer thickness (20 µm), hatch spacing (70 µm) and laser power (170 W). The scanning strategy for all produced specimens involved a 5-mm stripe pattern and a scan rotation angle of 67˚. Additionally, there were no up-skin or down-skin applied during exposure.

5.3 Specimen Preparation

5.3.1 Metallography

To investigate part quality and microstructure, metallographic preparation was conducted prior to analysis. An overview of the metallography applied in this thesis is presented in Figure 34.

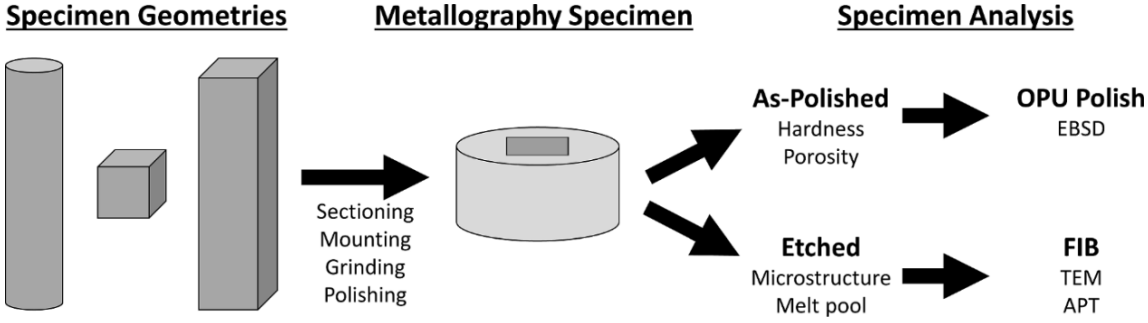

Figure 34: Overview of the metallography used to prepare specimens.

Sectioning was conducted using a Buehler ISOMET 2000 precision saw (Illinois Tool Works, USA) along the *XZ* plane of the specimen, where the *X*-direction related to the direction of gas flow while the *Z*-direction related to the building direction, see Figure 35. After sectioning, the specimens were mounted in resin using an Struers Citopress machine (Struers, Denmark) and then ground + polished using a Struers TegraPol machine (Struers, Denmark). The as-polished specimens were then used to analyze defects and to conduct hardness measurements. Polished specimens were also analyzed using electron backscatter diffraction (EBSD); however, these specimens underwent additional polishing with OPU suspension. The general procedure for grinding and polishing is outlined on the following page:

- Plane grinding with SiC-foil #230 until plane
- Grinding with progressively finer SiC-foil until reaching SiC-foil #4000
- Polishing with 3 µm and 1 µm diamond suspension
- Polishing with OPU suspension (only for EBSD)

To reveal the microstructure, specimens were etched using Nital (3%). These etched specimens were used for analyzing the microstructure and to measure the melt pool depth. They were also used as the precursor for focused ion beam (FIB) production of atom probe tomography (APT) and transmission electron microscopy (TEM) specimens in *Paper V*. These FIB lift-out specimens were produced using a FEI Versa 3D focused ion beam scanning electron microscope (Thermo Fisher Scientific, USA).

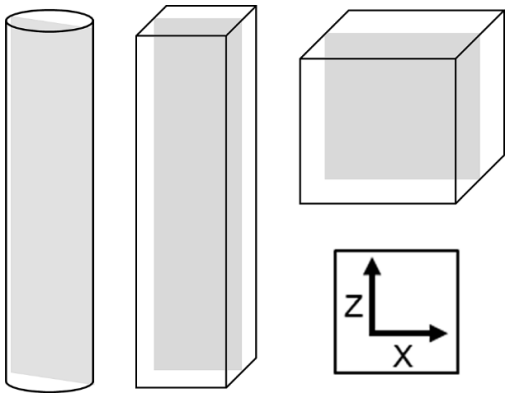

Figure 35: Schematic outlining how sectioning was conducted along the *XZ* plane for each specimen.

5.3.2 Fractography

Fractography analysis was carried out in *Paper I* and *Paper IV* on specimens with cold cracking defects. These specimens were prepared by cutting a 1 to 2 mm incision on the side-surface that was opposite to a cold crack. This incision was then used to initiate specimen fracture and reveal the cold crack surface that was further analyzed using scanning electron microscopy, see Section 5.4.4.

5.3.3 Heat Treatment

In *Paper IV* additional heat treatment was carried on select specimens using a Carbolite CWF 1200 box furnace (Verder, Germany). The first heat treatment involved austenization at 900°C for 1 hour followed by quenching in oil, while the second heat treatment involved the previously mentioned quenching procedure following by tempering at 500°C for 2 hours. Each of these heat treatments was carried out within a protective Ar atmosphere (purity >= 99.998%).

5.4 Analysis Techniques

5.4.1 Powder Characterization

Characterization of the powder feedstock in *Paper III* was carried out using optical microscopy, see Section 5.4.3, and was carried out in *Paper III* and *Paper VI* using scanning electron microscopy, see Section 5.4.4. The powders analyzed by optical microscopy were studied to measure internal defects and were prepared using the method outlined in Section 5.3.1. Powders analyzed by scanning electron microscopy were used for determining the particle morphology and were prepared by mounting the powders onto aluminum plates via powder pressing.

The particle size distribution (PSD) was measured for each powder by means of laser diffraction using a Malvern Mastersizer 3000 (Malvern, UK). Prior to each measurement the powder sample was homogenized for 20 to 30 minutes, and each measurement was repeated 5 times using dry powder.

The flow behavior of the powders in *Paper III* was measured using a revolution powder analyzer (Mercury Scientific Inc, USA). For each measurement a tapped powder sample of 29 cm^3 was used using a drum insert of ø 50 mm, a rotation rate of 0.6 RPM, an image rate of 15 FPS and a preparation time of 30 s. Prior to each measurement a fluidization treatment for powder conditioning was carried out based on the recommendation of Spierings et al. [196]. Each of these measurements were repeated 5 times and 150 avalanches were detected for each measurement.

5.4.2 Chemical Analysis

Measurement of the oxygen content in *Paper I* and *Paper III* was carried out via inert gas fusion. This analysis involved the heating of specimens in a graphite or ceramic crucible to approximately 3000°C in an inert gas atmosphere. At this temperature dissolved gases are driven away and in the case of oxygen will react to form carbon monoxide (CO) and carbon dioxide (CO_2). The formation of these gases can then be quantified using infra-red detectors that can measure the total released oxygen content [117]. For the inert gas fusion analysis, a LECO ON836 elemental analyzer (LECO Corporation, USA) was used following the EN ISO 15350 standard [197].

Measurement of the carbon content in *Paper I* and *Paper III* was carried out via combustion analysis. This analysis involved the combustion of specimens inside an induction furnace that had a high flow of oxygen. Carbon released by the specimens would then react with this oxygen to form CO and CO_2 gas, which could then be measured via infrared absorption [118]. For combustion analysis, a LECO CS844 elemental analyzer (LECO Corporation, USA), was used following the EN 10276-2 standard [198].

5.4.3 Optical Microscopy (OM)

Optical microscopy (OM) was conducted using a Zeiss Axiovision 7 light optical microscope (Carl Zeiss AG, Germany). Imaging of as-polished specimens involved the measurement of specimen density and the characterization of porosity. To measure the specimen density in *Paper I, Paper III, Paper IV,* and *Paper VI,* images with a resolution of at least 1.08 µm/pixel were analyzed using ImageJ software [199]. This was done by cropping and converting the images to a binary format which would isolate porosity within the specimen, see Figure 36. In this state, the total porosity area could be measured and subsequently used for determining the specimen density. This technique was chosen due to its relatively good agreement with specimen density measurements conducted by computer tomography [200].

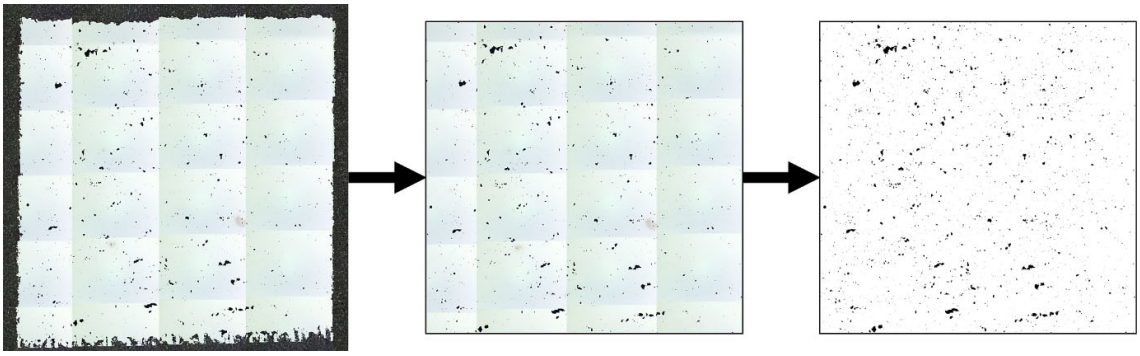

Figure 36: Example of cropping (middle) and conversion (right) of OM images into a binary format to measure specimen density. Specimen is from an AISI 8620 low-alloy steel.

To further characterize the specimen porosity, quantitative image analysis was carried out in *Paper I* and *Paper IV*. This analysis involved the measurement of pore shape characteristics using the shape descriptor plug-in of the ImageJ software. During said analysis, any pore below 20 μm^2 and any non-porosity defect (e.g., cold cracking) were filtered away.

In terms of shape characteristics, the Feret diameter was used to determine the pore size, as it represents the longest distance between any two points, see Figure 37. The roundness and aspect ratio were used for determining the pore shape. The aspect ratio is a dimensionless shape factor that describes the ratio between the largest dimension (c) and the smallest dimension (a), see Figure 37. Here, a value of 1 represents a perfect circle, while a value above 1 represents a deviation to an irregular shape. The roundness is a dimensionless shape factor that also describes how close a shape is to a perfect circle. Here a value of 0 represents a completely irregular shape, while a value of 1 represents a perfect circle. The roundness is calculated using the pore area in combination with the length of the major axis (c):

$$Roundness = \frac{4*Area}{\pi*c^2} \tag{6.1}$$

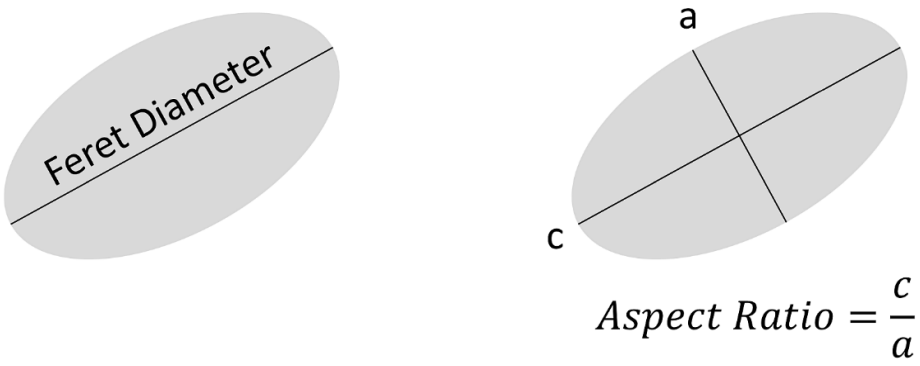

Figure 37: Schematic outlining the ferret diameter (left) and aspect ratio (right).

OM images of etched specimens were used for analyzing the microstructure and to measure the melt pool depth. The melt pool depth was determined by measuring the top layer depth that was preferentially revealed after etching with Nital, see Figure 38.

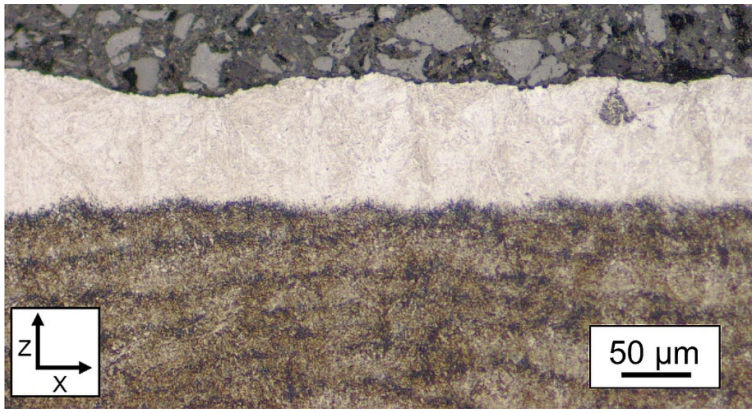

Figure 38: Example of the top layer in an AISI 4340 low-alloy steel produced by PBF-LB.

5.4.4 Scanning Electron Microscopy (SEM)

Scanning electron microscopy (SEM) is a technique used for generating high-resolution images with a large depth of field. These images reveal information regarding specimen topology, composition, crystallography and phase composition [201]. SEM begins with the creation of a focused beam of energized electrons using a high-voltage source (up to 30 keV). After emission and refinement, the beam penetrates the specimen and interacts with electrons that are down to 1 to 5 µm below the surface. This interaction produces a combination of secondary electrons (SE), backscattered electrons (BSE), Auger electrons and characteristic X-rays, see Figure 39. The depth of the interaction depends upon the specimens' atomic mass, as well as the incidence angle and the accelerating voltage of the beam [202].

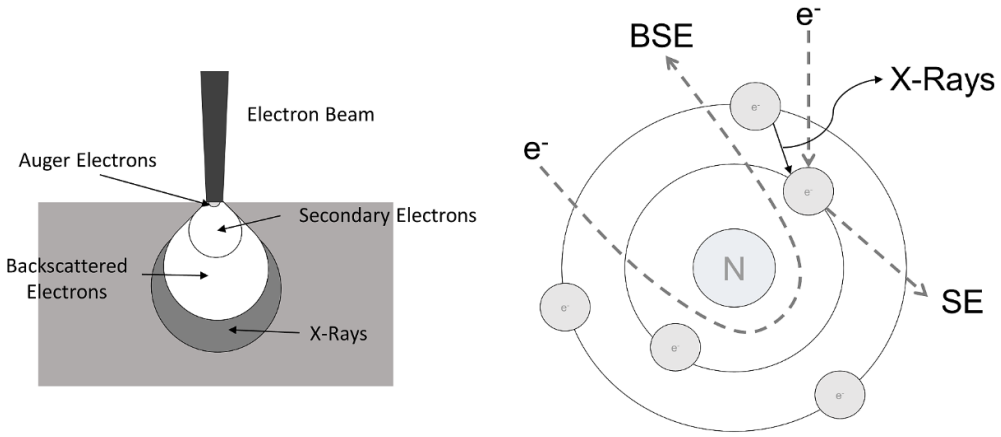

Figure 39: Schematic of the interaction volume (left) and creation of incident electrons (right) during SEM. Adapted from [202].

However, the depth of information depends on the escape depth of the different electrons or characteristic X-rays. SE are electrons that escape with low kinetic energy (< 50 eV) and were knocked out of their atomic orbit due to incoming incident electrons, see Figure 39. As SE are only able to escape in regions close to the surface, they will primarily provide topological information. On the other hand, BSE are higher-energy electrons that will approach and interact with the atomic nucleus before scattering, see Figure 39. Since the interaction depth of BSE is greater, they do not provide the same topological contrast. However, they will provide compositional contrast, as the atomic mass will influence the observed brightness [202]. Auger electrons are emitted from atomic layers near the specimen surface and can provide information regarding the surface chemistry. While X-rays are emitted when incident electrons knock out inner-shell electrons, causing outer-shell electrons to migrate and fill their place, see Figure 39. These emitted X-rays can provide information regarding the chemical composition [202], and will be associated with the greatest information depth.

In this thesis, SEM was used to characterize powders in *Paper III* and *Paper VI* and to characterize the produced specimens in *Paper II, Paper IV, Paper V* and Paper *VI*. SEM was carried out using a LEO Gemini 1550 HR-SEM (Carl Zeiss AG, Germany).

5.4.5 Electron Backscatter Diffraction (EBSD)

Electron backscatter diffraction (EBSD) is a SEM-based technique that can investigate the local crystallographic texture, grain characteristics, phase composition, and strain [203]. This information is gathered by analyzing data that is generated during the interaction between the electron beam and the specimen. When this interaction occurs, diffracted electrons create a collection of large-angle cones called Kossel cones that can be imaged using a phosphor screen. As these cones impinge upon the

screen, they generate visible lines referred to as Kikuchi bands [203], that are projections of the crystalline lattice geometry. These generated diffraction patterns provide information regarding the crystal structure, that can be used to identify the grain characteristics and present phases.

In *Paper II* and *Paper VI* EBSD was conducted to analyze the crystallographic texture and grain characteristics of produced specimens. This was done using a Nordlys II EBSD detector (Oxford Instruments) that was attached to a LEO Gemini 1550 HR-SEM (Carl Zeiss AG, Germany). During operation, an accelerating voltage of 20 kV was used, along with a working distance of 10 mm and a step size of 0.25 μm. The collected EBSD data was further analyzed with MTEX software and the ORTools function library [173] to help reconstruct the prior austenite grains.

5.4.6 Transmission Electron Microscopy (TEM)

Transmission electron microscopy (TEM) is a technique that creates high-resolution images by irradiating specimens with a high-voltage beam (100 to 300 kV). Although electrons in TEM are generated in a similar manner to those in SEM, TEM uses transmitted electrons that pass through the specimen, while SEM uses reflected electrons. This allows for TEM to provide valuable information regarding the specimen microstructure at the nano-scale, such as precipitate morphology, crystal structure and stress state [204]. However, for the beam to pass through the specimen it must be very thin (< 100 nm), with the required thickness depending upon the material density, material composition and desired resolution. Contrast in TEM is due to changes in the amplitude of the electron wave and is generated by variations in the specimen thickness and density, and by differences in the crystal structure and grain orientation. TEM can also be used to analyze the crystal structure, as when the electron wave passes through the specimen it generates diffraction patterns that can be used to calculate the lattice parameters [204].

In *Paper V* TEM was used for analyzing precipitates and was carried out using a FEI Tecnai T20 (Thermo Fisher Scientific, USA) equipped with a LaB_6 filament, that was operated at 200 kV.

5.4.7 Atom Probe Tomography (APT)

Atom probe tomography (APT) is a destructive technique that identifies the type and position of atoms within a specimen. This is done by exposing a thin needle-shaped specimen (< 50 nm diameter) to a high electric field at ultra-high vacuum and low temperature (30 to 70 K) [205]. As this thin specimen is subjected to a laser or voltage pulse, atoms near the tip can ionize and tear away during the field evaporation process. After these ionized atoms escape, they travel until being captured by a position sensitive detector. Said detector subsequently records the x-y position and time of flight, which can be used to identify the location of the atom as well as the type of atom by relating the time of flight to the mass-to-charge ratio. This information can then be used to create a 3D reconstruction of the analyzed specimen. The near-atomic resolution makes APT a suitable technique to study clustering, segregation and phase transformations [205] [206].

In *Paper V*, APT was used to study the distribution of atoms as well as the distribution and composition of precipitates. To perform APT, an Imago LEAP 3000X HR (Imago Scientific Instruments, USA) was operated with a 0.3 nJ laser pulsing at 30 K. The evaporation rate was set to 0.5% and the pulse frequency was set to 200 kHz. To reconstruct the APT data IVAS 3.6.14 software (CAMECA, France) was used. During data reconstruction, an evaporation field of 23 V/nm and a k-value of 4.5 were assumed. For the compositions of various regions, volumes were cut out with cylinders prior to evaluation. Additionally, the carbon content was carefully evaluated as there were plenty of molecular ions containing C, including C, C_2, C_3, C_4, C_5, and FeC_2, both single- and double-charged. Special care

was taken to deconvolute C_2^+ and C_4^{2+} at *m/n* 24 Da, taking the minor C-13 isotopes at 25 and 24.5 Da into account.

5.4.8 X-ray Diffraction (XRD)

X-ray diffraction (XRD) is a technique that can identify the crystallographic structure of a specimen. This is done by irradiating X-rays onto a specimen while simultaneously varying the angle of incidence. These diffracted X-rays are subsequently collected by detectors to measure the returned signal intensity at each incidence angle. From this measured inference, the inter-planar spacing can be determined using Bragg's law and subsequently related to databases of known diffraction patterns to identify the crystal structure of the specimen. The equation for Bragg's law is presented below, where n is the diffraction order, λ is the wavelength, d is the inter-planar spacing and θ is the incidence angle:

$$n\lambda = 2d\sin\theta \tag{6.2}$$

In *Paper II*, XRD was carried out using a Bruker AXS D8 Advance diffractometer equipped with a Cr Kα source, operated at 35 kV using a beam current of 50 mA.

5.4.9 X-ray Photoelectron Spectroscopy (XPS)

X-ray photoelectron spectroscopy (XPS) is a surface sensitive technique that can analyze the chemical state of a specimen with exceptional depth resolution (~10 nm). This is done by the irradiation of X-rays onto a specimen, which will excite electrons at the surface and induce the release of photoelectrons. These emitted photoelectrons have a specific kinetic energy that depend on the type of element, type of chemical bonding and specific electron orbital. Detectors within XPS can measure the kinetic energy of the released photoelectrons and then determine the elemental composition by calculating the characteristic binding energy. The binding energy is derived from the kinetic energy (E_k), the energy of incident X-ray photons (hv) and the work-function (W) which compensates the dissipation of energy within the photoelectron on escape from the sample to the analyzer:

$$E_B = hv - E_k - W \tag{6.3}$$

In XPS, data can be obtained using survey spectra or narrow spectra. Survey spectra detects over a large binding energy range (0 to 1416 eV) and can be used to detect all elements present on a surface. Conversely, narrow spectra will scan over a narrower binding energy range and is most commonly used for detailed analysis of individual elements.

In *Paper III*, XPS was used for measuring the surface chemistry, oxide layer thickness and conduct depth profiling. This was done using an ULVAC-PHI 5500 machine (ULVAC-PHI Inc., Japan) equipped with an Al Kα source. To determine the oxide layer thickness, Ar+ ion etching was performed at a rate of approximately 5.2 nm/min, where Ta foil with known Ta_2O_5 layers was used for calibration of the etch rate. The pass energies used for collection of survey and narrow spectra narrow were 280 eV and 26 eV, respectively. All analysis of collected XPS data was carried out using Physical Electronics' MultiPak software.

5.4.10 Materials Modelling

In this thesis two materials modelling tools were used. The first was ThermoCalc 2022a software [179] which utilizes a CALPHAD methodology and involves a phenomenological approach to calculate the thermodynamics and kinetics of multi-component material systems [207]. In *Paper I*, ThermoCalc was applied to calculate the liquidus temperature and dynamic viscosity, while in *Paper II* it was used to predict the retained austenite fraction and the martensite transformation temperatures. The calculation of the retained austenite fraction was based on an analytical equation developed by Huyan et al. [208], while the calculation of the martensite transformation temperatures was based on the modeling of the transformation barrier with fitted analytical equations [149]. All calculations with ThermoCalc were

conducted using the TCFE11 database. The second simulation tool was JMatPro with database v.11, which uses a combination of Thermodynamics modelling and physically-based models to predict and calculate the properties of multi-component material systems [181]. In *Paper I*, JMatPro was applied to calculate the surface tension, while in *Paper II* it was used to simulate the expected phases of carbon steel at composition between 0.06 to 1.1 wt.% C.

5.5 MECHANICAL TESTING

5.5.1 Hardness

Vickers micro-hardness measurements were used for determining the hardness of specimens at loads between 100 g to 10 kg. During testing, the specified load was applied by a diamond indenter, creating a square-like indentation. By measuring the average diagonal of the indentation as well as the applied force, the Vickers hardness (HV) could be calculated, where F is the force and d is the average diagonal:

$$HV = \frac{1.8544*F}{d^2} \tag{6.4}$$

Measurement of the Vickers micro-hardness in *Paper I, Paper II, Paper IV, Paper V* and *Paper VI* was conducted using a DuraScan 70-G5 machine in accordance with the ASTM E384-17 standard [209].

5.5.2 Nanoindentation

Nanoindentation is a technique used to measure the mechanical properties of small volumes of material. The technique is based on the theory of contact elasto-mechanics which states that the elastic modulus and hardness of a material can be determined from the slope of the initial unloading curve and the ratio of the peak load to contact area respectively [210], see Figure 40. This analysis of the loading-unloading curve differentiates nanoindentation from traditional micro- or macro-hardness measurements, as it allows for a determination of additional properties such as the fracture toughness, residual stress, dislocation movement and viscoelasticity [210].

In *Paper V*, nanoindentation was measured using a NanoTest Vantage 4 machine (Micro Materials, UK) at a load level of 20 mN and loading-unloading times of 20 s. From these measurements the hardness (H) was determined using the peak applied load (P_{Max}) and the projected contact area (A_c):

$$H = \frac{P_{Max}}{A_c} \tag{6.5}$$

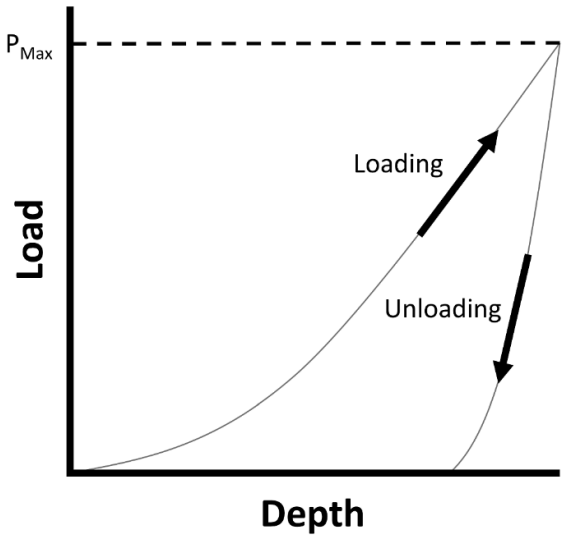

Figure 40: Schematic outlining a typical loading-unloading curve during nanoindentation.

5.5.3 Charpy Impact Testing

To study Charpy impact properties in *Paper VI* specimens were produced as 12.5 mm x 15.5 mm x 59.5 mm blocks. These blocks were then machined to Charpy v-notch specimens that were 10 mm x 10 mm x 55 mm in size following the ASTM 2298 standard [211]. Testing of the Charpy specimens was conducted at room temperature using a Zwick PSW 750 machine (Zwick Roell Group, USA).

5.5.4 Tensile Testing

To study tensile properties in *Paper VI* specimens were produced as 57 mm x 8mm rods. These rods were then machined to tensile specimens with a gauge diameter of 4 mm and a gauge length of 20 mm following the ASTM E8M standard [212]. During tensile testing a strain rate of 2.5×10^{-4} s^{-1} was maintained until 1.7% elongation to determine the Rp0.2. After this elongation was achieved, the strain rate was increased to 0.005 per second until final fracture. This was done to reduce testing time and was in accordance with the ASTM E8M standard [212]. Testing of the tensile specimens was conducted at room temperature using an Instron 4505 machine (Instron, USA).

6 RESULTS & DISCUSSION

This chapter summarizes the results and discussion of the appended papers within the context of the research questions in this thesis. These include: (RQ1) Impact of carbon content on processability and microstructure of structural steels, (RQ2) Impact of process parameters on porosity and cold cracking, and (RQ3) Impact of local thermal history on microstructure and mechanical properties.

6.1 IMPACT OF CARBON CONTENT ON PROCESSABILITY AND MICROSTRUCTURE OF STRUCTURAL STEELS

6.1.1 Processability

Results from *Paper I* show that changes in the carbon content would lead to changes in the processability of carbon steel. Starting with densification, two major effects were observed. The first was that at low VED lack of fusion porosity became less prominent at elevated carbon content (≥ 0.45 wt.%). This was clearly shown in carbon steels produced at 60 J/mm^3, as porosity within these specimens became less numerous, more rounded and smaller in size at higher carbon contents, see Figure 41. The reduction in lack of fusion porosity was due to the effect of carbon on the wetting behavior of the melt. As a higher carbon content would reduce the surface tension, viscosity and oxygen content, which subsequently improved the melt pool wettability and flowability. This enhanced the infiltration behavior of the molten metal, making it easier for lack of fusion pores to be filled in during melt track deposition. The second effect observed was that increasing the carbon content promoted the formation of keyhole porosity at lower VED. This was observed in carbon steels produced at 150 J/mm^3, as porosity within these specimens became more numerous, more rounded and larger in size at higher carbon contents, see Figure 41. The lowered onset of keyhole porosity can be somewhat attributed to the increase in melt pool depth at increased carbon content, see Figure 47, which stems from the depression of the liquidus temperature, see Figure 23. This deeper melt pool signifies an increased likelihood for unstable keyhole mode melting that can subsequently induce keyhole porosity.

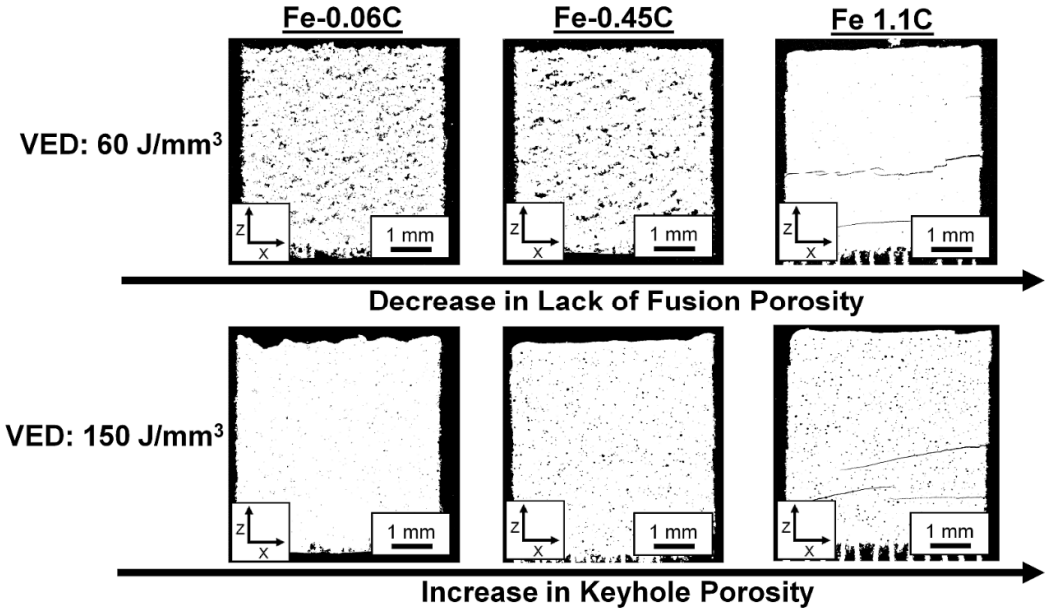

Figure 41: Results from *Paper I* outlining the influence of carbon content on lack of fusion porosity in specimens produced at 60 J/mm^3 (top), and on keyhole porosity in specimens produced at 150 J/mm^3 (bottom).

Paper III indicate that changes in the carbon content would affect the properties of the powder feedstock. Although properties such as the powder morphology and PSD remained relatively unaffected, increasing the carbon content did influence the initial oxygen content of the powder, as the amount of oxygen would decrease by up to 400 ppm as the carbon content increased. Additionally, the avalanche angle (measured using a revolution powder analyzer) would decrease by up to 2.75˚ as the carbon content increased, indicating a slight improvement in powder flow behavior.

Results from *Paper III* also found that the carbon content would affect the deoxidation behavior of carbon steels during PBF-LB. Specifically, alloys with more carbon experienced greater oxygen loss, even if the initial oxygen content of the powder was higher. This increased oxygen loss was not connected to enhanced oxygen removal by individual spatter particles. As spatter from higher carbon alloys was less likely to oxidize, had less oxygen pick-up and would form smaller oxide layers. Instead, it was due to oxygen's high affinity with carbon at elevated temperature which promoted the reduction of both elements during PBF-LB and for the reduction to become more prominent as the carbon content increased. The ability to reduce oxygen is a positive finding and indicates that carbon can be used to remove a harmful impurity element. Additionally, it shows that carbon can reduce spatter oxidation, which can subsequently alleviate oxygen pick-up during powder re-use. At the same time, the noticeable loss of carbon during PBF-LB must be accounted for to ensure that the produced part has the desired composition after processing.

In terms of cold cracking, *Paper I, Paper IV, Paper V and Paper VI* found that these defects only occurred in alloys with ≥ 0.38 wt.% C. This increased susceptibility to cold cracking was related to a higher alloy hardenability and martensite hardness as the carbon content increased, see Figure 47. Controlling the specimen hardness was one of the decisive factors that determined whether cold cracking would occur, as hardness thresholds were established in *Paper I and Paper IV* for carbon steel (< 425 HV), AISI 4140 low-alloy steel (< 460 HV) and AISI 4340 low-alloy steel (< 500 HV). Combining these findings on densification and cold cracking, *Paper I* was able to outline a process window for high-density and defect-free carbon steels as a function of the carbon content and the VED, see Figure 42.

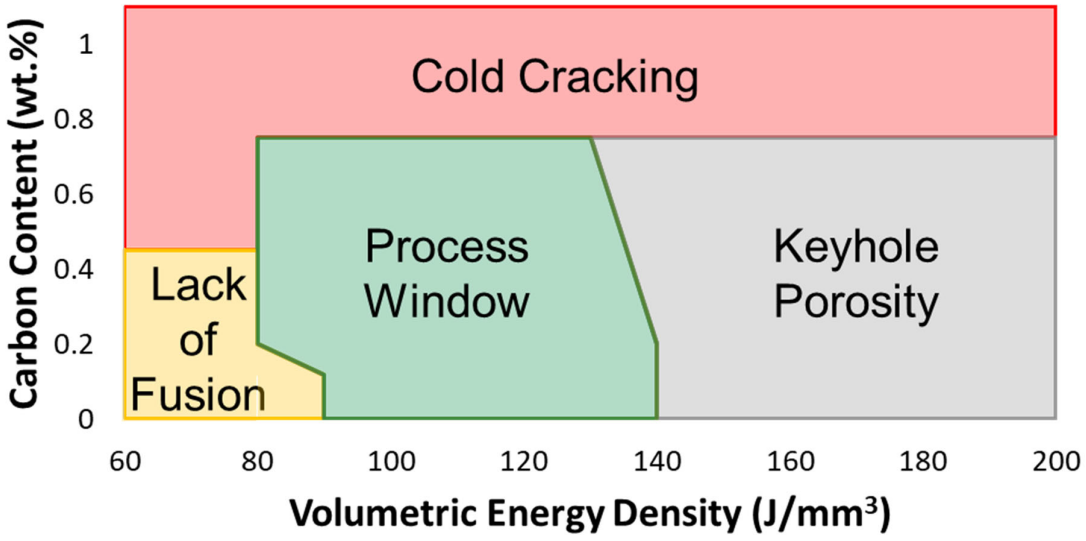

Figure 42: Results from *Paper I* outlining the process regions of carbon steel as a function of the carbon content and the VED. Specimens within the process window (green region) were crack-free and high-density (> 99.8%).

6.1.2 Microstructure

Paper II examined the impact of carbon on the microstructure of carbon steels produced by PBF-LB. It was found that these alloys were primarily composed of tempered martensite, see Figure 43, that similar hardness to traditionally quenched and tempered alloys [146]. However, in alloys with ≥ 0.75 wt.% C retained austenite was also observed, see Figure 43, due to the depression of the M_f temperature. The total retained austenite content was low for these alloys as it could not be indexed by XRD, while EBSD could only detect ~0.3% and ~1.7% retained austenite for the Fe-0.75C and Fe-1.1C alloys respectively. These values were below what was expected from thermodynamic simulations, as ~0.45% retained austenite was expected for the Fe-0.75C alloy and ~7% retained austenite was expected for the Fe-1.1C alloy. A possible explanation is that the in situ tempering of PBF-LB decomposed some of the initially retained austenite, lowering the final amount below what was expected from simulations.

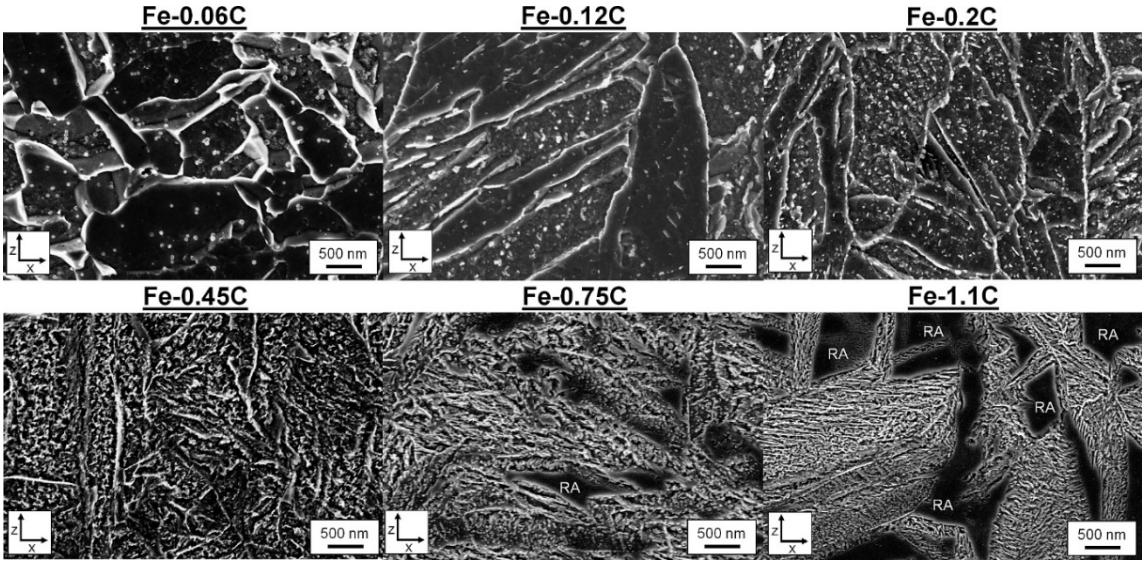

Figure 43: Results from *Paper II* outlining the microstructure of carbon steels produced by PBF-LB. These alloys were comprised primarily of tempered martensite that contained nano-sized carbides (< 100 nm). Within the Fe-0.75C and Fe-1.1C alloys, retained austenite was also observed and is marked using "RA".

Paper II also conducted a visual examination of the martensite morphology using SEM. Said analysis found that alloys with 0.06 to 0.75 wt.% C displayed a lath-like morphology, while alloys with 1.1 wt.% C displayed a plate-like morphology. This transition from lath to plate martensite at elevated carbon content was due to the depression of the M_S temperature and the increase in the retained austenite content, as both enhance the twinning slip tendency of the alloy making it more favorable for plate-like martensite to form [213]. These results were supported by thermodynamic simulations which found that the start temperature of lath-like martensite was more favorable than plate-like martensite until a composition of ~0.85 wt.% C.

6.2 IMPACT OF PROCESS PARAMETERS ON POROSITY AND COLD CRACKING

6.2.1 Porosity

Results from *Paper I, Paper III, Paper IV and Paper VI* indicated that the specimen density was dependent upon the VED and that this relationship could be segmented into three process regions, see Figure 44. At low VED there was Region I where specimens contained numerous large and irregular pores. As these pores formed at low VED and contained partially sintered particles, they were identified as lack of fusion porosity. Conversely, at high VED there was Region III where specimens contained numerous rounded and medium-sized pores. As these pores formed at high VED and were located at the bottom of melt pool boundaries, they were identified as keyhole porosity. In between these VEDs there was Region II where high-density specimens (> 99.8%) were produced that contained minimal internal porosity.

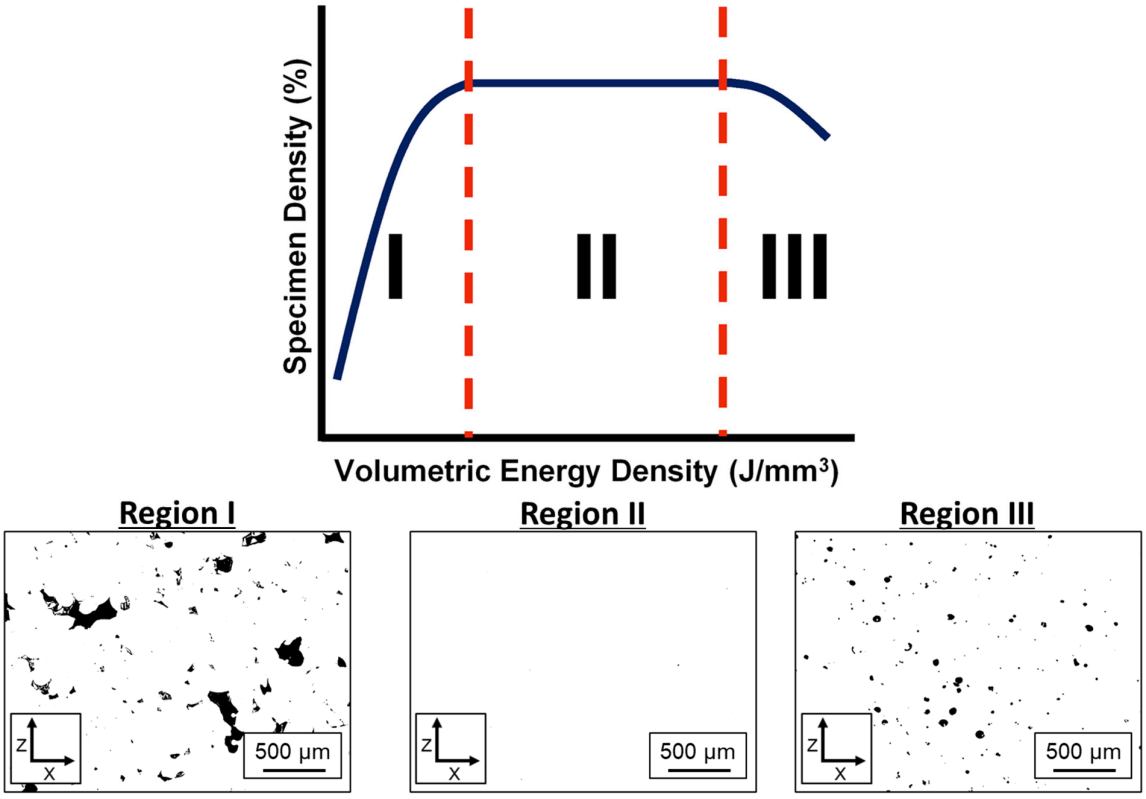

Figure 44: Schematic outlining the observed trend between specimen density and VED (top). Below are characteristic specimens from Region I, Region II and Region III specimens that were taken from Fe-0.45C steel, AISI 4340 low-alloy steel and AISI 4340 low-alloy steel respectively.

Detailed image analysis of porosity from each process regions was carried out in *Paper I and Paper IV* using quantitative metrics such as the total number of pores, the average aspect ratio of each pore, the average roundness of each pore and the cumulative porosity area as a function of the pore size, see Table 6 and Figure 45. This analysis found that porosity for Region I specimens was the most numerous, had the most irregular shape and was primarily comprised of pores sized > 50 µm, matching the visual observations of lack of fusion porosity. On the other hand, Region II specimens contained the fewest number of pores that were small (< 20 µm) and circular in shape. As for Region III specimens, they contained similarly rounded pores as Region II specimens, however porosity was more numerous and primarily related to pores sized between 20 to 100 µm. These characteristics pointed to the presence of keyhole porosity as well as an enhanced presence of small circular pores (< 20 µm) when compared to Region II specimens.

Table 6: Results from *Paper IV* showing the average pore characteristics from each process region for AISI 4140HC low-alloy steel.

	Number of Pores	Average Aspect Ratio	Average Roundness	Porosity Area Faction (%)
Region I	5000	2.0 ± 0.9	0.58 ± 0.2	4.6
Region II	1000	1.6 ± 1.2	0.72 ± 0.2	0.1
Region III	2900	1.5 ± 0.5	0.69 ± 0.2	1.4

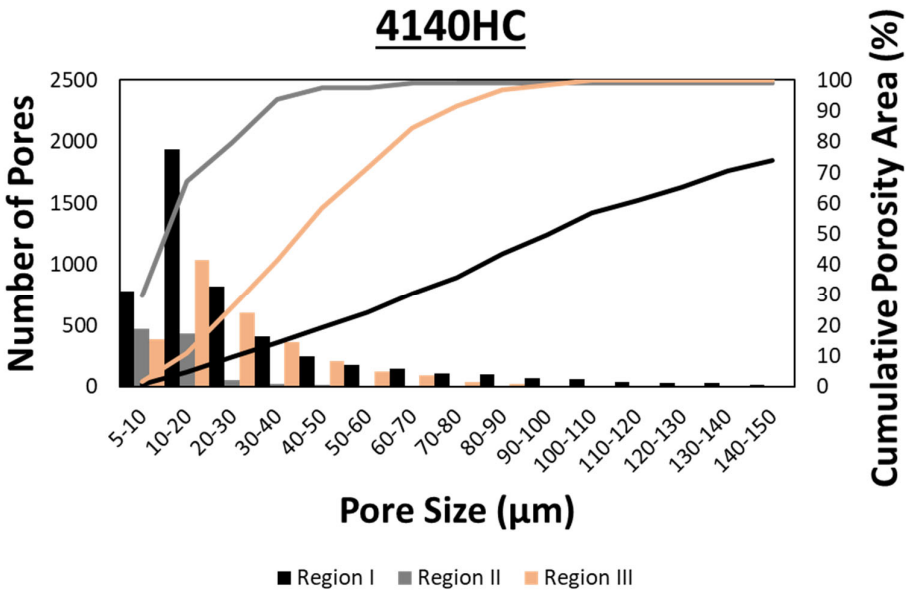

Figure 45: Results from *Paper IV* showing the histogram and cumulative area of porosity from each process region for AISI 4140HC low-alloy steel.

Despite this relationship between specimen density and VED, the VED range of each process region would shift as other laser, machine and powder parameters were altered. In terms of laser parameters, *Paper IV* observed that increasing the laser power would expand the VED range of Region II specimens. As for the beam diameter, it was found that using a smaller beam would promote the formation of keyhole porosity at lower VED when comparing the results of *Paper IV* (~40 µm beam diameter) to *Paper VI* (~100 µm beam diameter). This increased susceptibility to keyhole porosity was due to the larger laser intensity at smaller beam diameter, as the inputted energy from the laser would be applied over a much smaller region of the powder-bed. This would lead to the formation of a deeper melt pool that was more likely to reach unstable keyhole mode melting and form keyhole porosity.

In terms of machine parameters, *Paper VI* observed that increasing the build plate preheating temperature would mitigate the formation of lack of fusion porosity at low VED. This was due to an improvement in total heat input and melt pool depth as the build plate preheating temperature increased.

Lastly, in terms of powder parameters, results from *Paper III* observed that lack of fusion porosity was more likely to form at low VED for powders that had a high avalanche energy (> 7.75 mJ/kg), break energy (> 4.75 mJ/kg) and PSD (D_{10} > 25 µm). These properties accentuated the formation of lack of fusion porosity as the reduced powder flow behavior limited the ability of the powder to form a cohesive layer. While the coarser PSD meant that there were fewer fine particles to fill in the voids between coarser particles. It was possible to mitigate these issues but only after VEDs ≥ 80 J/mm^3 were applied.

6.2.2 Cold Cracking

Although results in *Paper I, Paper IV and Paper VI* indicated that cold cracking only occurred in alloys with ≥ 0.38 wt.% C, their formation also depended upon the VED. As these studies found that increasing the VED would decrease the size and number of cracks and could even stop their formation entirely if large enough VEDs were applied, see Figure 46. This reduction in cold cracking was the result of improved in situ tempering during PBF-LB. Essentially, a larger VED meant that more energy was applied to the powder-bed, leading to a formation of a larger melt pool. This larger volume of heated material reduced the rate of heat dissipation [214], which would subsequently lower the rate of heat extraction and increase the level of martensite tempering. This was shown from results in *Paper I and Paper V*, where increasing the VED led to a progressive increase in the melt pool depth and a subsequent decrease in the specimen hardness, see Figure 47. Similar results were observed for the AISI 4130, 4140, 4340 and 8620 low-alloy steels examined in *Paper IV and Paper VI*. These results are encouraging as they show that it possible to produce structural steels crack-free at high carbon content (< 0.75 wt.% C) without build plate preheating, as long as a sufficiently large VEDs are applied. Still, results from *Paper I* do indicate that only adjusting the VED cannot avoid cold cracking in carbon steels with ≥ 0.75 wt.% C and highlights that additional crack mitigation techniques are required.

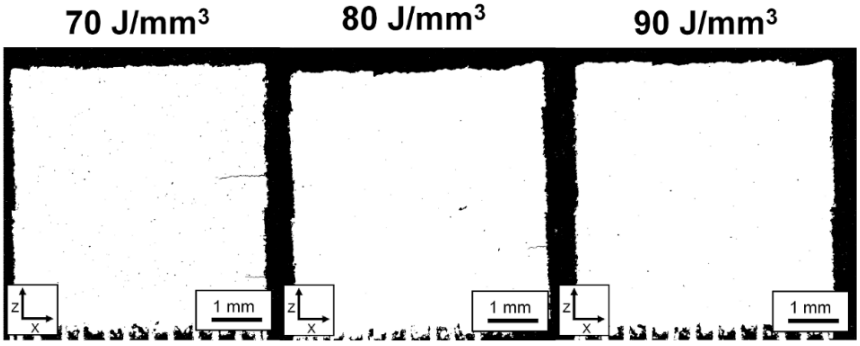

Figure 46: Results from *Paper I* showcasing the decrease in crack susceptibility with increasing VED for an Fe-0.45C alloy.

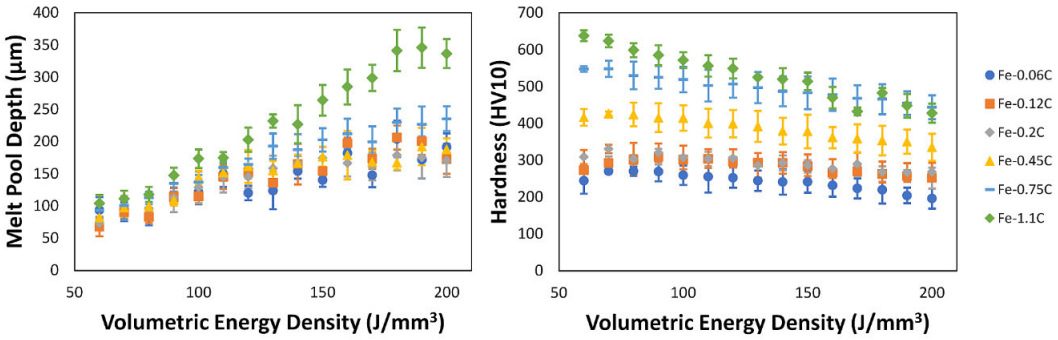

Figure 47: Results from *Paper I* outlining the change in melt pool depth and specimen hardness as a function of the VED for carbon steels between 0.06 to 1.1 wt.% C.

Besides the VED, the propensity for cold cracking also shifted as other laser and machine parameters were altered. In terms of the laser power, results from *Paper IV* found that increasing the laser power would decrease the required VED to avoid cold cracking. This was due to the increase in melt pool depth as the laser power increased, which would subsequently enhance the degree of in situ tempering, lowering the specimen hardness and making the material less susceptible to cold cracking.

In terms of the beam diameter, *Paper IV and Paper VI* both examined PBF-LB of AISI 4140 and 4340 low-alloy steel. However, each paper observed a different cold cracking response, as cracking could be avoided at lower VED in *Paper IV* (4140: 80 J/mm^3 and 4340: 80 J/mm^3) than in *Paper VI* (4140: 200 J/mm^3 and 4340: 180 J/mm^3). This was due to the smaller beam diameter used in *Paper IV* (~40 µm versus ~100 µm), which led a larger laser intensity and the formation of deeper melt pools. This subsequently enhanced the level of in situ tempering and lowered the hardness of produced specimens. Still, the hardness required to avoid cold cracking was larger for specimens in *Paper IV* (4140: 440 HV and 4340: 500 HV) than for specimens in *Paper VI* (4140: 410 HV and 4340: 450 HV). This suggests that increasing the laser intensity might alleviate other factors related to cold cracking, but this requires further investigation.

Lastly, in terms of machine parameters the impact of build plate preheating was examined in *Paper VI*. Results indicate that increasing the build plate preheating temperature would lower the required VED to produce crack-free specimens. In fact, when using the highest build plate preheating temperature of 180°C, cold cracking was avoided in all specimens regardless of the VED. This improved cracking resistance was partially due to a reduction in martensite hardness as the build plate preheating temperature increased. Additionally, past works have shown that increasing the build plate preheating temperature will reduce the magnitude of residual stress, see Sections 2.4.4 and 2.4.5, further lowering the crack susceptibility of the specimens. From these findings, *Paper VI* was able to establish processing windows for the AISI 4140, 4340 and 8620 low-alloy steel as a function of the build plate preheating temperature and the VED, see Figure 48.

Combined, these results indicate that the formation of cold cracking in structural steels is dependent not only on the carbon content but also on the degree of in situ tempering, which is controlled by the process parameters. This highlights that when trying to produce crack-free specimens the process parameters must be tailored to the carbon content of the alloy to ensure adequate in situ tempering.

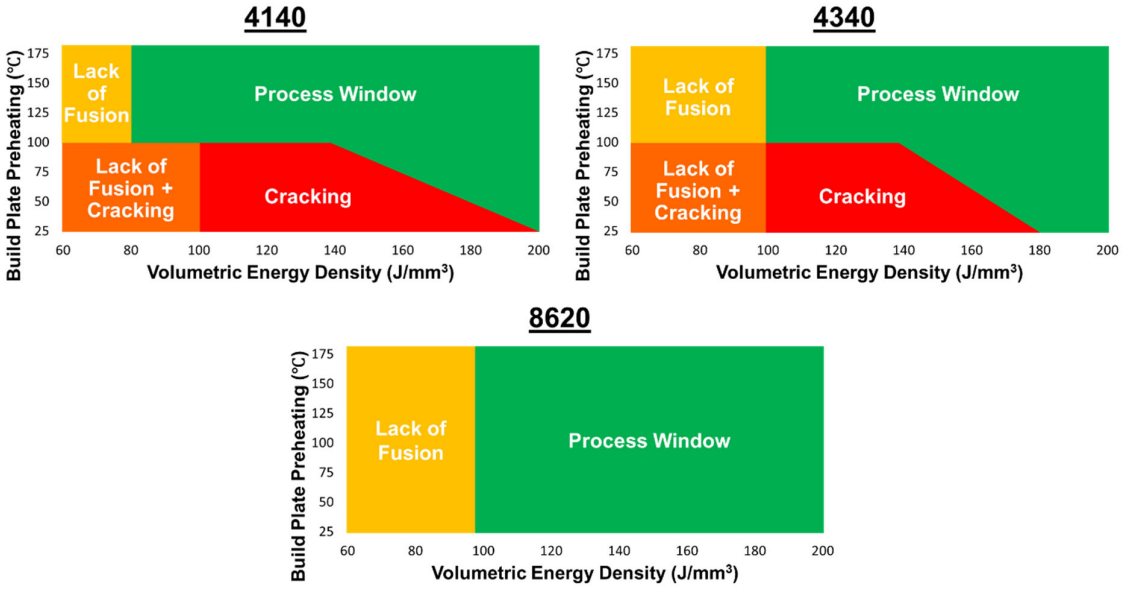

Figure 48: Results from *Paper VI* outlining the process regions of AISI 4140, 4340 and 8620 low-alloy steel as a function of the build plate preheating temperature and the VED. Specimens within the process window (green region) were crack-free and high-density (> 99.8%).

6.3 IMPACT OF LOCAL THERMAL HISTORY ON MICROSTRUCTURE AND MECHANICAL PROPERTIES

6.3.1 Microstructure

Paper V examined the impact of the local thermal history on the in situ tempering of martensite during PBF-LB of Fe-0.45C steel. As was mentioned in Section 2.3.3, martensite initially forms during layer melting, when the melted powder layer and previously solidified material is heated above the austenite stability temperature before rapid cooling. Characterization of this initial martensite was possible by examining the specimen top layer, as this region was not reheated during PBF-LB and could maintain its as-deposited state. Analysis of this region revealed that martensite was initially in a quenched-like state as it had a high hardness (750-800 HV) and contained no carbides, see Figure 49. However, carbon atoms within this region did not remain in solid solution and had instead segregated to dislocations and martensite lath boundaries, see Figure 49. This segregation was due to the reduced solubility of carbon atoms at the octahedral sites of the BCT martensite lattice, as well as the high mobility of carbon atoms when held at room temperature.

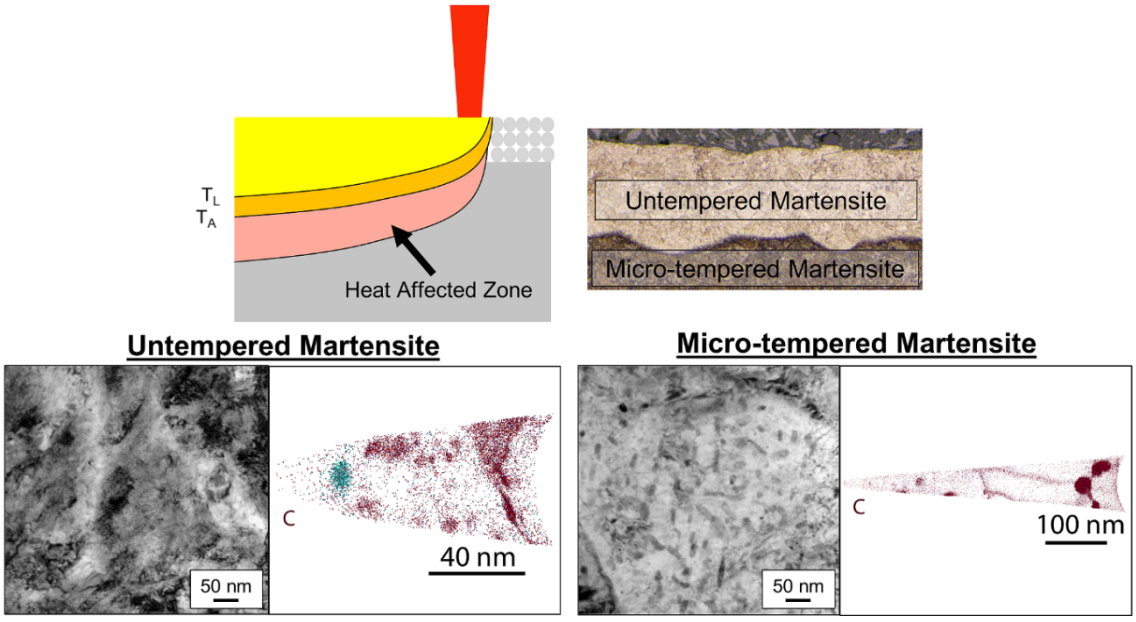

Figure 49: Schematic from *Paper V* highlighting where micro-tempering occurs during layer melting and where untempered or micro-tempered martensite is found in Fe-0.45C steel specimens. Higher magnification TEM and APT images of untempered and micro-tempered martensite for Fe-0.45C steel are shown below.

Subsequent tempering of martensite was due to micro-tempering within the heat affected zone and macro-tempering due to heat conduction and subsequent heat accumulation, see Figure 13. Extensive hardness measurements found that although both influenced martensite hardness, micro-tempering had the most significant impact. As the difference in hardness between untempered and micro-tempered martensite reached up to ~380 HV, see Figure 51. While the difference in hardness within the specimen due to macro-tempering reached up to only ~67 HV. Additionally, it was shown that regions of the specimen that did not experience micro-tempering (e.g., areas below lack of fusion porosity) would remain in an untempered state.

The noticeable reduction in martensite hardness during micro-tempering was due to the change in carbon atom distribution, as carbon went from being segregated at boundaries and dislocations to forming a distributed network of nano-sized carbides, see Figure 49. These carbides formed at the previously carbon enriched regions of martensite, indicating that the initial segregation of carbon acted as a precursor to carbide formation. Further APT revealed that these carbides had a carbon content of ~24.6 at.% C, matching the expected composition of cementite. Additional proxigrams observed a depletion of Si within the carbides as well as a build-up of Si at the carbide-matrix interface, see Figure 50, further supporting the claim that the carbides related to cementite.

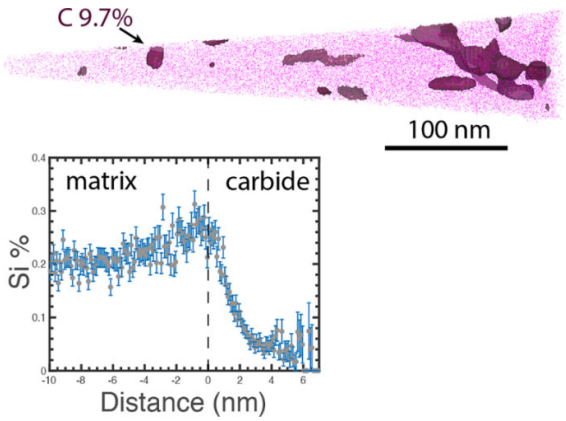

Figure 50: Proxigram from *Paper V* indicating the Si distribution of the highlighted carbide. The pink dots show the outline of the atom probe reconstruction.

Lastly, the degree of micro-tempering was dependent upon the VED, as increasing the energy input from 60 to 190 J/mm^3 decreased the martensite hardness within the micro-tempered regions by ~100 HV, see Figure 51. This was due to the noticeable increase in top layer depth, which increased from 87 ± 11 to 158 ± 15 to 263 ± 16 µm as the VED increased from 60 to 100 to 190 J/mm^3. This noticeable reduction in hardness indicates that despite its rapid nature, micro-tempering within the heat affected zone will lead to significant martensite tempering that can be tailored even on the micron scale.

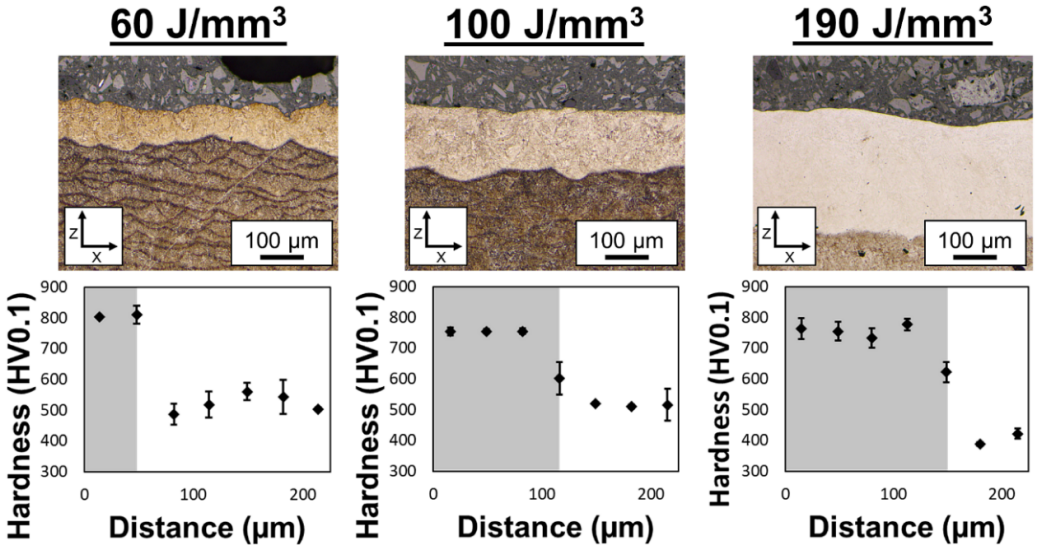

Figure 51: Results from *Paper V* showcasing the top layer in Fe-0.45C specimens produced at 60, 100 and 190 J/mm^3. Micro-hardness measurements (HV0.1) along the z-direction are also included, where indentations taken within the top layer are indicated by the grey region.

6.3.2 Mechanical Properties

Paper VI examined the impact of the local thermal history on the mechanical properties of AISI 4140, 4340 and 8620 low-alloy steel. This was done by producing specimens that were crack-free and high-density (> 99.8%) to ensure that a material response was measured for the alloys rather than a defect response. Mechanical testing shows that the examined low-alloy steels exhibited a combination of high strength, area reduction and impact toughness that exceeded the ASTM standards, while also achieving solid levels of elongation that fell within the ASTM standards, see Figure 52. This combination of properties was due to the produced microstructure which consisted of tempered martensite, as well as numerous nano-sized carbides. This finely tempered microstructure, which formed during the local thermal history, allowed the alloys to maintain the high strength and hardness of martensite without noticeably reducing ductility or toughness.

Another finding from mechanical testing was the limited presence of anisotropy when comparing horizontally and vertically produced specimens. As the reduction in tensile properties from horizontal to vertical specimens was below 10%, while the reduction in Charpy impact toughness only reached between 8 to 17%, see Figure 52. This reduced anisotropy was first due to the unique grain structure of the alloys, as instead of forming large columnar grains that were oriented along the building direction, the low-alloy steels formed a combination of fine martensite laths and small columnar/equiaxed grains related to prior austenite. Another cause for the reduced anisotropy was the rather homogeneous microstructure that stemmed from macro-tempering due to build plate preheating and post-AM stress relief. This homogeneity was observed from hardness measurements, as the deviation in hardness within a single specimen reached up to only 6 to 8%. Lastly, the limited presence of internal defects also contributed to the reduced levels of anisotropy, as defects preferentially oriented to the loading direction will negatively impact mechanical properties. These findings indicate that when processed defect-free and high-density, structural steels are not only suitable but actively take advantage of PBF-LB to achieve mechanical properties that meet or exceed those of conventionally produced alloys.

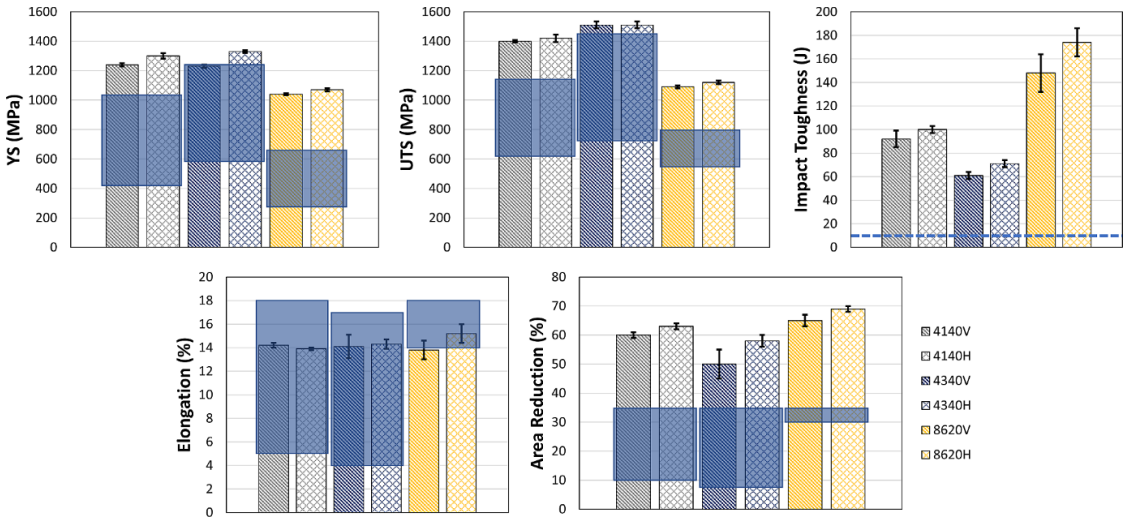

Figure 52: Results from *Paper VI* outlining the mechanical properties of AISI 4140, 4340 and 8620 low-alloy steel produced by PBF-LB. The ASTM standards are outlined as boxed regions or as dashed lines [215] [216].

7 CONCLUSIONS

RQ1: Impact of carbon content on processability and microstructure of structural steels?

Processability

- Elevated carbon content (≥ 0.45 wt.% C) reduced the formation of lack of fusion porosity at low VED, while promoting the onset of keyhole porosity at lower VED.
- Cold cracking occurred in alloys with ≥ 0.38 wt.% C and could be related to specific hardness thresholds when no build plate preheating was applied:
  - Carbon steel below 425 HV;
  - AISI 4140 low-alloy steel below 460 HV;
  - AISI 4340 low-alloy steel below 500 HV;
- Increasing the carbon content did not noticeably impact the properties of the powder feedstock, besides decreasing the initial oxygen content and reducing the avalanche angle by up to 2.75˚;
- Increasing the carbon content increased the oxygen loss during PBF-LB.

Microstructure

- Carbon steels were primarily composed of tempered martensite. However, alloys with ≥ 0.75 wt.% C also contained some retained austenite;
- Alloys with 0.06 to 0.75 wt.% C displayed a lath-like martensite morphology, while alloys with 1.1 wt.% C displayed a plate-like martensite morphology.

RQ2: Impact of process parameters on porosity and cold cracking?

Porosity

- At low VED, specimens formed lack of fusion porosity, while at high VED they formed keyhole porosity. In between these VED ranges, high density specimens (> 99.8%) were produced;
- Increasing the laser power expanded the VED range of high density specimens;
- Decreasing the beam diameter lowered the required VED to form keyhole porosity;
- Increasing the build plate preheating temperature reduced lack of fusion porosity at low VED;
- Powders with high avalanche energy (> 7.75 mJ/kg), break energy (> 4.75 mJ/kg) and PSD (D10 > 25 μm) were more likely to form lack of fusion porosity at low VED.

Cold Cracking

- Increasing the VED reduced the size and propensity of cold cracking due to improved in situ tempering of martensite during PBF-LB;
- Decreasing the laser beam diameter, increasing the laser power and increasing the build plate preheating temperature reduced the required VED to avoid cold cracking;
- It was possible to produce carbon steels with carbon content below 0.75 wt.% crack-free without build plate preheating as long as a sufficiently large VEDs were applied.

RQ3: Impact of local thermal history on microstructure and mechanical properties?

Microstructure

- Martensite is initially in a quenched state during PBF-LB with carbon atoms segregating to dislocations and martensite lath boundaries;
- Hardness measurements indicate that micro-tempering had the most significant effect on martensite tempering during PBF-LB as it decreased hardness by up to ~380 HV, while macro-tempering only decreased hardness by up to ~67 HV;
- The reduction in hardness during micro-tempering was due to the precipitation of nano-sized carbides at the previously carbon enriched regions of martensite. These carbides were identified as cementite, due to their composition and the rejection of Si at the carbide/matrix interface;
- The degree of this micro-tempering was dependent upon VED, as increasing from 60 to 190 J/mm^3 decreased the martensite hardness within the micro-tempered regions by ~100 HV.

Mechanical Properties

- Low-alloy steel produced by PBF-LB achieved a high ultimate tensile strength (AISI 4140: ~1400 MPa, AISI 4340: ~1500 MPa, AISI 8620: ~1100 MPa), impact toughness (AISI 4140: ~90-100 J, AISI 4340: ~60-70 J, AISI 8620: ~150-175 J), and elongation (AISI 4140: ~14%, AISI 4340: ~14%, AISI 8620: ~14-15%) that met or exceeded the ASTM standards.
- Mechanical testing also revealed limited directional anisotropy that was attributed to:
    - The prevalence of small grains within limited crystallographic texture;
    - A homogenous microstructure due to build plate preheating and post-AM stress relief;
    - The reduced presence of internal defects.
- These results indicate that when produced high density and defect-free, structural steels are not only suitable but actively takes advantage of PBF-LB to achieve mechanical properties that meet or exceed those of conventionally produced alloys.

8 FUTURE WORK

Based on the findings of this thesis the following topics are recommended for future research:

- *Paper I, Paper IV and Paper VI* proved that structural steels can be robustly produced by PBF-LB. However, to accelerate the industrial implementation of these alloys, production costs must be lowered as this is one of the driving factors for structural components. Therefore, there is a strong need to further develop the PBF-LB process to achieve high-productivity while maintaining part quality.
- *Paper III* showed the importance of carbon and oxygen control during PBF-LB of structural steel. Hence, there is a need for further studies to understand the impact of process parameters on carbon control and the potential batch-to-batch variation during powder re-use.
- *Paper I, Paper IV, Paper V and Paper VI* indicated that increasing the VED and build plate preheating temperature could mitigate cold cracking. However, the specific effect of each on the conditions required for cold cracking (e.g., residual stress and fracture resistance) has yet to be clearly defined. Therefore, further studies should examine the variation in residual stress and fracture resistance as a function of these parameters.
- *Paper I and Paper IV* were able to identify the presence of cold cracking. However, the formation of other types of cracking remains poorly defined for structural steel. On-going work has examined the formation of micro-cracks in AISI 4140 low-alloy steel produced by PBF-LB. Early results indicate that they are connected to trace elements that segregate during solidification and subsequently induce cracking at high angle grain boundaries. Further work is needed to clarify the crack sensitivity to the different types of trace elements and how this micro-cracking influences mechanical properties.
- *Paper V* examined the in situ tempering of martensite during PBF-LB of Fe-0.45C steel using post-mortem analysis. To further this understanding, it would be beneficial to observe this phenomena using operando measurements that could characterize the solidification path, define the local temperature history and follow carbide precipitation in real time. This kind of investigation is currently underway using synchrotron X-ray diffraction at the Paul Scherrer Institute in Villingen, Switzerland.
- *Paper VI* indicated the presence of many fine carbides. However, the work was unable to structurally characterize them due to their small size and distribution. Determining their composition could improve the understanding of the initial microstructure and explain their impact on mechanical strength. Additionally, tailored heat treatments should be developed for these alloys that focus on forming or coarsening the desired carbides to further optimize the mechanical properties.
- *Paper VI* showed that the static mechanical properties of structural steels produced by PBF-LB can meet or exceed the properties of conventionally produced alloys. Further work is required to understand the dynamic mechanical properties of these alloys during PBF-LB and how they compare to conventionally produced material.

9 ACKNOWLEDGEMENTS

First, I would like to thank my supervisor Eduard Hryha for his generous support, patience and guidance during my PhD. I would also like to thank my co-supervisor Lars Nyborg for his assistance and feedback. I am grateful to both of you for letting me take part in such exciting research.

I would like to recognize the Centre for Additive Manufacturing – Metal (CAM^2), supported by the Swedish Governmental Agency of Innovation Systems (Vinnova), for providing the framework and funding of this PhD work.

I am grateful to all of my co-authors and colleagues for their fantastic work and collaboration. Special thanks go out to Peter Harlin from Sandvik Additive Manufacturing and Sven Bengtsson from Höganäs AB for their noticeable feedback and guidance throughout my PhD.

I would like to thank and recognize my former masters' students, Robert and Rasmus for their fantastic work, interesting discussions and camaraderie.

I would like to acknowledge Dr. Yiming Yao, Dr. Eric Tam, Roger Sagdahl and Håkan Millqvist for their availability and support during my research. Furthermore, I would like to acknowledge Jessica Twedmark, Palina Wendel and Lillvor Wahlberg for their administrative support.

I would like to thank my current and past colleagues at the Department of Industrial and Materials Science. Special thanks go out to my AM/PM colleagues, my officemates Casey and Erika, and my fika mates Camille, Antonio, Phillip and Dmitri whose presence always made my day more enjoyable and were always there to provide support when it was needed.

Special thanks go out to my family and friends for their support, whether it is those back in Canada or those in Sweden and Finland.

To my lovely wife Ida, I want to thank you for your unwavering support during my difficult times, and for your endless love and patience, without which I would not have made it to the present day.

Lastly, I want to thank my amazing son Ville for showing me what truly matters in life.

10 REFERENCES

[1] "Standard Terminology for Additive Manufacturing - General Principles - Terminology," ASTM International, West Conshohocken, PA, 2015.

[2] Grand View Research, "Additive Manufacturing Market Size, Share & Trends Analysis Report By Component, By Printer Type, By Technology, By Software, By Application, By Vertical, By Material, By Region, And Segment Forecasts, 2022 - 2030," 2021. [Online]. Available: https://www.grandviewresearch.com/industry-analysis/additive-manufacturing-market/toc. [Accessed 25 October 2022].

[3] Knowledge Sourcing Intelligence, "Powder Bed Fusion 3D Printing Technology Market Size, Share, Opportunities, COVID-19 Impact, And Trends By Component (Hardware, Software, Services, Material), By Technology (Multi Jet Fusion, Selective Laser Sintering, Direct Metal Laser Sintering/Selecti," July 2021. [Online]. Available: https://www.knowledge-sourcing.com/report/powder-bed-fusion-process-3d-printer-market. [Accessed 25 October 2022].

[4] AMPOWER GmbH & Co. KG, "AMPower Report 2020," 2020.

[5] Introduction to Additive Manufacturing Technology: 3rd Edition, European Powder Metallurgy Association, 2019.

[6] D. Bourell, W. Frazier, H. Kuhn and M. Seifi, ASM Handbook®, Volume 24 - Additive Manufacturing Processes, ASM International, 2020.

[7] P. Bajaj, A. Hariharan, A. Kini, P. Kurnsteiner, D. Raabe and E. Jägle, "Steels in additive manufacturing: A review of their microstructure and properties," *Materials Science & Engineering A,* vol. 772, 2020.

[8] H. Fayazfar, M. Salarian, A. Rogalsky, D. Sarker, P. Russo, V. Paserin and E. Toyserkani, "A critical review of powder-based additive manufacturing of ferrous alloys: Process parameters, microstructure and mechanical properties," *Materials and Design,* vol. 144, pp. 98-128, 2018.

[9] S. Narasimharaju, W. Zeng, T. See, Z. Zhu, P. Scott, X. Jiang and S. Lou, "A comprehensive review on laser powder bed fusion of steels: Processing, microstructure, defects and control methods, mechanical properties, current challenges and future trends," *Journal of Manufacturing Processes,* vol. 75, pp. 375-414, 2022.

[10] D. Böckin and A.-M. Tillman, "Environmental asessment of additive manufacturing in the automotive industry," *Journal of Cleaner Production,* vol. 226, pp. 977-987, 2019.

[11] A. M, G. Issayev, E. Shehad and S. Sarfraz, "A critical review of 3D printing and digital manufacturing in construction engineering," *Rapid Prototyping Journal,* vol. 28, no. 7, pp. 1312-1324, 2022.

[12] J. Dossett and G. Totten, ASM Handbook, Volume 04D - Heat Treating of Irons and Steels., ASM International, 2014.

[13] A. I. H. Committee, ASM Handbook, Volume 01 - Properties and Selection: Irons, Steels, and High-Performance Alloys., ASM International, 1990.

[14] S. Aparna, "Global Automotive Spare Parts Logistics Market 2022 Size By Parts, Logistics, By Application with Global Demand and Analysis Forecast by 2022-2028," 21 October 2022. [Online]. Available: Global Automotive Spare Parts Logistics Market 2022 Size By Parts, Logistics, By Application with Global Demand and Analysis Forecast by 2022-2028. [Accessed 25 October 2022].

[15] L. Malefane, W. du Preez, M. Maringa and A. du Plessis, "Tensile and high cycle fatigue properties of annealed Ti6Al4V (ELI) specimens produced by direct metal laser sintering," *South African Journal of Industrial Engineering,* vol. 29, pp. 299-311, 2018.

[16] O. Andreau, E. Pessard, I. Koutiri, J.-D. Penot, C. Dupuy, N. Saintier and P. Peyre, "A competition between the contour and hatching zones on the high cycle fatigue behaviour of a

316L stainless steel: Analyzed using X-ray computed tomography," *Materials Science and Engineering A,* vol. 757, pp. 146-159, 2019.

[17] H. Carlton, A. Haboub, G. Gallegos, D. Parkinson and A. MacDowell, "Damage evolution and failure mechanisms in additively manufactured stainless steel," *Materials Science & Engineering A,* vol. 651, pp. 406-414, 2016.

[18] N. Larrosa, W. Wang, N. Read, M. Loretto, C. Evans, J. Carr, U. Tradowsky, M. Attallah and P. Withers, "Linking microstructure and processing defects to mechanical properties of selectively laser melted AlSi10Mg alloy," *Theoretical and Applied Fracture Mechanics,* vol. 98, pp. 123-133, 2018.

[19] E. Jelis, M. Clemente, M. Hespos, S. Groeschler, E. Golden and R. Carpenter, "Round Robin Study Evaluating Consistency of 4340 Steel," *Journal of Materials Engineering and Performance,* vol. 30, pp. 6832-6843, 2021.

[20] E. Jelis, M. Hespos and N. Ravindra, "Process Evaluation of AISI 4340 Steel Manufactured by Laser Powder Bed Fusion," *Journal of Materials Engineering and Performance,* vol. 27, pp. 63-71, 2018.

[21] A. Strondl, O. Lyckfeldt, H. Brodin and U. Ackelid, "Characterization and Control of Powder Properties for Additive Manufacturing," *JOM,* no. 67, pp. 549-555, 2015.

[22] J. Benson and E. Snyders, "The need for powder charcterization in the additive manufacturing industry and the establishment of a national facility," *The South African Journal of Industrial Engineering,* no. 26, pp. 104-114, 2015.

[23] D. Riabov, L. Cordova, E. Hryha and S. Bengtsson, "Effect of powder variability on laser powder bed fusion processing and properties of 316L," *European Journal of Materials,* vol. 2, no. 1, pp. 202-221, 2022.

[24] S. Vock, B. Klöden, A. Kirchner, T. Weissgärber and B. Kieback, "Powders for powder bed fusion: a review," *Progress in Additive Manufacturing,* no. 4, pp. 383-397, 2019.

[25] L. Haferkamp, L. Haudenschild, A. Spierings, K. Wegener, K. Riener, S. Ziegelmeier and G. Leichtfried, "The Influence of Particle Shape, Powder Flowability, and Powder Layer Density on Part Density in Laser Powder Bed Fusion," *Metals,* vol. 11, no. 418, 2021.

[26] D. Schulze, Powder and bulk solids: behavior, characterization, storage and flow, Berlin: Springer, 2008.

[27] P. Karapatis, "A sub-process approach of selective laser sintering," EPFL, Lausanne, 2002.

[28] D. Riabov, E. Hryha, M. Rashidi, S. Bengstsson and L. Nyborg, "Effect of atomization on surface oxide composition in 316L stainless steel powders for additive manufacturing," *Surface and Interface Analysis,* vol. 52, no. 11, pp. 694-706, 2020.

[29] H. Gruber, C. Luchian, E. Hryha and L. Nyborg, "Effect of Powder Recycling on Defect Formation in Electron Beam Melted Alloy 718," *Metallurgical and Materials Transactions A,* vol. 51, no. 5, pp. 2430-2433, 2020.

[30] M. Tang and P. Pistorius, "Oxides, porosity and fatigue performance of AlSi10Mg parts produced by selective laser melting," *International Journal of Fatigue,* vol. 94, pp. 192-201, 2017.

[31] M. Ansari, A. Mohamadizadeh, Y. Huang and V. Paserin, "Laser directed deposition of water-atomized iron powder: process optimization and microstructure of single-tracks," *Optics & Laser Technology,* vol. 112, pp. 485-493, 2019.

[32] E. Jelis, M. Clemente, S. Kerwien, N. Ravindra and R. Hespos, "Metallurgical and Mechanical Evaluation of 4340 Steel Produced by Direct Metal Laser Sintering," *JOM,* vol. 67, no. 3, pp. 582-589, 2015.

[33] J. Weinberg, Design and Implementation of an Experimental and Numerical Framework for Powder Recoating Research in Selective Laser Melting, Massachusetts Institute of Technology, 2018.

[34] M. Tang, P. Pistorius and J. Beuth, "Prediction of lack-of-fusion porosity for powder bed fusion," *Additive Manufacturing,* vol. 14, pp. 39-48, 2017.

[35] C. Qui, C. Panwisawas, M. Ward, H. Basoalto, J. Brooks and M. Attallah, "On the role of melt flow into the surface structure and porosity development during selective laser melting," *Acta Materialia,* no. 96, pp. 72-79, 2015.

[36] R. Mertens, B. Vrancken, N. Holmstock, Y. Kinds, J.-P. Kruth and J. Van Humbeeck, "Influence of powder bed preheating on microstructure and mechanical properties of H13 tool steel SLM parts," *Physics Procedia,* no. 83, pp. 882-890, 2016.

[37] H. Ali, H. Ghadbeigi and K. Mumtaz, "Effect of scanning strategies on residual stress and mechanical properties of Selective Laser Melted Ti6Al4V," *Materials Science & Engineering A,* no. 712, pp. 175-187, 2018.

[38] T. DebRoy, H. Wei, J. Zuback, T. Mukherjee, J. Elmer, J. Milewski, A. Beese, A. Wilson-Heid, A. De and W. Zhang, "Additive manufacturing of metallic components - Process, structure and properties," *Progress in Materials Science,* vol. 92, pp. 112-224, 2018.

[39] C. Pauzon, S. Van Petegem, E. Hryha, C. Change, S. Hocine, H. Van Swygenhoven, C. de Formanoir and S. Dubiez-Le Goff, "Effect of helium as process gas on laser powder bed fusion of Ti-6Al-4V studied with operando diffraction and radiography," *European Journal of Materials,* vol. 2, no. 1, pp. 422-435, 2022.

[40] C. Pauzon, A. Leicht, U. Klement, P. Foret and E. Hryha, "Effect if the Process Gas and Scan Speed on the Properties and Productivity of Thin 316L Structures Produced by Laser-Powder Bed Fusion," *Metallurgical and Materials Transactions A,* no. 51, pp. 5339-5350, 2020.

[41] C. Schwerz, A. Raza, X. Lei, L. Nyborg, E. Hryha and H. Wirdelius, "In-situ detection of redeposited spatter and its influence on the formation of internal flaws in laser powder bed fusion," *Additive Manufacturing,* vol. 47, p. 102370, 2021.

[42] W. Meiners, K. Wissenbach and A. Gasser, "Shaped Body Especially Prototype or Replacement Part Production". DE Patent DE19649865C1, 1996.

[43] H. Lee, C. Lim, M. Low, N. M. V. Tham and Y.-J. Kim, "Lasers in Additive Manufacturing: A Review," *International Journal of Precision Engineering and Manufacturing-Green Technology,* no. 4, pp. 307-322, 2017.

[44] A. Gusarov, S. Grigoriev, M. Volosova, Y. Melnik, A. Laskin, D. Kotoban and A. Okunkova, "On productivity of laser additive manufacturing," *Journal of Materials Processing Technology,* vol. 261, pp. 213-232, 2018.

[45] C. Guo, Y. Zhou, X. Li, X. Hu, Z. Xu, E. Dong, Q. Zhu and R. Ward, "A comparing study of defect generation in IN738LC superalloy fabricated by laser powder bed fusion: Continuos-wave mode versus pulsed-wave mode," *Journal of Materials Science & Technology,* vol. 90, pp. 45-57, 2021.

[46] K. Georgilas, R. Khan and M. Kartal, "The influence of pulsed laser powder bed fusion process parameters on Inconel 718 material properties," *Materials Science & Engineering A,* vol. 769, p. 138527, 2020.

[47] Y. Li and D. Gu, "Parametric analysis of thermal behavior during selective laser melting additive manufacturing of aluminum alloy powder," *Materials and Design,* no. 63, pp. 856-867, 2014.

[48] W. Di, Y. Yongqiang, S. Xubin and C. Yonghua, "Study on energy input and its influences on single-track, multi-track, and multi-layer SLM," *The International Journal of Advanced Manufacturing Technology,* vol. 58, pp. 1189-1199, 2012.

[49] R. Cunningham, C. Zhao, N. Parah, C. Kantzos, J. Pauza, K. Fezzaa, T. Sun and A. Rollett, "Keyhole threshold and morpohology in laser melting revealed by ultrahigh-speed x-ray imaging," *Science,* vol. 363, pp. 849-852, 2019.

[50] Z. Francis, "The Effects of Laser and Electron Beam Spot Size in Additive Manufacturing Processes," Carnegie Mellon University, Pittsburgh, 2017.

[51] J. Metelkova, Y. Kinds, K. Kempen, C. de Formanoir, A. Witvrouw and B. Van Hooreweder, "On the influence of laser defocusing in Selective Laser Melting of 316L," *Additive Manufacturing,* no. 23, pp. 161-169, 2018.

[52] V. Matilainen, H. Piili, A. Salminen and O. Nyrhila, "Preliminary investigation of keyhole phenomena during single layer fabrication in laser additive manufacturing of stainless steel," *Physics Procedia,* vol. 78, pp. 377-387, 2015.

[53] M. Rombouts, J. Kruth, L. Froyen and P. Mercelis, "Fundamentals of Seletive Laser Melting of alloyed steel powders," *CIRP Annals,* vol. 55, no. 1, pp. 187-192, 2006.

[54] X. Li, Y. Tan, H. Willly, P. Wang, W. Lu, M. Cagirici, C. Ong, T. Herng, J. Wei and J. Ding, "Heterogenously tempered martensitic high strength steel by selective laser melting and its micro-lattice: Processing, microstructure, superior performance and mechanisms," *Materials and Design,* vol. 178, 2019.

[55] T. Mukherjee and T. DebRoy, "Mitigation of lack of fusion defects in powder bed fusion additive manufacturing," *Journal of Manufacturing Processes,* vol. 36, pp. 442-449, 2018.

[56] J. Kruth, L. Froyen, J. Van Varenbergh, P. Mercelis, M. Rombouts and B. Lauwers, "Selective laser melting of iron-based powder," *Journal of Materials Processing Technology,* vol. 149, pp. 616-622, 2004.

[57] S.-H. Sun, K. Hagihara and T. Nakano, "Effect of scanning strategy on texture formation in Ni-25 at.%Mo alloys fabricated by selective laser melting," *Materials and Design,* vol. 140, pp. 307-316, 2018.

[58] X. Zhou, K. Li, D. Zhang, X. Liu, J. Ma, W. Liu and Z. Shen, "Textures formed in a CoCrMo alloy by selective laser melting," *Journal of Alloys and Compounds,* vol. 631, pp. 153-164, 2015.

[59] B. AlMangour, D. Grzesiak and J.-M. Yang, "Scanning strategies for texture and anisotropy tailoring during selective laser melting of TiC/316L stainless steel nanocomposites," *Journal of Alloys and Compounds,* vol. 728, pp. 424-435, 2017.

[60] I. Koutiri, E. Pessard, P. Peyre, O. Amlou and T. De Terris, "Influence of SLM process parameters on the surface finish, porosity rate and fatigue behavior of as-built Inconel 625 parts," *Journal of Materials Processing Technology,* no. 255, pp. 536-546, 2018.

[61] A. Martin, N. Calta, S. Khairallah, J. Wang, P. Depond, A. Fong, V. Thampy, G. Guss, A. Kiss, K. Stone, C. Tassone, J. Weker, M. Toney, T. van Buuren, Matthews and M, "Dynamics of pore formation during laser powder bed fusion additive manufacturing," *Nature Communications,* vol. 10, 2019.

[62] J. Pakkanen, "Designing for Additive Manufacturing -Product and Process Driven Design for Metals and Polymers," Politecnico di Torino, Torino, 2018.

[63] X. Wang, T. Laoui, J. Kruth, B. Lauwers and L. Froyen, "Direct Selective Laser Sintering of Hard Metal Powders: Experimental Study and Simulation," *The International Journal of Advanced Manufacturing Technology,* no. 19, pp. 351-357, 2002.

[64] A. Simchi, "Direct laser sintering of metal powders: Mechanism, kinetics and microstructural features," *Materials Science and Engineering A,* no. 428, pp. 148-158, 2006.

[65] P. Fischer, V. Romano, H. Weber, N. Karapatis, E. Boillat and R. Glardon, "Sintering of commcerically pure titanium powder with a Nd:YAG laser source," *Acta Materialia,* vol. 51, no. 6, pp. 1651-1662, 2003.

[66] S. Katayama, "Introduction: fundamentals of laser welding," in *Handbook of Laser Welding Technologies*, Woodhead Publishing, 2013, pp. 3-16.

[67] C. Panwisawas, B. Perumal, R. Ward, N. Turner, R. Turner, J. Brooks and H. Basoalto, "Keyhole formation and thermal fluid flow-induced porosity during laser fusion welding in titanium alloys: Experimental and modelling," *Acta Materialia,* vol. 126, pp. 251-263, 2017.

[68] U. Bertoli, G. Guss, S. Wu, M. Matthews and J. Schoenung, "In-situ characterization of laser-powder interaction and cooling rates through high-speed imaging of powder bed fusion additive manufacturing," *Materials and Design,* no. 135, pp. 385-396, 2017.

[69] S. Ly, A. Rubenchik, S. Khairallah, G. Guss and M. Matthews, "Metal vapor micro-jet controls material redistribution in laser powder bed fusion additive manufacturing," *Scientific Reports,* no. 7, 2017.

[70] B. Keene, "Review of data for the surface tension of iron and its binary alloys," *International Materials Review,* vol. 33, no. 1, pp. 1-36, 1988.

[71] K. Mills, B. Keene, R. Brooks and A. Shirali, "Maragoni Effects in Welding," *Philosophical Transactions: Mathematical, Physical and Engineering Sciences,* vol. 356, no. 1739, pp. 911-925, 1998.

[72] S. Kou, Welding Metallurgy: Second Edition, Hoboken, New Jersey: John Wiley & Sons, Inc., 2003.

[73] A. Raza, T. Fiegl, I. Hanif, A. Markström, M. Franke, C. Körner and E. Hryha, "Degradation of AlSi10Mg powder during laser based powder bed fusion processing," *Materials & Design,* vol. 198, p. 109358, 2021.

[74] C. Zhuoer, A. Raza and E. Hryha, "Influence of part geometry on spatter formation in laser powder bed fusion of Inconel 718 alloy revealed by optical tomography," *Journal of Manufacturing Processes,* vol. 81, pp. 680-695, 2022.

[75] C. Pauzon, A. Raza, E. Hryha and P. Foret, "Oxygen balance during laser powder bed fusion of Alloy 718," *Materials & Design,* vol. 201, 2021.

[76] P. Bidare, I. Bitharas, R. Ward, M. Attallah and A. Moore, "Fluid and particle dynamics in laser powder bed fusion," *Acta Materialia,* vol. 142, pp. 107-120, 2018.

[77] X. He, J. Norris, P. Fuerschbach and T. DebRoy, "Liquid metal expulsion during laser spot welding of 304 stainless steel," *Journal of Physics D: Applied Physics,* vol. 39, no. 3, 2006.

[78] C. Pauzon, B. Hoppe, T. Pichler, S. Dubiez-Le Goff, P. Foret, T. Nguyen and E. Hryha, "Reduction of incandescent spatter with helium addition to the process gas during laser powder bed fusion of Ti-6Al-4V," *CIRP Journal of Manufacturing Science and Technology,* vol. 35, pp. 371-378, 2021.

[79] T. Fiegl, M. Franke, A. Raza, E. Hryha and C. Körner, "Effect of AlSi10Mg0.4 long-term reused powder in PBF-LB/M on the mechanical properties," *Materials & Design,* vol. 212, p. 110176, 2021.

[80] A. Raza, C. Pauzon, E. Hryha, A. Markstrom and P. Foret, "Spatter oxidation during laser powder bed fusion of Alloy 718: Dependence on oxygen content in process atmosphere," *Additive Manufacturing,* vol. 48, p. 102369, 2021.

[81] T. Fedina, J. Sundqvist and A. Kaplan, "Spattering and oxidation phenomena during recycling of low alloy steel powder in Laser Powder Bed Fusion," *Materials Today Communications,* vol. 27, p. 102241, 2021.

[82] P. Krakmalev, I. Yadroitsava, G. Fredriksson and I. Yadroitsev, "In situ heat treatment in selective laser melted martensitic AISI 420 stainless steels," *Materials and Design,* vol. 87, pp. 380-385, 2015.

[83] C. Hagenlocher, P. O'Toole, W. Xu, M. Brandt, M. Easton and A. Molotnikov, "Analytical modelling of heat accumulation in laser based additive manufacturing processesof metals," *Additive Manufacturing,* vol. 60, p. 103263, 2022.

[84] J. Zhang, Y. Liu, M. Bayat, Q. Tan, Y. Yin, Z. Fan, S. Liu, J. Hattel, M. Dargusch and M.-X. Zhang, "Achieving high ductility in a selectively laser melted commercial pure-titanium via in-situ grain refinement," *Scripta Materialia,* vol. 191, pp. 155-160, 2021.

[85] H. Chae, E.-W. Huang, W. Woo, S. Kang, J. Jain, K. An and S. Lee, "Unravelling thermal history during additive manufacturing of martensitic stainless steel," *Journal of Alloys and Compounds,* vol. 857, 2021.

[86] P. Promoppatum, S.-C. Yao, P. Pistorius, A. Rollett, P. Coutts, F. Lia and R. Martukanitz, "Numerical modeling and experimental validation of thermal history and microstructure for additive manufacturing of an Inconel 718 product," *Progress in Additive Manufacturing,* vol. 3, pp. 15-32, 2018.

[87] M. Roumbouts, "Selective Laser Sintering/Melting of Iron-Based Powders," University of Leuven, 2006.

[88] C. Körner, "Additive manufacturing of metallic components by selective electron beam melting - a review," *International Materials Reviews,* vol. 61, no. 5, pp. 361-377, 2016.

[89] M. Chiumenti, E. Neiva, E. Salsi, M. Cervera, S. Badia, J. Moya, Z. Chen, C. Lee and C. Davies, "Numerical modelling and experimental validation in Selective Laser Melting," *Additive Manufacturing,* no. 18, pp. 171-185, 2017.

[90] R. Li, J. Liu, Y. Shi, L. Wang and W. Jiang, "Balling behavior of stainless steel and nickel powder during selective laser melting process," *The International Journal of Advanced Manufacturing Technology,* vol. 59, pp. 1025-1035, 2012.

[91] D. Gu and Y. Shen, "Balling phenomena in direct laser sintering of stainless steel powder: Metallurgical mechanisms and control methods," *Materials and Design,* vol. 30, pp. 2903-2910, 2009.

[92] H. Niu and I. Chang, "Instability of scan tracks of selective laser sintering of high speed steel powder," *Scripta Materialia,* vol. 41, no. 11, pp. 1229-1234, 1999.

[93] S. Das, "Physical Aspects of Process Control in Selective Laser Sintering of Metals," *Advanced Engineering Materials,* vol. 5, no. 10, 2003.

[94] Z. Chen, X. Wu, D. Tomus and C. Davies, "Surface roughness of Selective Laser Melted Ti-6Al-4V alloy components," *Additive Manufacturing,* vol. 21, pp. 91-103, 2018.

[95] J. Gockel, L. Sheridan, B. Koerper and B. Whip, "The influence of additive manufacturing processing parameters on surface roughness and fatigue life," *International Journal of Fatigue,* vol. 124, pp. 380-388, 2019.

[96] S. Rahmati and E. Vahabli, "Evaluation of analystical modeling for improvement of surface roughness of FDM test part using measurement results," *The International Journal of Advanced Manufacturing Technology,* vol. 79, pp. 823-829, 2015.

[97] A. Spierings, N. Herres and G. Levy, "Influence of the particle size distribution on surface quality and mechanical properties in AM steel parts," *Rapid Prototyping Journal,* vol. 17, no. 3, pp. 195-202, 2011.

[98] H. Gong, K. Rafi, H. Gu, G. Janaki Ram, T. Starr and B. Stucker, "Influence of defects on mechanical properites of Ti-6Al-4V components produced by selective laser melting and electron beam melting," *Materials and Design,* vol. 86, pp. 545-554, 2015.

[99] J. Stef, A. Poulon-Quintin, A. Redjaimia, J. Ghanbaja, O. Ferry, M. De Sousa and M. Goune, "Mechanism of porosity formation and influence on mechanical properties in selective laser melting of Ti-6Al-4V parts," *Materials and Design,* vol. 156, pp. 480-493, 2018.

[100] C. Shi, S. Dietrich and V. Schulze, "Parameter optimization and mechanical properties of 42CrMo4 manufactured by laser powder bed fusion," *The International Journal of Advanced Manufacturing Technology,* vol. 121, pp. 1899-1913, 2022.

[101] Q. Liu, J. Elambasseril, S. Sun, M. Leary, M. Brandt and P. Sharp, "The Effect of Manufacturing Defects on The Fatigue Behaviiour of Ti-6Al-4V Specimens Fabricated Using Selective Laser Melting," *Advanced Materials Research,* Vols. 891-892, pp. 1519-1524, 2014.

[102] R. Cunningham, S. Narra, C. Montgomery, J. Beuth and A. Rollett, "Synchrotron-Based X-ray Microtomography Characterization of the Effect of Processing Variables on Porosity Formation in Laser Powder-Bed Additive Manufacturing of Tu-6Al-4V," *JOM,* vol. 69, pp. 479-484, 2017.

[103] L. Thijs, F. Verhaeghe, T. Craeghs, J. Van Humbeeck and J.-P. Kruth, "A study of the microstructural evolution during selective laser melting of Ti-6Al-4V," *Acta Materialia,* vol. 58, pp. 3303-3312, 2010.

[104] R. Gunnerek, "Improving Build Rate of Low Alloy Steels Produced by Laser Powder Bed Fusion: Influence of layer thickness on processability," Chalmers University of Technology, 2020.

[105] R. Mertens, S. Dadbakhsh, J. Van Humbeeck and J. Kruth, "Application of base plate preheating during selective laser melting," *Procedia CIRP,* vol. 74, pp. 5-11, 2018.

[106] A. Simchi, "The Role of Particle Size on the Laser Sintering of Iron Powder," *Metallurgical and Materials Transactions B,* vol. 35B, pp. 937-948, 2004.

[107] W. King, W. Barth, V. Castillo, G. Gallegos, J. Gibbs, D. Hahn and C. R. A. Kamath, "Observation of keyhole-mode laser melting in laser powder-bed fusion additive manufacturing," *Journal of Materials Processing Technology,* vol. 214, pp. 2915-2925, 2014.

[108] J. Gordon, S. Narra, R. Cunningham, H. Liu, H. Chen, R. Suter, J. Beuth and A. Rollett, "Defect structure process maps for laser powder bed fusion additive manufacturing," *Additive Manufacturing,* vol. 36, 2020.

[109] A. Martin, N. Calta, J. Hammons, S. Khairallah, M. Nielsen, R. Shuttlesworth, N. Sinclair, M. Matthews, J. Jeffries, T. Willey and J. Lee, "Ultrafast dynamics of laser-metal interactions in additive manufacturing alloys captured by in situ X-ray imaging," *Materials Today Advances,* vol. 1, 2019.

[110] M. Bayat, A. Thanki, S. Mohanty, A. Wiyvrouw, S. Yang, J. Thorborg, N. Tiedje and J. Hattel, "Keyhole-induced porosities in Laser-based Powder Bed Fusion (L-PBF) of Ti6Al4V: High-fidelity modelling and experimental validation," *Additive Manufacturing,* vol. 30, 2019.

[111] J. Zhao, M. Easton, M. Qian, M. Leary and M. Brandt, "Effect of building direction on porosity and fatigue life of selective laser mleted AlSi12Mg alloy," *Materials Science & Engineering A,* vol. 729, pp. 76-85, 2018.

[112] R. Cunningham, "Defect Formation Mechanisms in Powder Bed Metal Additive Manufacturing," Carnegie Mellon University, 2018.

[113] A. Bobel, H. Jr., L, I. Chelladurai, A. Sachdev, T. Brown, W. Poling, R. Kubic, B. Gould, C. Zhao, N. Parab, A. Greco and T. Sun, "In situ synchrotron X-ray imaging of 4140 steel laser powder bed fusion," *Materialia,* vol. 6, 2019.

[114] B. Zhang, Y. Li and Q. Bai, "Defect Formation Mechanisms in Selective Laser Melting: A Review," *Chinese Journal of Mechanical Engineering,* vol. 30, pp. 515-527, 2017.

[115] E. Jelis, M. Hespos, S. Groeschler and R. Carpenter, "L-PBF of 4340 Low Alloy Steel: Influence of Feedstock Powder, Layer Thickness, and Machine Maintenance," *Journal of Materials Engineering and Performance,* vol. 28, no. 2, pp. 693-700, 2019.

[116] P. Withers and H. Bhadeshia, "Residual stress. Part 1 - Measurement techniques," *Materials Science and Technology,* vol. 17, no. 4, pp. 355-365, 2001.

[117] P. Withers and H. Bhadeshia, "Residual stress. Part 2 - Nature and origins," *Materials Science and Technology,* vol. 17, no. 4, pp. 366-375, 2001.

[118] J. Bartlett and X. Li, "An overview of residual stresses in metal powder bed fusion," *Additive Manufacturing,* vol. 27, pp. 131-149, 2019.

[119] T. Simson, A. Emmel, A. Dwars and J. Böhm, "Residual stress measurements on AISI 316L samples manufactured by selective laser melting," *Additive Manufacturing,* vol. 17, pp. 183-189, 2017.

[120] I. Yadroitsev and I. Yadroitsava, "Evaluation of residual stress in stainless steel 316L and Ti6Al4V samples produced by selective laser melting," *Virtual and Physical Prototyping,* vol. 10, no. 2, pp. 67-76, 2015.

[121] A. Dunbar, E. Denlinger, J. Heigel, P. Michaleris, P. Guerrier, R. Martukanitz and T. Simpson, "Development of experimental method for in situ distortion and temperature measurements

during the laser powder bed fusion additive manufacturing process," *Additive Manufacturing,* vol. 12, pp. 25-30, 2016.

[122] F. Galbusera, A. Demir, J. Platl, C. Turk, R. Schnitzer and B. Previtali, "Processability and cracking behaviour of novel high-alloed tool steels processed by Laser Powder Bed Fusion," *Journal of Materials Processing Technology,* vol. 302, p. 117435, 2022.

[123] P. Mercelis and J. Kruth, "Residual stresses in selective laser sintering and selective laser melting," *Rapid Prototyping Journal,* pp. 254-265, 2006.

[124] B. Vrancken, V. Cain, R. Knutsen and J. Van Humbeeck, "Residual stress via the contour method in compact tension specimens produced via selective laser melting," *Scripta Materialia,* vol. 87, pp. 29-32, 2014.

[125] J. Montero, S. Weber, M. Bleckmann, K. Paetzold and E. Jägle, "Determination of bi-dimensional normal residual stress distribution in metallic laser-based powder bed fusion parts," *Mechanics of Materials,* vol. 173, p. 104437, 2022.

[126] L. A. I. Parry and R. Wildman, "Understanding the effect of laser scan stradegy on residual stresses in selective laser meting through thermo-mechanical simulation," *Additive Manufacturing,* vol. 12, pp. 1-15, 2016.

[127] E. Denlinger, J. Heigel, P. Michaleris and T. Palmer, "Effect of inter-layer dwell time on distortion and residual stress in additive manufacturing of titanium and nickel alloys," *Journal of Materials Processing Technology,* vol. 215, pp. 123-131, 2015.

[128] J.-P. Kruth, J. Deckers, E. Yasa and R. Wauthle, "Assesing and comparing influencing factors of residual stresses in selective laser melting using novel analysis method," *Proceedings of the Instituion of Mechanical Engineers, Part B: Journal of Engineering Manufacture,* vol. 226, no. 6, pp. 980-991, 2012.

[129] L. Anderson, A. Venter, B. Vrancken, D. Marais, J. Van Humbeeck and T. Becker, "Understanding the Residual Stress Distribution in Selective Laser Melting Produced Ti-6Al-4V using Neutron Diffraction," *Materials Research Proceedings,* vol. 4, pp. 73-78, 2018.

[130] M. Zaeh and G. Branner, "Investigations on residual stresses and deformation in selective laser melting," *Production Engineering,* vol. 4, pp. 35-45, 2010.

[131] E. Pereloma and D. Edmonds, Phase Transformations in Steels: Diffusionless Transformations, High Strength Steels, Modelling and Advanced Analytical Techniques, Elsevier Science & Technology, 2012.

[132] J. Moyer and G. Ansell, "The Volume Expansion Accompanying the Martensite Transformation in Iron-Carbon Alloys," *Metallurgical Transactions A,* vol. 6A, pp. 1785-1791, 1975.

[133] J. Yan, D. Zheng, H. Li, X. Jia, J. Sun, Y. Li, M. Qian and M. Yan, "Selective laser melting of H13: microstructure and residual stress," *Journal of Materials Science,* vol. 52, pp. 12476-12485, 2017.

[134] M. Narvan, A. Ghasemi, E. Fereiduni, S. Kendrish and M. Elbestawi, "Part deflection and residual stresses in laser powder bed fusion of H13 tool steel," *Materials and Design,* vol. 204, p. 109659, 2021.

[135] J. Saewe, "Investigation of the processability of high-speed steel HS6-5-3-8 by laser powder bed fusion," RWTH Aachen University, Aachen, Germany, 2022.

[136] J. Platl, H. Leitner, C. Turk, A. Demir, B. Previtali and R. Schnitzer, "Defects in a Laser Powder Bed Fused Tool Steel," *Advanced Engineering Materials,* vol. 23, no. 12, p. 2000833, 2021.

[137] L. Wu, S. Das, W. Gridin, S. Leuders, M. Kahlert, M. Vollmer and T. Niendorf, "Hot Work Tool Steel Processed by Laser Powder Bed Fusion: A Review on Most Relevant Influencing Factors," *Advanced Engineering Materials,* vol. 23, no. 7, p. 2100049, 2021.

[138] P. Winchell and M. Cohen, "The effect of carbon on the hardness of martensite and austenite," *Transactions of the Metallurgical Society of AIME,* vol. 224, pp. 638-657, 1962.

[139] R. Grange, C. Hribal and L. Porter, "Hardness of Tempered Martensite in Carbon and Low-Alloy Steels," *Metallurgical Transactions A,* vol. 8A, pp. 1775-1785, 1977.

[140] J. Saewe, N. Carstensen, P. Kurnsteiner, E. Jägle and J. Schleifenbaum, "Influence of increased carbon content on the processability of high-speed steel HS6-5-3-8 by laser powder bed fusion," *Additive Manufacturing,* vol. 46, p. 102125, 2021.

[141] P. Harvey, Engineering Properties of Steels, American Society for Metals, 1982.

[142] G. Krauss, Physical Metallurgy and Heat Treatment of Steel, American Society for Metals, 1985.

[143] *Ansys Granta EduPack Software,* Cambridge, UK: ANSYS, Inc., 2022.

[144] H. Bhadeshia and R. Honeycombe, Steels: Microstructure and Properties 4th Edition, Elsevier, 2017.

[145] G. Krauss, Steels - Processing, Structure, and Performance (2nd Edition), Materials Park, OH: ASM International, 2015.

[146] Y. Lu, H. Yu and R. Sisson Jr., "The effect of carbon content on the c/a ratio of as-quenched martensite in Fe-C alloys," *Materials Science & Engineering A,* vol. 700, pp. 592-597, 2017.

[147] A. Marder and G. Krauss, "The Morphology of Martensite in Iron-Carbon Alloys," *Trans. ASM,* vol. 60, pp. 651-660, 1967.

[148] C. Roberts, "Effect of Carbon on the Volume Fractions and Lattice Parameters of Retained Austenite and Martensite," *Trans. AIME,* vol. 197, pp. 203-204, 1953.

[149] A. Hanumantharaju, "Thermodynamic modelling of martensite start temperature in commercail steels," KTH Royal Institute of Technology, Stockholm, 2017.

[150] H. Yang and H. Bhadeshia, "Austenite grain size and the martensite-start temperature," *Scripta materialia,* vol. 60, pp. 493-495, 2009.

[151] S. van Bohemen and L. Morsdorf, "Predicting the Ms temperature of steels with a thermodynamic based model including the effect of the prior austenite grain size," *Acta Materialia,* vol. 125, pp. 401-415, 2017.

[152] T. Maki, K. Tsuzaki and I. Tamura, "The Morphology of Microstructure Composed of Lath Martensites in Steels," *Transactions ISIJ,* vol. 20, pp. 207-214, 1980.

[153] K. Tsuzaki and T. Maki, "The Effect of Cooling Rate on the Morphology of Lath Martensite in Fe-Ni Alloys," *J. Japan Inst. Metals.,* vol. 45, no. 2, pp. 125-134, 1981.

[154] T. Furuhara, K. Kikumoto, H. Saito, T. Sekine, T. Ogawa, S. Morito and T. Maki, "Phase Transformation from Fine-grained Austenite," *ISIJ International,* vol. 48, no. 8, pp. 1038-1045, 2008.

[155] S. Morito, H. Tanaka, R. Konishi, T. Furuhara and T. Maki, "The morphology and crystallography of lath martensite in Fe-C alloys," *Acta Materialia,* vol. 51, pp. 1789-1799, 2003.

[156] D. Porter, K. Easterling and M. Sherif, Phase Transformations in Metals and Alloys 3rd ed., Boca Raton, USA: Taylor & Francis Group, 2009.

[157] A. Shibata, S. Morito, T. Furuhara and T. Maki, "Substructures of lenticular martensites with different martensite start temperatures in ferrous alloys," *Acta Materialia,* vol. 57, pp. 483-492, 2009.

[158] T. Kakeshita and K. Shimizu, "Growth behavior of lenticular and thin plate martensites in ferrous alloys and steels," *Scripta Metallurgica,* vol. 14, no. 10, pp. 1067-1070, 1980.

[159] J. Chilton and P. Kelly, "The strength of ferrous martensite," *Acta Metallurgica,* vol. 16, pp. 637-656, 1968.

[160] R. Grange, "Strengthening steel by austenite grain refinement," *Transactions of ASM,* vol. 16, pp. 26-48, 1966.

[161] G. Speich and W. Leslie, "Tempering of Steel," *Metallurgical Transactions,* vol. 3, pp. 1043-1054, 1972.

[162] G. Roberts and G. Krauss, Tool Steels 5th Edition, Materials Park, OH, USA: ASM International, 1998.

[163] T. Furuhara, G. Miyamoto and T. Maki, "Control of Cementite in Temepred Lath Martensite by Rapid Heating and Tempering," *ISIJ International,* vol. 44, no. 11, pp. 1937-1944, 2004.

[164] H. Joo, W. Kim, Y. Kim, Y. Jo, M. Kang, J. Lee, J. Lee, M. Kim, G. Kim, S. Kim and D. Kim, "Effect of Laser Power on the Microstructure Evolution and Mechanical Properties of 20MnCr5 Low Alloy Steel Produced by Laser-Based Powder Bed Fusion," *Metals and Materials International,* 2022.

[165] M. Abdelwahed, S. Bengtsson, R. Casati, A. Larsson, S. Petrella and M. Vedani, "Effect of water atomization on properties of tpe 4130 steel processed by L-PBF," *Materials & Design,* vol. 210, p. 110085, 2021.

[166] Y. Han, C. Zhang, X. Cui, S. Zhang, J. Zhang and Y. Liu, "The formability and microstructure evolution of 24CrNiMo alloy steel fabricated by selective laser melting," *Vacuum,* vol. 175, p. 109297, 2020.

[167] W. Hearn, K. Lindgren, J. Persson and E. Hryha, "In situ tempering of martensite during laser power bed fusion of Fe-0.45C steel," *Materialia,* vol. 23, p. 101459, 2022.

[168] R. Seede, B. Zhang, A. Whitt, S. Picak, S. Gibbons, P. Flater, A. A. R. Elwany and I. Karaman, "Effect of heat treatments on the microstructure and mechanical properties of an ultra-high strength martensitic steel fabricated via laser powder bed fusion additive manufacturing," *Additive Manufacturing,* vol. 47, 2021.

[169] T. Neindorf, S. Leuders, A. Riemer, H. Richard, T. Tröster and D. Schwarze, "Highly Anisotropic Steel Processed by Selective Laser Melting," *Metallurgical and Materials Transactions B,* vol. 44, pp. 794-796, 2013.

[170] N. Haghdadi, M. Laleh, M. Moyle and S. Primig, "Additive manufacturing of steels: a review of achievements and challenges," *Journal of Materials Science,* vol. 56, pp. 64-107, 2021.

[171] A. Leicht, M. Rashidi, U. Klement and E. Hryha, "Effect of process parameters on the microstructure, tensile strength and productivity of 316L parts produced by laser powder bed fusion," *Materials Characterization,* vol. 159, p. 110016, 2020.

[172] A. Leicht, C. Yu, V. Luzin, U. Klement and E. Hryha, "Effect of scan rotation on the microstrcuture development and mechanical properties of 316L parts produced by laser powder bed fusion," *Materials Characterization,* vol. 163, p. 110309, 2020.

[173] F. Niessen, T. Nyssönen, A. Gazder and R. Hielscher, "Parent grain reconstruction from partially or fully transformed microstructures in MTEX," *ArXiv Prepr. ArXiv2104.14603.,* 2021.

[174] J. Damon, R. Koch, D. Kaiser, G. Graf, S. Dietrich and V. Schulze, "Process development and impact of intrinsic heat treatment on the mechanical perforamnce of selective laser melted AISI 4140," *Additive Manufacturing,* vol. 28, pp. 275-284, 2019.

[175] M. Ryder, C. Montgomery, M. Brand, J. Carpenter, Jones, A. Spangenberger and D. Lados, "Melt Pool and Heat Treatment Optimization for the Fabrication of High-Strength and High-Toughness Additively Manufactured 4340 Steel," *Journal of Materials Engineering and Performance,* vol. 30, pp. 5426-5440, 2021.

[176] E. Hager, R. O'Hara, G. Cobb, P. Flater, E. Payton, V. Sinha, B. Doane and R. Kemnitz, "Development of high density parts in the low-alloy, high-performance steel AF9628 using laser powder bed fusion," *Materials Science & Engineering A,* vol. 838, p. 142656, 2022.

[177] J. Dantzig and M. Rappaz, Solidification, Boca Raton: CRC Press, 2009.

[178] S. Babu, J. Elmer, J. Vitek and S. David, "Time-resolved X-ray diffraction investigation of primary weld solidification in Fe-C-Al-Mn steel welds," *Acta Materialia,* vol. 50, pp. 4763-4781, 2002.

[179] J. Andersson, T. Helander, L. Höglund, P. Shi and B. Sundman, "Thermo-Calc and DICTRA, Computational tools for materials science," *Calphad,* vol. 26, pp. 273-312, 2002.

[180] M. Holzweissig, A. Taube, S. M. Brenne and T. Niendorf, "Microstructure Characterization and Mechanical Performance of Hot Work Tool Steel Processed by Selective Laser Melting," *Metallurgical and Materials Transactions B,* vol. 46, pp. 545-549, 2015.

[181] "JMatPro: Pratical Software for Materials Properties," Senate Software UK, 2020. [Online]. Available: https://www.sentesoftware.co.uk/. [Accessed 29 12 2020].

[182] W. Wang and S. Kelly, "A Metallurgical Evaluation of the Powder-Bed Laser Additive Manufactured 4140 Steel Material," *JOM,* vol. 68, no. 3, pp. 869-875, 2016.

[183] A. Kudzal, B. McWilliams, J. Taggart-Scarff and M. Knezevic, "Fabrication of a low alloy ultra-high strength (>1500 MPa yield) steel using powder bed fusion additive manufacturing," *Materials Science & Engineering A,* vol. 770, p. 138512, 2020.

[184] D. Bartels, J. Klaffki, I. Pitz, C. K. F. Merklein and Schmidt, "Inverstigation on the Case-Hardening Behavior of Additively Manufactured 16MnCr5," *Metals,* vol. 536, no. 10, 2020.

[185] L. Zumofen, A. Kirchheim and H.-J. Dennig, "Laser powder bed fusion of 30CrNiMo8 steel for quenching and tempering: examination of the processability and mechanical properties," *Progress in Additive Manufacturing,* vol. 5, pp. 75-81, 2020.

[186] M. Abdelwahed, R. Casati, S. Bengtsson, A. Larsson, M. Riccio and M. Vedani, "Effect of Powder Atomization on Microstructural and Mechanical Behaviour of L-PBF Processed Steels," *Metals,* vol. 1474, no. 10, 2020.

[187] T. Fedina, J. Sundqvist, J. Powell and A. Kaplan, "A comparitive study of water and gas atomized low alloy steel powders for additive manufacturing," *Additive Manufacturing,* vol. 36, p. 101675, 2020.

[188] D. Heaney, Handbook of Metal Injection Molding, Woodhead Publishing, 2012.

[189] C. Aumayr, J. Platl, H. Zunko and C. Turk, "Additive Manufacturing of a Low-alloyed Engineering Steel," *Berg Huettenmaenn Monatsh,* vol. 165, no. 3, pp. 137-142, 2020.

[190] P. Agrawal, S. Shukla, S. Thapliyal, P. Agrawal, S. Nene, R. Mishra, B. McWilliams and K. Cho, "Microstructure-Property Correlation in a Laser Powder Bed Fusion Processed High-Strength AF-9628 Steel," *Advanced Engineering Materials,* vol. 23, p. 2000845, 2021.

[191] M. Abdelwahed, R. Casati, A. Larsson, S. Petrella, S. Bengtsson and M. Vedani, "On the Recycling of Water Atomized Powder and the Effects on Properties of L-PBF Processed 4130 Low-Alloy Steel," *Materials,* vol. 336, no. 15, 2022.

[192] Y. Kok, X. Tan, P. Wang, M. Nai, N. Loh, E. Liu and S. Tor, "Anisotropy and heterogeneity of microstructure and mechanical properties in metal additive manufacturing: A criticl review," *Materials and Design,* vol. 139, pp. 565-586, 2018.

[193] M.-W. Wu, P.-H. Lai and J.-K. Chen, "Anisotropy in the impact toughness of selective laser melted Ti-6Al-4V alloy," *Materials Science and Engineering: A,* vol. 650, pp. 295-299, 2016.

[194] M. Schmitt, B. Kempter, S. Inayathulla, A. Gottwalt, M. Horn, M. Binder, J. WInkler, G. Schlick, T. Tobie, K. Stahl and G. Reinhart, "Influence of Baseplate Heating and Shielding Gas on Distortion, Mechanical and Case hardening Properties of 16MnCr5 fabricated by Laser Powder Bed Fusion," *Procedia CIRP,* vol. 93, pp. 581-586, 2020.

[195] W. Hearn, E. Hryha, S. Bengtsson and L. Nyborg, "Processability & Microstructure of Fe-C System via L-PBF," *EuroPM Proceedings 2019,* 2019.

[196] A. Spierings, M. Voegtlin, T. Bauer and K. Wegener, "Powder flowability characterisation methodology for powder-bed-based metal additive manufacturing," *Progress in Additive Manufacturing,* vol. 1, pp. 9-20, 2016.

[197] "EN ISO 15350: Steel and iron — Determination of total carbon and sulfur content — Infrared absorption method after combustion in an induction furnace (routine method)," ISO, 2010.

[198] "EN 10276-2: Chemical analysis of ferrous materials - Determination of oxygen content in steel and iron - Part 2: Infrared method after fusion under inert gas," CEN, 2003.

[199] C. Schneider, W. Rasband and K. Eliceiri, "NIH Image to ImageJ: 25 years of image analysis," *Nature Methods,* pp. 671-675, 2012.

[200] G. Kasperovich and J. Hausmann, "Improvement of fatigue resistance and ductility of TiAl6V4 processed by selective laser melting," *Journal of Materials Processing Technology,* no. 220, pp. 202-214, 2015.

[201] J. Goldstein, D. Newbury, J. Michael, N. Ritchie, J. Scott and D. Joy, Scanning Electron Microscopy and X-Ray Microanalysis - Fourth Edition, Springer, 2018.

[202] K. Vernon-Parry, "Scanning electron microscopy: an introduction," *III-Vs Review,* vol. 13, no. 4, pp. 40-44, 2000.

[203] A. Schwartz, M. Kumar, B. Adams and D. Field, Electron Backscatter Diffraction in Materials Science - Second Edition, Springer, 2009.

[204] C. Carter and D. Williams, Transmission Electron Microscopy: Diffraction, Imaging, and Spectrometry, Springer, 2016.

[205] B. Gault, M. Moody, J. Cairney and S. Ringer, Atom Probe Microscopy, New York: Springer, 2012.

[206] M. Miller and R. Forbers, Atom-Probe Tomography: The Local Electrode Atom Probe, New York: Springer, 2014.

[207] "CALPHAD Methodology," Thermo-Calc Software, 2020. [Online]. Available: https://thermocalc.com/about-us/methodology/the-calphad-methodology/. [Accessed 29 12 2020].

[208] F. Huyan, P. Hedström, L. Höglund and A. Borgenstam, "A Thermodynamic-Based Model to Predict the Fraction of Martensite in Steels," *Metallurgical and Materials Transactions A,* vol. 47, pp. 4404-4410, 2016.

[209] A. E384-17, Standard Test Method for Microindentation Hardness of MAterials, West Conshohocken, PA: ASTM International, 2017.

[210] H. Wang, L. Zhu and B. Xu, Residual Stresses and Nanoindentation Testing of Films and Coatings, Beijing: Springer, 2018.

[211] "ASTM E2298-18: Standard Test Method for Instrumented Impact Testing of Metallic Materials," ASTM International, 2018.

[212] "ASTM E8M/E8M-21: Standard Test Methods for Tension Testing of Metallic Materials," ASTM International, 2021.

[213] G. Krauss and A. Marder, "The Morphology of Martensite in Iron Alloys," *Metallurgical Transactions,* vol. 2, pp. 2343-2357, 1971.

[214] V. Thampy, A. Fong, N. Calta, J. Wang, A. Martin, P. Depond, A. Kiss, G. Guss, Q. Xing, R. Ott, A. Van Buuren, M. Toney, J. Weker, M. Kramer, M. Matthews, C. Tassone and K. Stone, "Subsurface Cooling Rates and Microstructural Response during Laser Based Metal Additive Manufacturing," *Scientific Reports,* no. 10, 2020.

[215] "ASTM A958/A958M - 17: Standard Specification for Steel Castings, Carbon and Alloy, with Tensile Requirements, Chemical Requirements Similar to Standard Wrought Grades," ASTM International, 2017.

[216] "ASTM A673/A673M - 17: Standard Specification for Sampling Procedure for Impact Testing of Structural Steel," ASTM International, 2017.